UC Berkeley
UC Berkeley Electronic Theses and Dissertations

Title

Full Core, Heterogeneous, Time Dependent Neutron Transport Calculations with the 3D Code DeCART

Permalink

https://escholarship.org/uc/item/8pk9n07h

Author

Hursin, Mathieu

Publication Date

2010

Peer reviewed|Thesis/dissertation

Full Core, Heterogeneous, Time Dependent Neutron Transport
Calculations with the 3D Code DeCART

by

Mathieu Hursin

A dissertation submitted in partial satisfaction of the
requirements for the degree of

Doctor of Philosophy

In

Engineering - Nuclear Engineering

in the

GRADUATE DIVISION

of the

UNIVERSITY OF CALIFORNIA AT BERKELEY

Committee in charge:

Professor Ehud Greenspan, Chair
Professor Per F. Peterson
Professor Thomas Downar
Professor Jon Wilkening

Fall
2010

ABSTRACT

Hursin, Mathieu. PhD, University of California at Berkeley, December 2010. Full Core, Heterogeneous, Time Dependent Neutron Transport Calculations with the 3D Code DeCART. Major Professors: Tom Downar and Ehud Greenspan.

The current state of the art in reactor physics methods to assess safety, fuel failure, and operability margins for Design Basis Accidents (DBAs) for Light Water Reactors (LWRs) rely upon the coupling of nodal neutronics and one-dimensional thermal hydraulic system codes. The neutronic calculations use a multi-step approach in which the assembly homogenized macroscopic cross sections and kinetic parameters are first calculated using a lattice code for the range of conditions (temperatures, burnup, control rod position, etc...) anticipated during the transient. The core calculation is then performed using the few group cross sections in a core simulator which uses some type of coarse mesh nodal method. The multi-step approach was identified as inadequate for several applications such as the design of MOX cores and other highly hetereogeneous, high leakage core designs. Because of the considerable advances in computing power over the last several years, there has been interest in high-fidelity solutions of the Boltzmann Transport equation. A practical approach developed for high-fidelity solutions of the 3D transport equation is the 2D-1D methodology in which the method of characteristics (MOC) is applied to the heterogeneous 2D planar problem and a lower order solution is applied to the axial problem which is, generally, more uniform. This approach was implemented in the DeCART code. Recently, there has been interest in extending such approach to the simulations of design basis accidents, such as control rod ejection accidents also known as reactivity initiated accidents (RIA). The current 2D-1D algorithm available in DeCART only provide 1D axial solution based on the diffusion theory whose accuracy deteriorates in case of strong flux gradient that can potentially be observed during RIA simulations.

The primary ojective of the dissertation is to improve the accuracy and range of applicability of the DeCART code and to investigate its ability to perform a full core transient analysis of a realistic RIA.

The specific research accomplishments of this work include:

- The addition of more accurate 2D-1D coupling and transverse leakage splitting options to avoid the occurrence of negative source terms in the 2D MOC equations and the subsequent failure of the DeCART calculation and the improvement of the convergence of the 2D-1D method.
- The implementation of a higher order transport axial solver based on NEM-Sn derivation of the Boltzmann equation.

- Improved handling of thermal hydraulic feedbacks by DeCART during transient calculations.
- A consistent comparison of the DeCART transient methodology with the current multistep approach (PARCS) for a realistic full core RIA.

An efficient direct whole core transport calculation method involving the NEM-Sn formulation for the axial solution and the MOC for the 2-D radial solution was developed. In this solution method, the Sn neutron transport equations were developed within the framework of the Nodal Expansion Method. A RIA analysis was performed and the DeCART results were compared to the current generation of LWR core analysis methods represented by the PARCS code. In general there is good overall agreement in terms of global information from DeCART and PARCS for the RIA considered. However, the higher fidelity solution in DeCART provides a better spatial resolution that is expected to improve the accuracy of fuel performance calculations and to enable reducing the margin in several important reactor safety analysis events such as the RIA.

To my mother for her unwavering support,
And to my father for sharing his passion.

TABLE OF CONTENTS

LIST OF FIGURES

LIST OF TABLES

AKNOWLEDGEMENTS

Introduction

1.1. <u>Motivation</u>

In the design and licensing of light water reactors, it is postulated that a number of low-probability accidents will occur and it is required that the reactor will be able to withstand their consequences without affecting the public health and safety. Those accidents are called Design Basis Accidents (DBA). The current state of the art methods to assess safety, fuel failure and operability margins for DBAs applicable to existing and advanced Light Water Reactor (LWR) fuel use coupled nodal neutronic and thermal hydraulic system codes. The current generation of LWR core analysis methods using coarse mesh nodal methods employs a multi-steps procedure in which the assembly homogenized macroscopic cross sections and kinetic parameters are first calculated using a lattice code for the range of conditions (temperatures, burnup, control rod position, etc...) anticipated during the transient. The core calculation is then performed using the few group cross sections in a core simulator which uses some type of coarse mesh nodal method. The lattice codes typically used for LWR cross section generation include HELIOS (Scandpower 2000) and CASMO-5 (Rhodes 2008) and the nodal codes typically used for LWR analysis include SIMULATE-3 (Smith 1999) and the U.S. NRC core simulator PARCS (Downar, Xu et al. 2006), which is coupled to the thermal-hydraulics codes RELAP5(NRC 2001), and TRACE (Odar, Murray et al. 2004) to provide temperature and density feedbacks. The fuel pin temperature and power variations during a transient are typically determined through some type of pin power reconstruction method and resulting pin averaged information is provided to fuel performance codes to evaluate fuel behaviour and safety limits. This kind of approach has previously been identified as inadequate (Cho 2006) for the design of MOX cores and the same limitations would be encountered in the analysis of certain innovative core designs; in particular to cores that feature a large heterogeneity in the axial direction.

Because of the considerable advances in computing power over the last several years, there has been interest in high-fidelity solutions of the coupled Boltzmann transport and temperature-fluid field equations. However, the computational burden inherent in 3D transport solutions for practical coupled field applications still requires the investigation of innovative solution algorithms to improve its parallelization and use on computer clusters. During the last several years, a class of algorithms was developed based on "2D-1D" decomposition of the reactor transport problem (Cho 2002; Cho, Lee et al. 2002). This was motivated in part by the naturally stronger radial heterogeneity that occurs in most power reactor core problems. The 2D-1D algorithm involves a set of coupled 2-D planar transport and 1-D axial diffusion solutions. This method has proven to be adequate for a wide range of steady state LWR applications (Cho, Lee et al. 2002).

Recently, there has been interest in taking advantage of advanced numerical methods, involving neutron transport and Computational Fluid Dynamic (CFD), to perform high-fidelity simulations of design basis accidents, such as control rod ejection accidents also known as reactivity initiated accidents (RIA). These include Pressurized Water Reactor (PWR) rod-ejection and Boiling Water Reactor (BWR) rod-drop accidents. In these accidents, energy is deposited in the fuel and causes rapid heating that

may damage the fuel if the power burst is sufficiently energetic. Besides being DBAs, the other advantage of studying RIAs is that they are very short in duration (around a second) and driven by their neutronic behavior. Because of the event's short time-scale, the energy remains mostly where it was deposited. Consequently, an accurate treatment of the heat dissipation both in the cladding and the coolant is not needed to obtain a reasonable simulation of the event, allowing to focus the analysis on the neutronic modeling of the accident while using a simple thermal hydraulic solution to provide temperature and density feedbacks. The feasibility of such analysis with high-fidelity simulations tools like DeCART has been demonstrated by (Hursin 2008).

The DeCART (Deterministic Core Analysis based on Ray Tracing)(Weber, Sofu et al. 2006) code uses the 2D-1D algorithm. Its development began in 2000 as part of International Nuclear Energy Research Initiative (INERI) project collaboration between Korean Atomic Energy Research Institute (KAERI), Argonne National Laboratory (ANL), and Purdue University. The objective was to develop a whole core neutron transport code capable of direct sub-pin level flux calculation at power generating conditions of a PWR and BWR. Unlike the current generation of nodal codes, DeCART does not require a priori homogenization or group condensation which limits the accuracy and fidelity of conventional reactor physics calculations. The local heterogeneity at the sub-pin level is explicitly represented and solved using the Method of Characteristics (MOC) which is an effective transport solution method for such highly refined heterogeneous problems and is widely used for LWR problems in codes such as CASMO-5.

The overarching goal of the dissertation is to investigate the ability of the DeCART code to accurately perform a full core transient analysis of a realistic RIA. During preliminary RIA analysis, the accuracy of the DeCART "2D-1D" formulation was found to be insufficient for certain aspects of the simulation. Therefore, research was undertaken to improve the 2D-1D formulation, specifically to investigate more accurate methods for solution of the axial 1D flux. The next section details what are the issues that had to be resolved in order to accurately model a full core RIA with DeCART.

1.2. Issues and Undertakings

1.2.1. Key issues

While the 2D-1D approach to solve the 3D transport equation has not been thoroughly studied for the widest range of applications, it has worked well for the coupled field solution of the PWR, which is primarily a homogeneous single phase flow thermal-hydraulics problem. However, recent applications to the more axially-heterogeneous two phase flow BWR have exposed limitations in the existing 2D-1D solution algorithm. Recently, the application of the DeCART code and the 2D-1D algorithm to the gas reactor problem has also resulted in some cases in which the 3D solution does not converge. Other convergence issues have been observed when the size of the axial mesh is reduced.

Another issue of the 2D-1D algorithm is related to the axial 1D solver. The presence of heterogeneities in the axial direction (partially inserted control assembly,

severe void variations, part length fuel rod, axial enrichment zoning, etc …) leads to 3D solutions of poor accuracy (Cho, Kim et al. 2006). The current 2D-1D algorithm available in DeCART only provide 1D axial solution based on the diffusion theory whose accuracy deteriorates in case of strong flux gradient, like the one observed for the problems listed above.

Besides the improvements to the 2D-1D algorithm that would impact steady-state and transient solutions, another key aspect of the transient solution algorithm was required in order to model full core transient events. The DeCART transient methodology has been developed and tested (Cho, Kim et al. 2005) only for cases where macroscopic cross sections are given and no thermal hydraulic feedbacks are provided. A proper model of the coupled fields of neutronic and thermal hydraulic is needed to accurately analyze any kind of transient event. DeCART needs to be able to handle variation of the fuel temperature, coolant density, etc…during the course of transient calculations.

1.2.2. *Improvements to DeCART undertaken in this work*

In order to perform high fidelity analysis of a transient event, the following research was performed and represents the main outcome of the work summarized in the present dissertation:

- Addition of an axial 1D solver based on a higher order transport solution than the existing diffusion solver.
- Improvement of the coupling of the 2D and 1D solutions through improved transverse leakage approximations.
- Addition of an online treatment of the local thermal hydraulic conditions during transient analysis.

The first two improvements are validated against the C5G7 benchmark (Lewis, Smith et al. 2001) and the third improvement is tested during the analysis of the full core RIA; its results are compared to the one of the multi-step methodology.

1.3. Dissertation Outline

The remaining sections of the present dissertation are designed to discuss in more detail the improvements needed by DeCART in order to perform a realistic analysis of a RIA and compare the results to those of the current multi-step methodology.

The first chapter provides general background information on the DeCART code, describing its original steady state and transient calculation methodology. The second chapter is dedicated to the improvement of the 2D-1D algorithm and more specifically the coupling between the 2D transport solution and 1D diffusion solution. Five different coupling approaches are investigated and applied to a test problem. The effect in terms of accuracy and convergence properties is then discussed. The third chapter is focused on the improvement of the 1D axial solver. A few different potential solvers are compared. The Nodal Expansion Method (NEM) and discrete ordinate (Sn) method are chosen to handle, respectively, the spatial and angular dependence of the angular flux. The derivation of the NEM-Sn is described as well as its numerical implementation in DeCART. The last part of the third chapter is dedicated to the study of the performance

of the NEM-Sn against the diffusion solver for the C5G7 benchmark (Lewis, Smith et al. 2001). The fourth chapter brings together the improvements described in the Chapter one to three by showing a full core transient calculation for a RIA. The handling of thermal hydraulic feedback during transient calculations is presented. The approach used in the multi-step methodology is detailed and its limitations shown. The subgroup method (Notari and Garraffo 1987), which allows DeCART to treat both spatial and resonance self shielding online, briefly presented in chapter two, is used to apply the proper local thermal hydraulic feedback. The calculation flow of a DeCART transient calculation with thermal hydraulic feedbacks is presented. Finally, the DeCART results are compared with the current multi-step approach. The final chapter of the dissertation summarizes the research performed and its main findings.

2. The DeCART Integral Transport Code

The following sections are describing the primary features of the DeCART code. An overview of code methodology is presented first. Then the derivation of the 2D-1D approach for steady-state and transient calculation is provided and the spatial and energy self-shielding treatment is reviewed.

2.1. Overview

DeCART is a 3-D whole core transport code that is capable of generating sub-pin level power distributions. This is accomplished by obtaining the integral transport solutions to the heterogeneous reactor problem in which the actual detailed geometrical configuration of fuel components such as the pellet and cladding is explicitly retained. The cross section data needed for the neutron transport calculation are obtained directly from a 47 energy group cross section library. Hence DeCART involves neither *a priori* homogenization nor group condensation, which are two of the principal limitations of the current generation of nodal methods most commonly used for reactor analysis.

2.1.1. 2D-1D Solution Approach

DeCART is based on the 2D-1D algorithm which involves a set of coupled 2-D planar transport solutions which use the MOC and a 1-D axial diffusion solution which uses NEM or Semi-Analytical Nodal Method (SANM) (Fu and Cho 2002). The 3-D problem domain is first divided into several thick planes and the MOC calculation is performed for each planar problem to determine the neutron fluxes at the fine flat source regions. The cell homogenized cross sections are then obtained by flux volume weighting based on the flat source region fluxes and the regional microscopic cross sections evaluated at the local thermal condition. A diffusion solution is obtained for each fuel rod to determine the local axial flux shape that is used to modify the MOC calculation in order to take into account axial leakage and produce a 3-D solution.
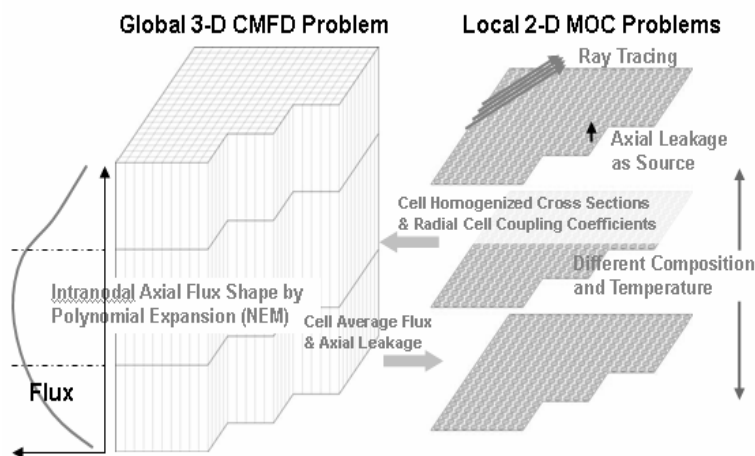
Fig. 2.1. 2D-1D solution based on 2-D MOC and 3-D CMFD formulations

As an effective method to realize a direct whole-core transport calculation capability, the planar MOC solution is combined with a 3-D coarse mesh finite difference (CMFD) solution (Smith 1983; Sutton 1989). The basic idea of this formulation is to represent the whole core transport problem with a simpler 3-D problem using the pin-cell homogenized cross sections generated adaptively from the 2-D MOC solutions. The cell cross sections are then used in the 3-D CMFD problem which represents the global neutron balance. The 3-D CMFD solver becomes the main solver while the MOC and NEM/SANM solvers function merely as the regional flux shape generator. The NEM and SANM solvers are embedded in the CMFD solver, which permits the generation of the axial flux shape directly during the CMFD stage of the calculation. No separate, fuel rod wise, diffusion calculation is necessary. The entire solution process described above is illustrated in Fig. 2.1. The planar MOC calculation is considerably more expensive than the CMFD calculation, as each progression of the MOC solution requires sweeping over tens to hundreds of thousands of rays across the core. Consequently, the CMFD approach provides an effective acceleration to the transport calculation by rapidly converging the fission source distribution at the coarse mesh level. In addition to the multigroup CMFD, a two energy group CMFD kernel has been implemented to further accelerate the DeCART calculation using an effective group rebalance methodology. This two-level CMFD scheme reduces the number of MOC iterations for practical problems by more than an order of magnitude (Joo, Cho et al. 2004).

2.1.2. *Modular Ray Tracing*

DeCART implements a modular ray tracing scheme similar to those described in the literature (Cho 2006) and implemented into codes such as CASMO-5 and CHAPLET (Kosaka and Saji 2000). There are two primary benefits of modular ray tracing: the simplification of the geometry calculation and an increased accuracy of calculations with reflective boundary conditions. In a typical core calculation, there are hundreds of millions of ray segments and the length of each of ray ($s_{l,k}^{n}$) is required. In modular ray tracing, the positioning of the rays is the same for all modular units and the segment lengths must be determined only for a few types of modules. These square ray tracing modules are then arranged in a regular array and the ray tracing is performed by linking rays from one modular unit to the next. The accuracy of problems with reflective boundary conditions is achieved because of the cyclic nature of the ray positioning. That is, the incoming angular flux for a ray with azimuthal angle α is determined from the outgoing angular flux of a ray of angle $-\alpha$ that terminates precisely where the original ray began.

These two features are shown for the case of pin-cell based modular ray tracing in Fig 2.2. The ray positioning in each pin-cell is identical and yields continuous rays that link to neighboring cells. Thus, the 2x2 pin geometry can be computed by calculating the segment lengths in any one cell. Two reflective rays (dashed lines) for the angle $-\alpha$ are given as an example.
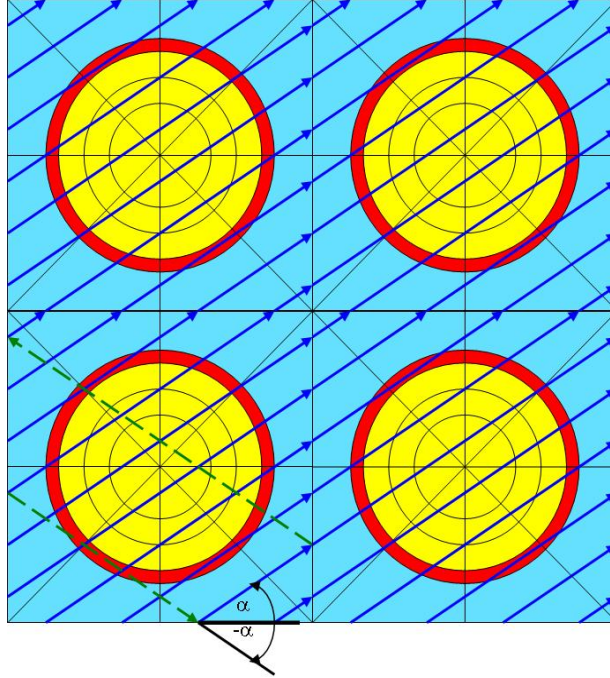
Fig. 2.2. Example of 2x2 fuel pin array with cell modular ray tracing

2.2. Resonance Treatment

In DeCART, the subgroup method is used for the resonance treatment. If a sequence of heterogeneous transport calculations is performed beforehand, the subgroup method permits the adaptive handling of the spatial and energy self-shielding during the calculation. The next sections presenting the resonance treatment are a brief summary of the references (Stamm'Ler and Abbate 1983; Scandpower 2000). Even though no additional work has been done on the resonance treatment in the DeCART code, a detailed understanding of the subgroup method is necessary to properly apply temperature and density changes during transient calculations.

2.2.1. General Treatment

It is very inefficient and time-consuming to use point-wise cross sections in the deterministic transport calculation. Therefore, typically 30 to 70 energy discretized cross sections are used in Light Water Reactor calculations, which are processed from ENDF/B-VI library using codes such as NJOY. The multi-group cross section is calculated by,

$$\sigma_x = \frac{\int_{\Delta E} \sigma_x(E)\phi(E)dE}{\int_{\Delta E} \phi(E)dE} = \frac{\int_{\Delta u} \sigma_x(u)\phi(u)du}{\int_{\Delta u} \phi(u)du} \qquad \text{Eq. 2.1}$$

where u is the lethargy defined by $u = ln\ (E_0/E)$, with $E_0 = 10$ MeV. The accuracy in the deterministic transport calculation is mainly dependent upon the scalar flux, $\phi(u)$, which is not know *a priori*, and group width, Δu, used in Eq. 2.1.

The resonance behavior of $\sigma_a(u)$ complicates the evaluation of group cross sections. The flux, $\phi(u)$, will have dips at and near resonance energies due to the strong absorption in the resonance. These dips depend on the resonances and the concentration of the resonance isotopes and on their location.

The resonance integrals from ENDF/B-VI are tabulated as function of various background cross sections and temperatures for the extended applications. The background cross section can be expressed as follows:

$$\Sigma_b = \lambda\Sigma_p + \Sigma_e \qquad \text{Eq. 2.2}$$

where λ is the hydrogen-equivalence factor also called intermediate resonance factor, Σ_p is the potential scattering cross section and Σ_e is the equivalence cross section. The equivalence cross section represents a departure from a homogeneous geometry: the equivalent cross section takes into account the escape probability from the fuel to the surrounding material (cladding, coolant, etc…), which is mainly dependent upon the geometrical configuration of the fuel pins.

Solving the slowing-down equation at resonance lethargies, and away from fission sources, using the intermediate resonance (IR) approximation(Goldstein and Cohen 1962), leads to the Eq. 2.3:

$$\phi(u) = \frac{\lambda\Sigma_p(u) + \Sigma_e(u)}{\Sigma_a(u) + \lambda\Sigma_p(u) + \Sigma_e(u)} \qquad \text{Eq. 2.3}$$

$\lambda\Sigma_p$ can be obtained directly from smooth data in the library. However, determining the equivalence cross section Σ_e considering the geometrical configuration is more complicated. Before describing how the equivalence cross section is obtained, the subgroup method is briefly introduced.

2.2.2. *The Subgroup Method*

The essential is that the numerator and denominator of Eq. 2.1 are approximated by quadratures in the absorption cross section.
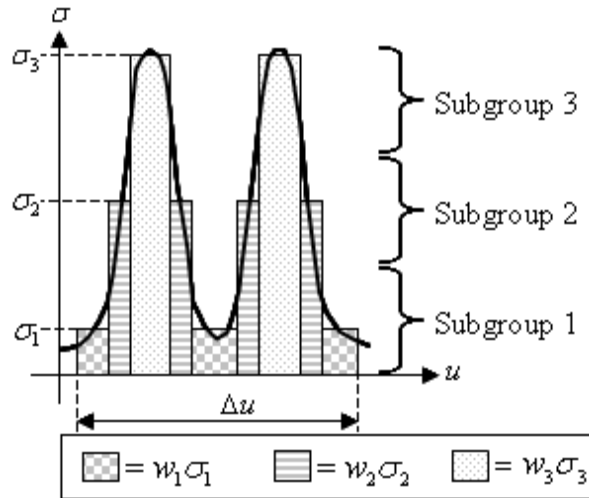
Fig. 2.3. Subgroup data structure

Since the background cross section is constant within a group, Eq. 2.3 can be written with microscopic ones as follows:

$$\phi(u) = \frac{\sigma_b}{\sigma_a(u) + \sigma_b}$$

The lethargy dependence of the flux of Eq. 2.4 is uniquely through $\sigma_a(u)$. This is essential for the subgroup method. It allows to replace the integration variable u by σ_a and to approximate the integrals by quadratures in σ_a according to the following equations:

$$\frac{1}{\Delta u} \int_{\Delta u} f(u) du = \frac{1}{\Delta u} \int_{\Delta u} f(\sigma_a) \frac{du}{d\sigma_a} d\sigma_a \cong \sum_n \omega_n f_n$$

Eq. 2.5

where $f_n = f(\sigma_n)$ are the integrands at the discrete values of σ_a. As shown in Fig. 2.3, the resonance cross section is subdivided with σ_{an}'s over the σ_a range and their weights (ω_n).

Therefore the resonance cross section in Eq. 2.1 can be approximated by the quadrature set of σ_{an} and ω_n as follows:

$$\sigma_a = \frac{\sum_{n=1}^{N} \omega_n \sigma_{an} \phi_n}{\sum_{n=1}^{N} \omega_n \phi_n}$$

Eq. 2.6

N and σ_{an} are arbitrarily chosen to produce accurate effective cross sections. In DeCART, the number of subgroups is set to 7. The scalar fluxes, ϕ_n, correspond to a fixed level of absorption σ_{an}, are unknown and have to be obtained from the heterogeneous transport calculations. In DeCART, in order to reduce the number of heterogeneous transport calculations, a detour via a parametrization of the absorption level through the background cross section σ_b instead of directly using the fluxes ϕ_n is used.

2.2.3. *Determination of the Equivalence Cross Section*

Due to the weak lethargy dependence of the equivalence cross sections, the background cross section is itself lethargy dependent and can be expressed as follow:

$$\phi(u) = \frac{\sigma_b(u)}{\sigma_a(u) + \sigma_b(u)} \Rightarrow \sigma_b(u) = \frac{\sigma_a(u)\phi(u)}{1 - \phi(u)}$$

Eq. 2.7

M heterogeneous transport calculations are performed with different absorption level (σ_m, m=1,..,M). In DeCART, M is set to 4. Practically, in DeCART, the fixed source heterogeneous calculations are performed for each different plane, assuming no axial leakage and a homogeneous temperature:

$$\hat{\Omega}_n \cdot \nabla \varphi_{ng}(\vec{r}) + \Sigma_{rg}(\vec{r}) \varphi_{ng}(\vec{r}) = \frac{1}{4\pi} Q_g(\vec{r})$$

Eq. 2.8

where 'g' is an energy group and 'n' the angle. The source in is obtained by

$$Q_g = \lambda_g \Sigma_{pg}$$

Eq. 2.9

The removal cross section is calculated by

$$\Sigma_{rg} = N_i \sigma_{mg} + \lambda_g \Sigma_{pg}$$

Eq. 2.10

The transport calculations provide, for a given absorption level σ_m, a scalar flux ϕ_g. Using Eq. 2.7, the background cross section is determined by the Eq. 2.11:

$$\Sigma_{bg}(\sigma_{mg}) = \frac{\Sigma_{ag}(\sigma_{mg})\phi_g}{1-\phi_g}$$

Eq. 2.11

And the equivalence cross section for a given absorption level, easily follows as:

$$\Sigma_{eg}(\sigma_{mg}) = \Sigma_{bg}(\sigma_{mg}) - \lambda_g \Sigma_{pg} \quad m = 1,..,M$$

Eq. 2.12

2.2.4. _Determination of the effective macroscopic resonance cross section._

By combining Eq. 2.4 and Eq. 2.6, the effective microscopic resonance cross section can be obtained by Eq. 2.13 provided that the corresponding background cross section σ_{bn} to σ_{an} is known:

$$\sigma_a = \frac{\sum_n w_n \sigma_{an} \dfrac{\sigma_{bn}}{\sigma_{an}+\sigma_{bn}}}{1-\sum_n w_n \dfrac{\sigma_{an}}{\sigma_{an}+\sigma_{bn}}}$$

Eq. 2.13

Since the subgroup data σ_{an}'s are given, the corresponding σ_{bn}'s are obtained by linear interpolation in $ln(\sigma_m)$ reducing the number of transport calculations needed from 7 by resonance energy group to 4 by energy group.

The last step of the determination of resonance effective cross section is to generate the region-wise macroscopic cross section which takes into account both spatial and energy self shielding. The macroscopic cross section is computed in the Eq. 2.14, assuming that the equivalence cross section is known:

$$\Sigma_a = \frac{\sum_n w_n \dfrac{\Sigma_{an}\Sigma_{bn}}{\Sigma_{an}+\Sigma_{bn}}}{1-\sum_n w_n \dfrac{\Sigma_{an}}{\Sigma_{an}+\Sigma_{bn}}}$$

Eq. 2.14

with

$$\Sigma_{an} = N\sigma_{an}$$
$$\Sigma_{bn} = N\sigma_{bn} = \lambda N\sigma_p + \Sigma_e(\sigma_{an})$$

Eq. 2.15

The resonance treatment presented above assumed that only one resonant isotope was present in each spatial region. If more than one isotope is present, the interactions between the resonances of the different isotopes need to be resolved to properly predict energy and spatial self-shielding. In the subgroup method, only two cases are considered

and correspond to the extreme limits of no or full overlap between the resonances. The details on how to handle the interaction between isotopes are beyond the scope of the dissertation and can be found in (Stamm'Ler and Abbate 1983).

```
┌─────────────────────────┐              ┌──────────────────────┐
│ Read the required data  │◄─────────────│ Cross section library│
│        λᵢσᵢₚ            │              └──────────────────────┘
│     subgroup data       │
│  (wₙ, σₐₙ, σᵥfₙ, σₘ)    │
└─────────────────────────┘
             │
             ▼
┌─────────────────────────┐
│ Macroscopic cross section│
│  for transport calculation│
│   -  λΣₚ, Σᵣ(σₘ)        │
└─────────────────────────┘
             │
             ▼
┌─────────────────────────┐
│  Fixed source Transport │
│  calculation at resonance│
│   -  scalar flux (φₘ)   │
└─────────────────────────┘
             │
             ▼
┌─────────────────────────┐
│ Table for the equivalence│
│     cross section       │
│      -  Σₑ(σₘ)          │
└─────────────────────────┘
             │
             ▼
┌─────────────────────────┐
│  Assume Σᵢₓ⁽⁰⁾=0.0      │
└─────────────────────────┘
             │
             ▼
┌─────────────────────────┐
│  Calculate the effective│
│  resonance cross section│
│      σᵢₐ , νσᵢf         │
└─────────────────────────┘
             │
             ▼
┌─────────────────────────┐
│   Update Σᵢₓ⁽ˡ⁺¹⁾       │
└─────────────────────────┘
             │
             ▼
┌─────────────────────────┐
│  Check the convergence  │
└─────────────────────────┘
             │
             ▼
┌─────────────────────────┐
│          End            │
└─────────────────────────┘
```
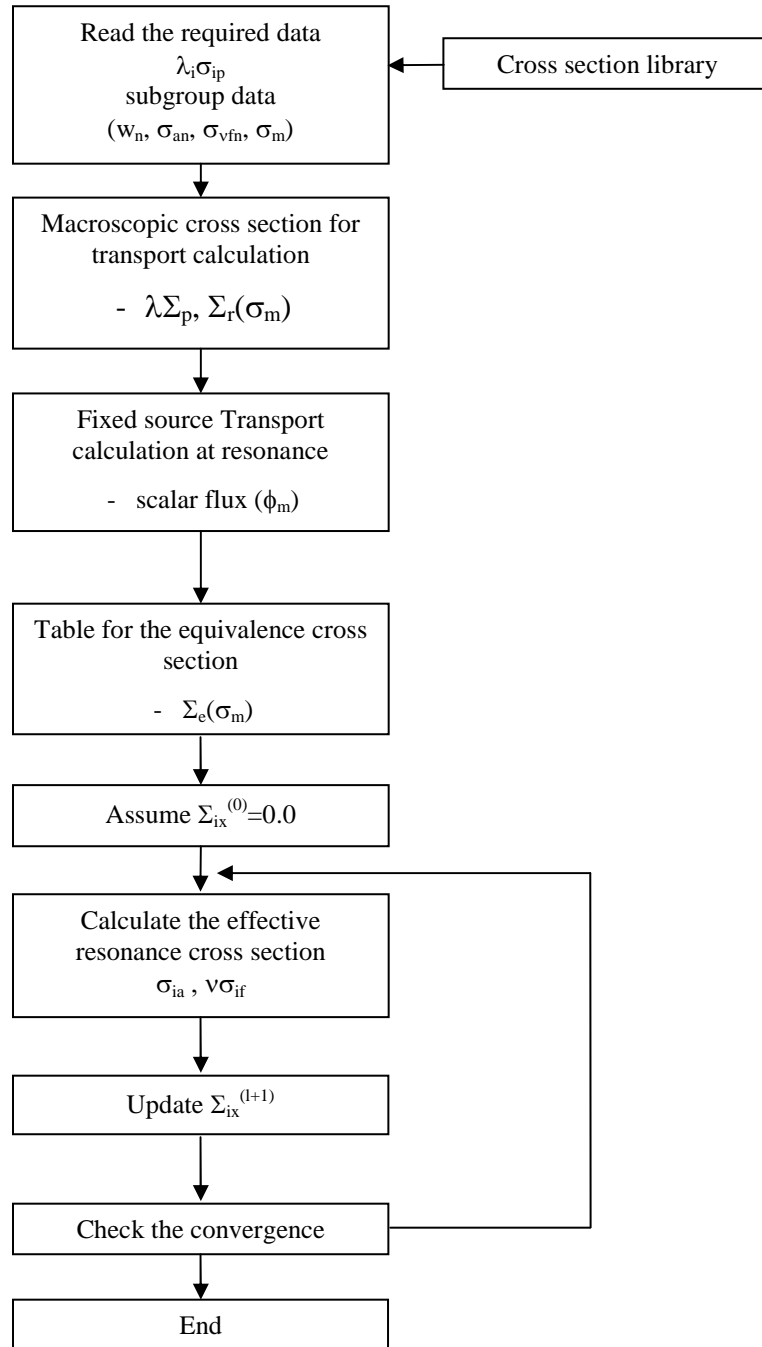
Fig. 2.4. DeCART flow chart for resonance calculation

2.2.5. *Calculation sequence for resonance treatment*

The resonance calculation module begins with reading the smooth cross section and the subgroup data from the library as shown in Fig. 2.4. Fixed source heterogeneous

transport calculation is performed to obtain the scalar flux according to the 4 levels of absorption cross sections. The calculated scalar fluxes are converted into the equivalence cross sections, and those are tabularized as functions of the absorption cross section. To consider the influence of the absorption cross section from the other resonance nuclides, the iteration process is required. Iteration process includes the assumption of zero absorption cross section from other nuclides at the beginning and the resonance absorption cross sections are updated until the spectrums are converged.

The end result of the resonance calculation module is a library of effective cross sections tabulated as functions of the absorption level and temperature. During the actual neutron transport module of DeCART, the local macroscopic cross sections for a given flat source region is evaluated using the Eq. 2.14.

Now that the handling of spatial and energy self-shielding has been understood, the macroscopic cross sections are determined and the transport calculation itself can be performed.

2.3. Steady State Methodology

2.3.1. The 2-D Method of Characteristics.

The formulation begins with the 3-D steady-state Boltzmann transport equation for the solution of the angular flux distribution per unit volume, solid angle and energy $\varphi(\mathbf{r},\mathbf{\Omega},E)$:

$$\mathbf{\Omega}\cdot\nabla\varphi(\mathbf{r},\mathbf{\Omega},E)+\Sigma(\mathbf{r},E)\varphi(\mathbf{r},\mathbf{\Omega},E)=q(\mathbf{r},\mathbf{\Omega},E) \qquad \text{Eq. 2.16}$$

where the source term consists of fission and scattering events:

$$q(\mathbf{r},\mathbf{\Omega},E)=\frac{1}{4\pi}\frac{\chi(\mathbf{r},E)}{k_{eff}}\int_0^\infty dE'\nu\Sigma_f(\mathbf{r},E')\phi(\mathbf{r},E')$$

$$+\int_0^\infty dE'\int_{4\pi}d\mathbf{\Omega}'\Sigma_s(\mathbf{r},\mathbf{\Omega}'\to\mathbf{\Omega},E'\to E)\varphi(\mathbf{r},\mathbf{\Omega}',E') \qquad \text{Eq. 2.17}$$

In DeCART, the scattering source is assumed to be isotropic in the lab system, so Eq. 2.17 can be simplified:

$$q(r,\Omega,E)=\frac{\chi(r,\Omega,E)}{4\pi k_{eff}}\int_0^\infty \nu\Sigma_f(r,E')\phi(r,E')dE'+\frac{1}{4\pi}\int_0^\infty \Sigma_{s,E'\to E}(r,E')\phi(r,E')dE' \qquad \text{Eq. 2.18}$$

and the scalar flux $\phi(\mathbf{r},E)$ is given by:

$$\phi(\mathbf{r},E)=\int_{4\pi}\varphi(\mathbf{r},\Omega,E)d\Omega \qquad \text{Eq. 2.19}$$

The 3-D Boltzmann equation is integrated axially over a plane of thickness h_z. The result is:

$$\left(\sin\theta\cos\alpha\frac{\partial}{\partial x} + \sin\theta\sin\alpha\frac{\partial}{\partial y} \right)\bar{\varphi}\left(\mathbf{r_r},\mathbf{\Omega},E\right)$$

$$+ \bar{\Sigma}\left(\mathbf{r},E\right)\bar{\varphi}\left(\mathbf{r_r},\mathbf{\Omega},E\right) = \hat{q}\left(\mathbf{r_r},\mathbf{\Omega},E\right),$$

Eq. 2.20

where $\mathbf{r_r}$ is the position vector in 2-D, α is the azimuthal angle, and θ is the polar angle. The over-bar indicates axial integration; for instance, the 2-D averaged angular flux is given by:

$$\bar{\varphi}\left(\mathbf{r_r},\mathbf{\Omega},E\right) = \frac{1}{h_z}\int_{h_z}\varphi\left(\mathbf{r},\mathbf{\Omega},E\right)dz,$$

Eq. 2.21

and the effective source term is given by:

$$\hat{q}\left(\mathbf{r_r},\mathbf{\Omega},E\right) = \bar{q}\left(\mathbf{r_r},\mathbf{\Omega},E\right) - L_z\left(\mathbf{r_r},\mathbf{\Omega},E\right)$$

Eq. 2.22

The axial leakage is given by:

$$L_z\left(\mathbf{r_r},\mathbf{\Omega},E\right) = \frac{\mu}{h_z}\left(\varphi_T\left(\mathbf{r},\mathbf{\Omega},E\right) - \varphi_B\left(\mathbf{r},\mathbf{\Omega},E\right)\right)$$

Eq. 2.23

L_z was obtained directly from the integration in Eq. 2.16 and was moved to the right-hand side. In the expression for L_z, φ_T and φ_B are the angular fluxes from the top and bottom surfaces of the plane and $\mu = \cos\theta$. One of the major approximations of the 2D-1D methodology resides in the evaluation of φ_T and φ_B. If these fluxes were obtained from the solution of the 3-D Boltzmann equation, then there would be no approximation in Eq. 2.20. However, in DeCART, these angular fluxes are approximated from the axial 1-D diffusion based solution. Currently, the axial angular flux distribution is obtained by a double-P_0 approximation, which basically assumes an isotropic axial leakage. The axial leakage is then expressed as a function of incoming and outgoing partial currents at the top and bottom surfaces of the considered plane:

$$\frac{\mu}{h_z}\left(\varphi_T\left(\mathbf{r_r},\mathbf{\Omega},E\right) - \varphi_B\left(\mathbf{r_r},\mathbf{\Omega},E\right)\right) \cong \begin{cases} \dfrac{\mu}{\pi h_z}\left(j_g^{T,out} - j_g^{jB,in}\right) & \text{for } \mu \geq 0 \\[2mm] \dfrac{\mu}{\pi h_z}\left(j_g^{T,in} - j_g^{B,out}\right) & \text{for } \mu < 0 \end{cases}$$

Eq. 2.24

where $j^{T,out}$ and $j^{T,in}$ are the partial outgoing and incoming currents at the top surface, and $j^{B,out}$ and $j^{B,in}$ are the corresponding values at the bottom surface. The effect of this approximation will be the focus of a detailed investigation in this thesis.

The next step is to rewrite the 2-D position vector $\mathbf{r_r}$ as the sum of two vectors: an arbitrary starting vector $\mathbf{r_{r0}}$ and the component $\mathbf{r_r}$ projection of the transport angle onto the plane, $\mathbf{\Omega_r}$. That is, $\mathbf{r_r} = \mathbf{r_{r0}} + s\mathbf{\Omega}$, where s is the distance traveled from $\mathbf{r_{r0}}$ to $\mathbf{r_r}$ along the $\mathbf{\Omega_r}$ direction. This yields a differential equation in the single variable s, for which an analytic solution is given by:

$$\bar{\varphi}\left(\mathbf{r_r},\mathbf{\Omega_r},E\right) = \bar{\varphi}\left(\mathbf{r_{r,0}},\mathbf{\Omega_r},E\right)\exp\left(-\frac{\bar{\Sigma}(E)s}{\sin\theta}\right) + \frac{\hat{q}\left(\mathbf{\Omega_r},E\right)}{\Sigma(E)}\left[1 - \exp\left(-\frac{\bar{\Sigma}(E)s}{\sin\theta}\right)\right]$$

Eq. 2.25

The evaluation of Eq. 2.25 is performed on a discrete spatial mesh where the multigroup cross sections are uniform and the source distribution is flat.
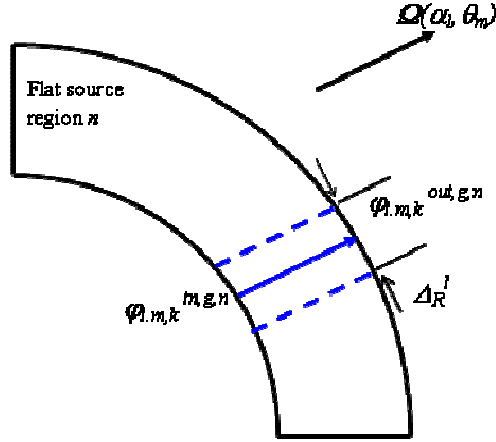
Fig. 2.5. Ray Tracing through a discrete region

Rays are traced across these flat source regions along various directions given by $\mathbf{\Omega}=\mathbf{\Omega}(\alpha_l,\theta_m)$. For a given direction, there are several parallel rays that pass through a particular flat source region. Consider the nth flat source region as depicted in Fig. 2.5. Suppose that the kth ray segment is of orientation $\mathbf{\Omega}(\alpha_l,\theta_m)$ and lies in region n. This segment has length $s_{l,k}^n$ and is considered to have a width equal to the ray spacing Δ_R^l. Suppose that the problem domain is discretized into N flat source regions, L azimuthal angles, M polar angles and G energy groups. The expression for the outgoing angular flux, $\varphi_{l,m,k}^{out,g,n}$ at the region boundary can be written in terms of the incoming angular flux $\varphi_{l,m,k}^{in,g,n}$ as:

$$\varphi_{l,m,k}^{out,g,n} = \varphi_{l,m,k}^{in,g,n}\exp\left(-\frac{\Sigma_g^n s_{l,k}^n}{\sin\theta_m}\right) + \frac{q_m^{g,n}}{\Sigma_g^n}\left[1-\exp\left(-\frac{\Sigma_g^n s_{l,k}^n}{\sin\theta_m}\right)\right] \qquad \text{Eq. 2.26}$$

The ray segment k makes a contribution to the angular flux in the band of width Δ_R^l and length $s_{l,k}^n$ shown in Fig. 2.5. The average angular flux in this band is obtained by integrating Eq. 2.25 over the track length s:

$$\overline{\varphi}_{l,m,k}^{g,n} = \frac{\varphi_{l,m,k}^{in,g,k}-\varphi_{l,m,k}^{out,g,n}}{\Sigma_g^n s_{l,k}^n / \sin\theta_m} + \frac{q_m^{g,n}}{\Sigma_g^n} \qquad \text{Eq. 2.27}$$

There are several ray segments that contribute to the angular flux in region n. The angular flux in the region is given as a summation of contributions from all rays segments lying in region n :

$$\overline{\varphi}_{l,m}^{g,n} = \frac{\displaystyle\sum_{k\in n}\overline{\varphi}_{l,m,k}^{g,n}s_{l,k}^n\Delta_R^l}{\displaystyle\sum_{k\in n}s_{l,k}^n\Delta_R^l} \qquad \text{Eq. 2.28}$$

The segment length $s_{l,k}{}^n$ is adjusted so that the denominator of Eq. 2.27 equals the physical region volume V_n. The scalar flux is obtained by integrating Eq. 2.28 with respect to angle:

$$\phi_g^n = \sum_m w_m \sum_l w_l \bar{\varphi}_{l,m}^{g,n}$$

Eq. 2.29

where w_m and w_l are weights for the polar and azimuthal angle, respectively.

2.3.2.   *1-D axial diffusion solvers*

The 1-D diffusion equation for energy group g is:

$$-D_g \frac{d^2\phi_g(z)}{dz^2} + \Sigma_{r\,g}\phi_g(z) = Q_g(z)$$

Eq. 2.30

Q_g is the total source, including fission, scattering and radial transverse leakage. The latter quantity is determined by the 2-D MOC calculation. DeCART has 2 available nodal methods to solve the Eq. 2.30.

2.3.2.1.   *Nodal Expansion Method (NEM)*

In DeCART, NEM is derived for the 1-node problem. The main approximation of NEM is that the solution of Eq. 2.30 can be represented by a 4th order polynomial:

$$\phi(u) = \sum_{i=0}^{4} \phi_i f_i(u)$$

Eq. 2.31

The derivation of the NEM expression then involves selecting an appropriate set of basis functions, $f(u)$ where $u=z/h_z$, and then determining the coefficients of the polynomial. DeCART uses a set of orthogonal polynomials defined on the interval [0,1] as the basis functions. The basis are the polynomials proposed by (Finnemann, Bennewitz et al. 1977).

There are 5 unknowns per spatial mesh (ϕ_i) to be determined, so 5 constraints are needed:

- Current continuity at each face of the considered mesh
- Neutron balance equation (Eq. 2.30)
- 2 weighted residual balance equations which are obtained by in multiplying the neutron balance equation by f_i and integrating it over [0,1].

The resulting set of equations relates the node average flux ϕ_0 with the partial currents at the top and bottom surfaces of the node, as well as the first and second flux moments $\tilde{\phi}_1$ and $\tilde{\phi}_2$ defined as follow:

$$\tilde{\phi}_i = \int_0^1 \varphi(u) f_i(u)\,du$$

Eq. 2.32

After the 5 unknowns have determined, the outgoing partial currents at the surface of a spatial mesh can be expressed as follow:

$$j_z^{+T,k} = T_1^k j_z^{-T,k} + T_2^k j_z^{-B,k} + T_3^k \overline{\phi}^k + T_4^k \phi_1^{\%} + T_5^k \phi_2^{\%}$$

where

$$T_1^k = \frac{1 - 960\beta_k^2}{(1 + 40\beta_k)(1 + 24\beta_k)}, \quad T_2^k = \frac{-16\beta_k}{(1 + 40\beta_k)(1 + 24\beta_k)}, \quad T_3^k = \frac{20\beta_k}{(1 + 40\beta_k)},$$

$$T_4^k = \frac{30\beta_k}{(1 + 24\beta_k)}, \quad T_5^k = -\frac{70\beta_k}{(1 + 40\beta_k)}.$$

In this expression, j_z^k is a partial current in the axial direction for spatial mesh k, the $\pm$ superscripts imply incoming or outgoing current and the T and B superscripts refer to the top and bottom of the mesh, respectively. The average flux is $\overline{\varphi}^k$, the first and second flux moments are $\phi_1^{\%}$ and $\phi_2^{\%}$, and the ratio of the diffusion coefficient to the node size is denoted β_k.

2.3.2.2.   *Semi Analytical Nodal Method (SANM)*

The semi analytic nodal method is also derived for a single spatial mesh starting from Eq. 2.30. However, instead of assuming that a 4th order polynomial can satisfy the solution, it is assumed that only the source term of Eq. 2.30 is represented by a 4th order polynomial.

$$Q(u) \cong \sum_{i=0}^{4} q_i P_i(u)$$

In the typical SANM formulation, the polynomial basis is composed of the 5 first Legendre polynomials and $u = 2z/h_z$.

Eq. 2.30 can then be solved analytically to provide that following expression for the scalar flux:

$$\phi(u) \cong \sum_{i=0}^{4} a_i P_i(u) + a_5 \sinh\left(\frac{h_z}{2}\sqrt{\frac{\Sigma_r}{D}} u\right) + a_6 \cosh\left(\frac{h_z}{2}\sqrt{\frac{\Sigma_r}{D}} u\right)$$

The hyperbolic functions arise from the homogenous part of the solution, and the linear combination of Legendre polynomials represents the particular part of the solution to the Eq. 2.30. The rest of the steps in deriving the final expression for the SANM solution are similar to those required by NEM. An additional step is required in which the hyperbolic part of the solution is projected on the Legendre Polynomial basis in order to properly compute the source term $Q(z)$. The details of NEM and SANM implementations in DeCART are beyond the scope of the dissertation but can be found in (Joo, Cho et al. 2004; Thomas 2006).

2.3.3.   3-D Global Solution Strategy

As mentioned previously, a 3-D solution is obtained by coupling a set of 2-D MOC planar problems to a set of 1-D fuel rod wise diffusion problem. The coupling is

through transverse leakage which modify respectively the source terms of the Eq. 2.16 and Eq. 2.30. However, because transverse leakage represents a weak coupling between the 2-D and 1-D solutions; and because of the computational cost of every MOC sweep, a CMFD approach was implemented to provide an effective acceleration to the transport calculation. Even though the CMFD framework is not needed to obtain a 3-D solution and can be turned off completely, its fast converging properties makes it an important piece of the DeCART methodology.

The 3-D CMFD kernel in DeCART is formulated as a nodal neutron balance equation shown below for a homogenized node m. The coarse mesh node in DeCART is understood to be an axial slice of a pin cell as shown in Fig. 2.1 with the node average scalar flux, $\overline{\phi}$, being the solution to the CMFD linear system of equations.

$$\sum_{s=1}^{N_{rad}^m} J_{rad}^{m,s} A_{rad}^s + \sum_{s=1}^{N_z^m} J_z^{m,s} A_z^s + \overline{\Sigma}_r^m \overline{\phi}^m V^m = \overline{S}^m V^m \qquad \text{Eq. 2.37}$$

In Eq. 2.37, $J_{rad}^{m,s}$ and $J_z^{m,s}$ are the surface average currents in the radial and axial directions, respectively, normal to node surface s with area A. The symbols $\overline{\phi}^m$, $\overline{\Sigma}_r^m$ and $\overline{S}^m$ represent the node average flux, removal cross section, and source which includes fission and scattering. Finally, V is the node volume and N_{rad}^m and N_z^m are the number of neighboring nodes in the radial and axial directions.

The node averaged terms of Eq. 2.37 are all obtained through flux-volume weighted homogenization techniques using the higher order solution provided by the 2-D MOC solution. The expression for the surface averaged radial net currents is given as:

$$J_{rad}^{m,s} = -\tilde{D}^{m,s}\left(\overline{\phi}^{l(m)} - \overline{\phi}^m\right) - \hat{D}^{m,s}\left(\overline{\phi}^{l(m)} + \overline{\phi}^m\right) \qquad \text{Eq. 2.38}$$

where $\overline{\phi}^m$ is the node averaged scalar flux for the m node and $\overline{\phi}^{l(m)}$ is the node averaged scalar flux of the node neighboring node m on the s side. $\tilde{D}^{m,s}$ and $\hat{D}^{m,s}$ are the radial coupling coefficients which represent the coefficient for the normal finite difference approximation and a higher-order current correction factor, respectively. $\tilde{D}^{m,s}$ is taken as the conventional definition of the diffusion coefficient, whereas $\hat{D}^{m,s}$ can only be determined by the MOC solution. Note that the inclusion of the higher order current correction factor allows for the CMFD solution to exactly reproduce the 2-D MOC transport solution.

Just as the radial currents were provided by a higher order 2-D solution, the axial currents are also provided by the 1-D solution of a higher order nodal method (NEM, SANM) used for the axial direction. As shown in Eq. 2.33, the response matrix for NEM and SANM may be formulated to provide the axial current directly. The result of this formulation is that the final equations for the 1-D solvers can be imbedded directly into the CMFD kernel by substitution into Eq. 2.37 and lead to the following formulation:

$$-\frac{1}{h_z}\sum_{s=1}^{N_{rad}^m}\left(\tilde{D}^{m,s}+\hat{D}^{m,s}\right)\bar{\phi}^{l(m)}+\left(\frac{2T_3^m}{h_z}+\bar{\bar{\Sigma}}_r^m+\sum_{s=1}^{N_{rad}^m}\left(\tilde{D}^{m,s}-\hat{D}^{m,s}\right)\right)\bar{\phi}^m=\ldots$$

Eq. 2.39

$$\bar{S}^{l,k}-\frac{1}{h_z}\left(T_1^m+T_2^m-1\right)\left(j_z^{-T,m}+j_z^{-B,m}\right)-\frac{2T_5^m}{h_z}\tilde{\phi}_2^m$$

$\tilde{\phi}_2^m$ and T_i^m are defined in the Eq. 2.32 and Eq. 2.34 above. When the formulation of the Eq. 2.39 is used, no separate solution of for the fuel rod wise 1-D axial problem is required, only the set of 2-D planar MOC equations and the global solution of the Eq. 2.39 are needed to get a 3-D flux solution.

2.3.4. *Known Issues of original 2D/1D formulation*

Recently, the DeCART code and the 2D-1D algorithm have been applied to problems where neutron streaming plays a major role. Some examples of such problems are gas cooled reactor applications, the analysis of a Loss Of Coolant Accident (LOCA) where severe voiding occurs or the modeling of high void region in a BWR modeling have resulted in some cases (Thomas 2006) in which the 3-D solution does not converge. Other convergence issues have been observed when the size of the axial mesh is reduced. The DeCART convergence issues reveal that the basic 2D-1D algorithm, although highly successful on most problems, requires investigations for robustness of convergence. Those investigations are presented in Chapter 3.

Another issue of the 2D-1D algorithm is related to the axial 1-D solver. The presence of heterogeneity in the axial direction, such as partially inserted control assemblies, severe void variations, part length fuel rods, and axial enrichment zoning can lead to 3-D solutions of poor accuracy (Cho, Kim et al. 2006). The current 2D-1D algorithm available in DeCART only provides 1-D axial solution based on the diffusion theory whose accuracy deteriorates in cases of strong flux gradients such as the ones observed for the problems listed above. The addition of a transport based solver is the subject of Chapter 4.

2.4. Transient Methodology

This section briefly describes the main features of the transient implementation in DeCART. It is a summary of (Cho, Kim et al. 2005) and is included in the dissertation as a starting point for the development of a transient methodology able to include thermal hydraulic feedbacks.

The analysis of the time dependent neutron transport requires the coupled solution of a few equations, the time dependent Boltzmann equation as well as the temporal variation of the neutron precursor's population, per spatial mesh. Given the roles of the CMFD and MOC steady-state solvers described in the section 2.3 above, the planar 2-D MOC solution as well as the CMFD formulation can be extended readily to solve the time-dependent Boltzmann equation. It is possible to make most of the transient calculations be carried out by the CMFD calculation by limiting the MOC calculation to update the intra-cell regional flux shapes and the radial cell coupling coefficients. Since

the intra-cell flux shape would not vary much unless there is a significant change in the material composition of the cell itself or its neighbors.

The time discretization is performed for the time dependent 3-D CMFD neutron balance equation to formulate a transient fixed source problem (TFSP). The 3-D TFSP is solved with the embedded nodal method (NEM or SANM) based axial solution kernel which takes care of the axial variation of the flux within the large axial node. If requested, the MOC calculation is performed only when there are significant changes in the local composition at the current time step. This intermittent MOC calculation based on the monitoring of the composition change is referred to as the conditional MOC update. As much as CMFD wasn't required to perform steady state calculation, it is the cornerstone of the DeCART transient solver.

2.4.1. *Governing equations*

Three families of equations are solved by DeCART during transient analysis: the diffusion equation which is solved by the CMFD method, the time dependent transport equation solved by the MOC method and the equations describing the evolution of the precursor's concentration solved to compute the delayed neutron source. All three equations are described in the following sections.

The discretized time dependent neutron diffusion equation for the spatial mesh m and the energy group g is:

$$\frac{1}{v_g^m}\frac{d\phi_g^m}{dt} = \chi_{pg}(1-\beta^m)\psi^m + \chi_{dg}S_d^m + \sum_{\substack{g'=1\\g'\neq g}}^{G}\Sigma_{s,g<-g'}^m\overline{\phi}_{g'}^m\ldots$$

$$\ldots -\left(\sum_{u=x,y,z}\frac{1}{h_u^{l,k}}\left(J_{gu}^{m+} - J_{gu}^{m-}\right) + \Sigma_{rg}^m\overline{\phi}_g^m\right)$$

Eq. 2.40

where

$$\psi^m = \frac{1}{k_{eff}}\sum_{g'=1}^{G}\upsilon_{dgk}\Sigma_{f,g'}^m\overline{\phi}_{g'}^m$$

$$S_d^m = \sum_{k=1}^{K}\lambda_k C_k^m$$

Eq. 2.41

ψ^m represents the total fission source, S_d^m the delayed neutron source and C_k^m is the precursor k concentration. K represents the number of precursors and λ_k is its associated decay time constant. $J_{gu}^{m\pm}$ is the surface average current along direction u at the positive and negative side surfaces of the node m defined by the CMFD relation, the Eq. 2.38. G represents the number of energy groups. The details of the discretization and solution of the transient equations are given in the following sections.

2.4.1.1. *Time discretization*

The theta method is used to discretize the time derivative term in the Eq. 2.40:

$$\frac{\bar{\phi}_g^{m,n} - \bar{\phi}_g^{m,n-1}}{v_g^m \Delta t_n} = \theta R_g^{m,n} + (1-\theta)R_g^{m,n-1} \qquad \text{Eq. 2.42}$$

with n represents the time index, $R_g^{m,n}$ denoting the RHS of Eq. 2.42 at time step n. Typically, the crank Nicholson scheme is used ($\theta=0.5$).

2.4.1.2. Delayed Neutron Source Approximation

The evolution of a given precursor concentration with time is governed by:

$$\frac{dC_k^m}{dt} = \beta_k^m \psi^m - \lambda_k C_k^m \qquad \text{Eq. 2.43}$$

β_k^m is the fraction of delayed neutron produced by precursor k. The first term on the right hand side (RHS) represents the source term by fission ψ^m defined in Eq. 2.41 and the second term the loss term by beta decay.

It was shown in (Keepin, Wimmett et al. 1957) that it is not required to keep track all of the neutron precursors (about 40 element produce delayed neutron with different decay constants), and that just six representative precursors are needed to properly capture the delayed neutrons effect. Consequently, seven equations need to be solved per spatial mesh. To further reduce the computational burden, a second order precursor integration technique (Downar, Xu et al. 2006) is used which is an approximate technique to avoid the time differencing of the precursor equation. The precursor's concentrations and their contribution to the delayed neutron source are evaluated using a second order approximation of the time variation of the fission source during the current time step.

The delayed neutron source can then be expressed as follow:

$$S_d^{m,n} = \sum_{k=1}^{K} \lambda_k C_k^{m,n-1} e^{-\lambda_k \Delta t_n} + \sum_{l=n-2}^{n} \sum_{k=1}^{K} \beta_k^m \Omega_k^{m,l} \psi^{m,l} = \tilde{S}_d^{m,n-1} + \omega^{m,n} \psi^{m,n} \qquad \text{Eq. 2.44}$$

where

$$\Omega_k^{n-1} = \frac{1}{\lambda_k \Delta t_{n-1}} \left(\kappa_k + 1 + \frac{1-\kappa_k}{\gamma}\left(1 - \frac{2}{\lambda_k \Delta t_{n-1}}\right) \right) - \kappa_k$$

$$\Omega_k^n = 1 - \frac{2}{(\gamma+1)\lambda_k \Delta t_{n-1}} + \frac{1-\kappa_k}{\gamma(\gamma+1)\lambda_k \Delta t_{n-1}}\left(\frac{2}{\lambda_k \Delta t_{n-1}} - 1\right) \qquad \text{Eq. 2.45}$$

$$\tilde{S}_d^{m,n-1} = \sum_{k=1}^{K} \kappa_k \lambda_k C_k^{m,n-1} + \sum_{l=n-2}^{n-1} \sum_{k=1}^{K} \beta_k^m \Omega_k^{m,l} \psi^{m,l}$$

$$\omega^{m,n} = \sum_{k=1}^{K} \beta_k^m \Omega_k^{m,n}$$

and the following constants, $\kappa_k = e^{-\lambda_k \Delta t_n}$ and $\gamma = \frac{\Delta t_n}{\Delta t_{n-1}}$.

By an additional storage of the node-wise fission source over the past 2 time steps, it is possible to avoid the solution of the system of 6 coupled differential equations.

2.4.1.3.   Multi-group CMFD transient fixed source formulation

By inserting Eq. 2.42 and Eq. 2.44 into Eq. 2.40, the TFSP for the CMFD can be written as follow:

$$\sum_{u=x,y,z} \frac{1}{h_u^m} \left(J_{gu}^{m+} - J_{gu}^{m-} \right) + \left(\Sigma_{rg}^m + \frac{1}{\theta v_g^m \Delta t_n} \right) \overline{\phi}_g^{m,n} = \left(\chi_{pg}(1 - \beta^{m,n}) + \chi_{dg}\omega^{m,n} \right) \psi^m$$

$$+ \sum_{\substack{g'=1 \\ g' \neq g}}^G \Sigma_{s,g'\leftarrow g}^m \overline{\phi}_{g'}^{m,n} + \frac{\overline{\phi}_g^{m,n-1}}{\theta v_g^m \Delta t_n} + \chi_{dg}\widetilde{S}_d^{m,n-1} + \Theta R_g^{m,n-1}$$

<div align="right">Eq. 2.46</div>

The RHS of Eq. 2.46 represents the fixed source of spatial mesh *m*. The source term consists of five terms: the usual fission and scattering source terms as well as three transient specific terms, the previous flux term, the delayed neutron source term, and the residual term. The residual term representing the imbalance at the previous time should be evaluated to establish the fixed source problem. Provided that the previous time step scalar fluxes, delayed neutron source and residuals are stored, it is possible to use the steady-state CMFD solver with a modified source term to perform transient calculation.

2.4.1.4.   MOC transient fixed source formulation

In the framework of the 2D-1D methodology, the time dependent form of the planar transport equation, obtained by axial integration of the 3D time dependent Boltzmann equation can be written as follow for angle *w*, spatial mesh *m* and energy group *g*:

$$\frac{1}{v_g} \frac{\partial \varphi_g^{w,m}}{\partial t} = \frac{1}{4\pi} \left(\chi_{pg}(1-\beta^m)\psi^m + \chi_{dg}S_d^m + \sum_{g'=1}^G \Sigma_{s,g'\leftarrow g}^m \overline{\phi}_{g'}^m \right) - \frac{\mu_w}{h_z} \left(\varphi_{T,g}^{w,m} - \varphi_{B,g}^{w,m} \right)$$

$$- \left(\sin(\theta)\cos(\alpha) \frac{\partial \varphi_g^{w,m}}{\partial x} + \sin(\theta)\sin(\alpha) \frac{\partial \varphi_g^{w,m}}{\partial y} + \Sigma_{tg}^m \varphi_g^{w,m} \right)$$

<div align="right">Eq. 2.47</div>

Eq. 2.47 is the discretized, time-dependent version of Eq. 2.20. ψ^m and S_d^m have the same definition that in section 2.4.1.3. Using the temporal discretization discussed in section 2.4.1.1, a TFSP for the planar Boltzmann equation is obtained:

$$\sin(\theta)\cos(\alpha) \frac{\partial \varphi_g^{w,m,n}}{\partial x} + \sin(\theta)\sin(\alpha) \frac{\partial \varphi_g^{w,m,n}}{\partial y} + \left(\Sigma_{tg}^m + \frac{1}{\theta v_g \Delta t_n} \right) \varphi_g^{w,m,n} = \ldots$$

$$\ldots \frac{1}{4\pi} \left(\chi_{pg}(1-\beta^m)\psi^{m,n} + \chi_{dg}S_d^{m,n} + \sum_{g'=1}^G \Sigma_{s,g'\leftarrow g}^m \overline{\phi}_{g'}^{m,n} \right)$$

<div align="right">Eq. 2.48</div>

$$\ldots - \frac{\mu_w}{h_z} \left(\varphi_{T,g}^{w,m,n} - \varphi_{B,g}^{w,m,n} \right) + \frac{\varphi_g^{w,m,n-1}}{\theta v_g \Delta t_n} + \frac{1}{4\pi}\chi_{dg}\widetilde{S}_d^{m,n-1} + \Theta R_g^{m,n-1}$$

Here the residual term represents the imbalance between neutron production and loss in direction w in a spatial mesh region m. In principle, Eq. 2.48 can be solved by MOC as long as the RHS is exactly known for each flat source region. However, there are several practical difficulties in solving Eq. 2.48 as is. First of all, the total cross section is augmented by the 1-over-vΔt term. This augmentation changes the ray attenuation characteristics in the MOC solution since all the exponential terms have to be evaluated with the augmented cross section. Secondly, since the angular flux of the previous step appears on the RHS, all the angular flux should be stored at every flat source region which would cause a significant increase in the memory. In order to avoid these problems, an approximate solution approach is applied. The 1-over-vΔt term of the current time step is first moved to the RHS so that the left hand side becomes identical to the steady-state form. The angular dependence of the 1-over-vΔt term is then neglected by treating this term isotropic. This approximation would have negligible impact since the isotropy assumption is applied to the difference term not to the angular flux itself. Furthermore the angular dependence of the residual term is neglected. Eq. 2.48 now becomes:

$$\sin(\theta)\cos(\alpha)\frac{\partial \varphi_g^{w,m,n}}{\partial x} + \sin(\theta)\sin(\alpha)\frac{\partial \varphi_g^{w,m,n}}{\partial y} + \Sigma_{tg}^m \varphi_g^{w,m,n} = ...$$

$$...\frac{1}{4\pi}\left(\chi_{pg}(1-\beta^m)\psi^{m,n} + \chi_{dg}S_d^{m,n} + \sum_{g'=1}^{G} \Sigma_{s,g'\leftarrow g}^m \overline{\phi}_{g'}^{m,n} \right)$$

$$...-\frac{\mu_w}{h_z}\left(\varphi_{T,g}^{w,m,n} - \varphi_{B,g}^{w,m,n} \right) + \frac{1}{4\pi}\left(\frac{\overline{\phi}_g^{m,n-1} - \overline{\phi}_g^{m,n}}{\theta v_g \Delta t_n} + \chi_{dg}\tilde{S}_d^{m,n-1} + \Theta R_g^{m,n-1} \right)$$

Eq. 2.49

Once the delayed neutron source and the residual terms are given for each flat source region, Eq. 2.49 can be solved using the steady-state MOC solver with only a few additions of source terms. However, the residual term cannot be determined readily for each flat source region because the shape of the surface of a flat source region is irregular. Thus a further approximation is introduced to use the cell based residual term which is determined for the multi-group CMFD TFSP. The final equation becomes:

$$\sin(\theta)\cos(\alpha)\frac{\partial \varphi_g^{w,m,n}}{\partial x} + \sin(\theta)\sin(\alpha)\frac{\partial \varphi_g^{w,m,n}}{\partial y} + \Sigma_{tg}^m \varphi_g^{w,m,n} = ...$$

$$...\frac{1}{4\pi}\left(\chi_{pg}(1-\beta^m)\psi^{m,n} + \chi_{dg}S_d^{m,n} + \sum_{g'=1}^{G} \Sigma_{s,g'\leftarrow g}^m \overline{\phi}_{g'}^{m,n} \right)$$

Eq. 2.50

$$...-\frac{\mu_w}{h_z}\left(\varphi_{T,g}^{w,m,n} - \varphi_{B,g}^{w,m,n} \right) + \frac{1}{4\pi}\left(\frac{\overline{\phi}_g^{m,n-1} - \overline{\phi}_g^{m,n}}{\theta v_g \Delta t_n} + \chi_{dg}\tilde{S}_d^{m,n-1} + \Theta \overline{R}_g^{m,n-1} \right)$$

The bar above designates parameters obtained from the multi-group CMFD.

2.4.2. *Calculation flow*

The calculation flow of a DeCART transient calculation is shown in Fig. 2.6. The transient calculation is driven by the CMFD TFSP solver. At each time step, the new multi-group (MG) constants are determined using the intra-cell flux shapes and regional microscopic cross sections from the last MOC transient update.
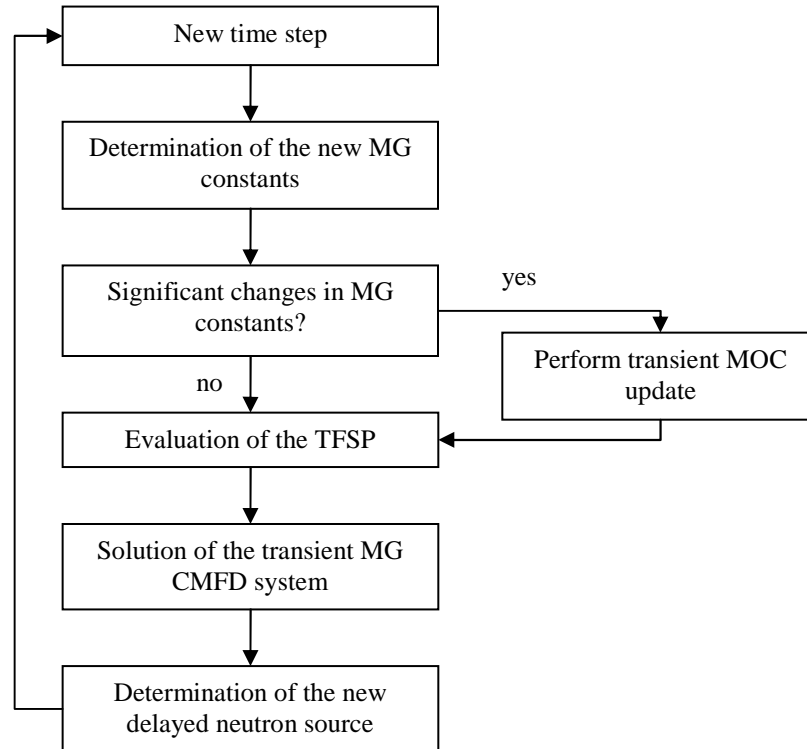
Fig. 2.6. DeCART flow chart for transient calculation

One of the user's options for the transient calculation is a threshold value in the MG cross section change. If, for a given spatial mesh, the change is bigger than the threshold value, a MOC transient calculation is performed to generate the intra-cell flux shapes and regional microscopic cross sections reflecting the new local conditions in the reactor. Otherwise the TFSP CMFD calculation continues and the next step scalar fluxes are computed by the CMFD solver. Finally, the new delayed neutron source is updated before the start a new time step.

2.4.3. *Kinetics parameters*

In the TFSP equations, i.e. in Eq. 2.46 and Eq. 2.47, three kinetics parameters appear: the total delayed neutron fraction, group-wise neutron velocity, and delayed neutron emission spectra. The delayed neutron fraction which has a strong isotopic dependence is obtained directly from the multi-group cross section library. The delayed neutron fraction of an isotope is constant and is not affected by the reactor condition such as the fuel temperature. However, for a mixture of fissionable isotopes the average delayed neutron fraction becomes condition dependent. It is obtained by isotopic fission

source weighting. Specifically, for a given spatial mesh m, the mesh averaged delayed neutron for precursor group k is obtained by:

$$\beta_k^m = \frac{\sum\limits_{i=1}^{I^m}\sum\limits_{j=1}^{J^m}\beta_k^j\left(\sum\limits_{g=1}^{G}\nu\sigma_{fg}^{m,i,j}N_j^{m,i}\overline{\phi}_g^{m,i}\right)V^{m,i}}{\sum\limits_{i=1}^{I^m}\sum\limits_{j=1}^{J^m}\left(\sum\limits_{g=1}^{G}\nu\sigma_{fg}^{m,i,j}N_j^{m,i}\overline{\phi}_g^{m,i}\right)V^{m,i}}$$

Eq. 2.51

I represents the total number of flat source region per nodal mesh m and J the number of isotopes in a given flat source region. Note also that the temperature dependence is carried by the microscopic nu-fission cross section $\sigma_{fg}^{m,i}$ of isotope j and group g at flat source region i of cell m.

The neutron velocity data are not available from the cross section library. Instead it is inferred from the microscopic group cross section of B-10 which is a nearly perfect 1-over-v absorber. The reciprocal velocity is obtained by:

$$\frac{1}{v_g} = \frac{\sigma_g}{\sigma_0}\frac{1}{v_0}$$

Eq. 2.52

where σ_0 and v_0 B-10 the absorption cross section and velocity at the room temperature, namely 3837 barns and 220,000 cm/sec, respectively.

Since the group cross section depends on the temperature of the medium, the reciprocal neutron velocity obtained by Eq. 2.52 is not uniform across the domain and each cell is assigned its own reciprocal velocity. The above formula cannot be applied to high energy groups since the energy dependence is no longer 1-over-v. For the energy groups beyond 0.1 MeV, the velocity is determined by taking the midpoint lethargy instead of the B-10 absorption cross section.

The delayed neutron emission spectrum is much softer than the prompt fission spectrum and it is dependent on the precursor group as shown (Ott and Neuhold 1985). However, the precursor group dependence is neglected in DeCART by using only one spectrum which is averaged over all the delayed neutrons.

The decay constants λ_k of the six precursor groups are fixed and they were obtained from the specification of a PWR control rod ejection benchmark problem (Finnemann and Bauer 1994). The decay constants can be overridden by the user input though.

2.4.4. *Limitations*

The final form of Eq. 2.46 and Eq. 2.47 for DeCART transient calculations has been validated by comparing the DeCART solution with the VARIANT-K transport solution for several transient benchmark problems (Cho, Kim et al. 2005). However, all calculations were performed with a fixed set of macroscopic cross sections. The transient analyses were triggered by changing the macroscopic cross sections of a given region. Typically, when a control rod was withdrawn, the cross sections of the rodded region

changed from the set corresponding to a control rod to the set corresponding to water. As it was described in the section 2.4.2, MOC TFSPs are triggered when local changes in the local composition of the reactor were detected. Practically, with provided macroscopic cross sections sets, as it was the case for the calculations reported in (Cho, Kim et al. 2005), the MOC TFSP happened when a region has its cross sections set modified by control rod movement for example. Furthermore, these calculations did not involve any kind of thermal hydraulic feedbacks.

In order to perform realistic transient calculations at the core level, without relying on a multi-step approach where a library of macroscopic cross sections is generated for the wide range of thermal hydraulic and burnup conditions encountered in a reactor during the transient, DeCART's transient methodology needs to be modified. The modifications should allow the code to handle changes in local thermal hydraulic conditions (fuel temperature, water density, etc…).

3. Improvement of the 2D/1D coupling

The goal of this part of the dissertation is to improve the 2D-1D methodology and more specifically the coupling between the MOC solver and the 1-D axial solver.

3.1. Investigation of the potential issues with the current 2D-1D coupling

In the 2D-1D methodology, the axial integration of the 3-D Boltzmann equation leads to (for convenience of the notation, the energy group index g has been omitted.):

$$\left(\sin(\theta_w)\cos(\alpha_w)\frac{\partial}{\partial x} + \sin(\theta_w)\sin(\alpha_w)\frac{\partial}{\partial y} \right)\varphi_w^Z(x,y) + \Sigma_{tg}\varphi_w^Z(x,y)$$

$$= \frac{Q(x,y)}{4\pi} - TL_w^z(x,y)$$

Eq. 3.1

where

$$\varphi_w^Z(x,y) = \frac{1}{h_z}\int_0^{h_z}\varphi_w^Z(x,y,z)dz$$

$$TL_w^z(x,y) = \frac{\mu_w}{h_z}\left(\varphi^w(x,y,z^T) - \varphi^w(x,y,z^B)\right)$$

Eq. 3.2

$$Q(x,y) = \frac{\chi}{k_{eff}}\sum_{g'=1}^{G}\nu\Sigma_{f,g'}\overline{\phi}_{g'}^Z(x,y) + \sum_{g'=1}^{G}\Sigma_{s,g'\leftarrow g}\overline{\phi}_{g'}^Z(x,y)$$

$$\overline{\phi}_{g'}^Z(x,y) = \frac{1}{h_z}\int_0^{h_z}\overline{\phi}_{g'}(x,y,z)dz$$

A close look at the Eq. 3.1 shows that a potential for a negative source term exists for 2 distinct sets of conditions:

- When the axial leakage is much larger than the neutron source term, typical for low density region where neutron streaming occurs. It is rarely encountered in LWR but can happen under accident conditions such as LOCA.
- When the axial mesh size becomes small. Numerical problem may arise when the transverse leakage term becomes large due to its $\frac{1}{h_z}$ dependence.

When the source term of the MOC equation becomes negative, the DeCART calculation usually does not recover and diverges. Although the low density conditions are not likely to be encountered during most practical transient analysis, fine axial mesh are needed to ensure an accurate scalar flux solution, especially for cases where axial heterogeneities are present. In those cases, a fine mesh is required for low order methods such as diffusion theory to properly capture the flux gradient.

In order to illustrate the limits of the current 2D-1D methodology described above, a simple problem, yet representative of PWR conditions, was developed and performed with DeCART.

3.1.1. *Test Case Description*

The test case geometry is shown in Fig. 3.1 and its cross sections are based on the C5G7 benchmark specifications (Lewis, Smith et al. 2001).

The model consists of 5 pins, and a reflective boundary condition is imposed at the boundary surfaces except for the top surface where a vacuum boundary condition is imposed. Four pins, pins 1, 2, 4 and 5, are fuel pins and pin 3 is a non-fuel pin. The fuel pin has a slab shape. The demonstrative model is similar to a slab geometry model except for the additional reflector region above which the vacuum boundary condition applies. The equivalent fuel radius was determined to preserve the fuel volume from a circular pellet. The non-fuel pin of pin number 3 is added to analyze the heterogeneity effect of a water hole or the control rod. The total height of the geometry is 56.7 cm including the 39.8 cm of fuel region and 18.9 cm of reflector region. The fuel region is initially divided in 2 meshes of 18.9 cm size and the reflector region is represented by 1 axial mesh.
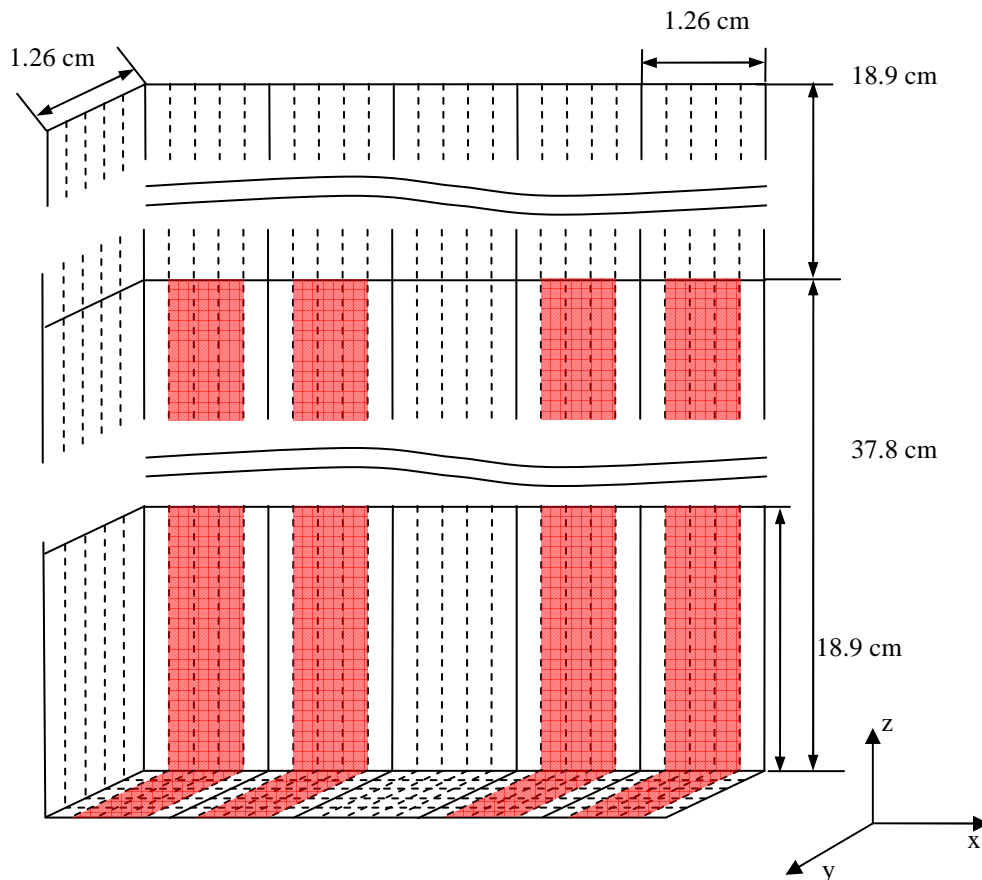
Pin 1, 2, 4 and 5: Fuel Pin
Pin 3: Fuel Pin or Guide Tube or Control Rod can be loaded

Fig. 3.1. 5-pin test problem geometry

In order to illustrate the short comings of the current 2D-1D methodology in DeCART, 2 sets of calculations are performed: One where the axial mesh is gradually reduced to less than a centimeter to assess the convergence properties of the 2D-1D algorithm in the limit of a small mesh size and a second calculation where the coolant density is reduced from 100% to 1% of its normal value to represent high leakage, low density conditions.

3.1.2. *Results and Discussion*

3.1.2.1. *Reduced Mesh Size Case*

The model described above is used with the pin 3 replaced by water hole. The axial mesh is refined by subdividing the initial spatial discretization (3 planes) evenly, see Table 3.1.

Table 3.1. Effective multiplication coefficient for various axial mesh sizes of the reduced mesh size case

Number of Planes	Axial Mesh Size [cm]	k_{eff}
3	18.90	1.25810
6	9.45	1.25960
9	6.30	1.25970
12	4.73	1.25970
15	3.78	1.25970
18	3.15	1.25980
21	2.70	1.25980
24	2.36	1.25980
27	2.10	1.25980
30	1.89	1.25980
33	1.72	1.25980
36	1.58	1.25980
39	1.45	1.25980
42	1.35	1.25980
45	1.26	1.25980

Contrary to what was expected from the previous discussion, even when the axial mesh becomes small, about the size of the radial mesh, 1.26cm, the DeCART solution does not diverge. It is also important to note the importance of refining the mesh. The predicted effective multiplication coefficient of the initial case differs by 140 pcm (per cent milli-k) compared to the case where the axial direction is refined as much as possible (1.26 cm). 140 pcm represents a non trivial difference, especially considering that the problem, a water hole surrounded by fuel rods is relatively "easy"; there is no significant axial heterogeneity.

3.1.2.2.   Low Density Case

The model described above was used with the pin 3 replaced by fuel rod. The coolant density is reduced from 100% to 1% and the axial mesh is refined by subdividing the initial spatial discretization (3 planes) evenly, see Fig. 3.1. The calculation does not converge when the axial mesh is reduced below 20cm. When the axial leakage is much larger than the neutron source term, usually for low density regions where neutron streaming occurs, the MOC source term become negative, leading to the divergence of the solution. In Fig. 3.2, the scalar flux calculated for energy group 3 is shown for the top of core near the fuel/water interface. The quantities shown in Fig 3.2. are expressed in neutrons per cm^3 but are not normalized. As indicated, the entire region corresponding to the axial water reflector has a negative flux. The reason can be understood by a closer look to the two RHS source terms of Eq. 3.1. As shown Fig. 3.2.c) and Fig. 3.2.d), since the leakage term is much larger than the usual source term, the overall MOC source term (shown in Fig. 3.2.b)) becomes negative and results in non-physical negative MOC scalar fluxes and consequently divergence of the 2D-1D algorithm.

| a) MOC Scalar Flux | b) Total MOC Source |
| c) Fission, Scattering Source | d) Leakage Source |
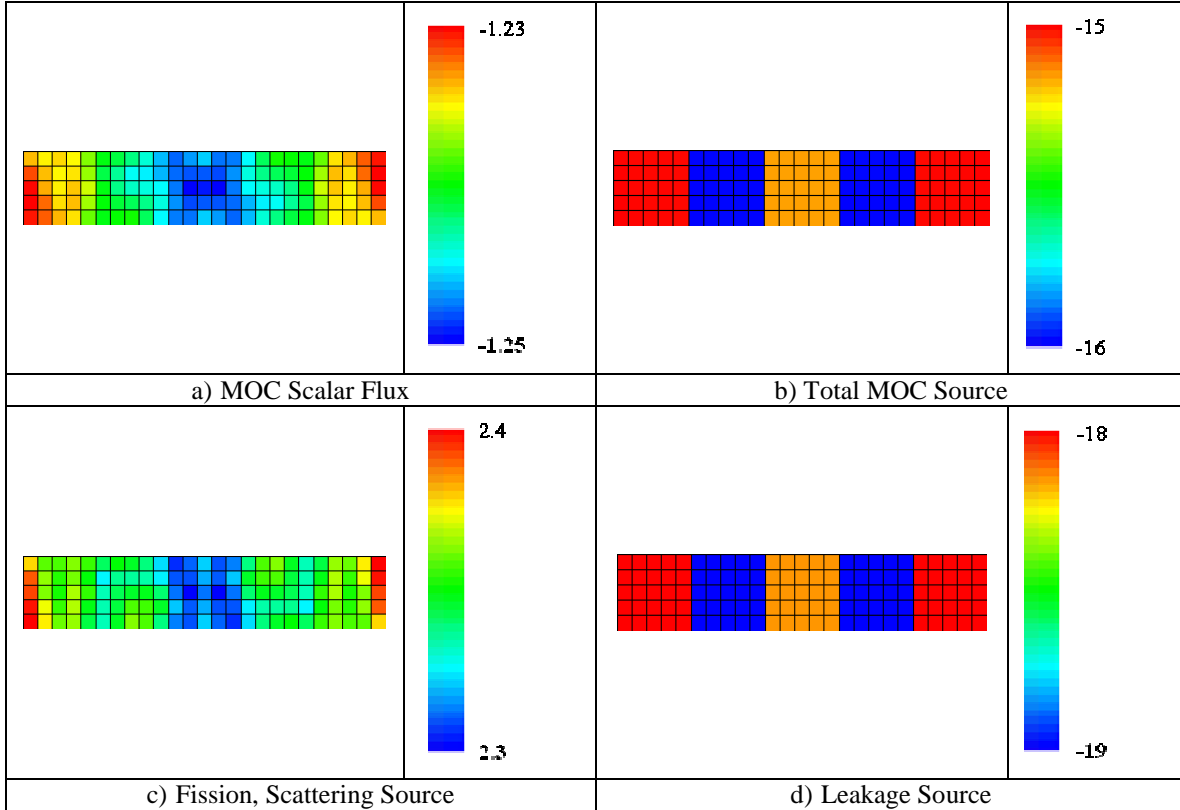
Fig. 3.2. Epithermal energy group results for the plane near the top of core

The objectives of the investigations on the 2D-1D coupling are:

- Improve the accuracy of the 2D-1D coupling while retaining the same axial solver.
- Resolve the occurrence of negative source terms in high neutron leakage regions.

Table 3.2. Effective multiplication coefficient for various axial mesh sizes of the low density case

Number of Planes	Axial Mesh Size	k_{eff}
3	18.90	0.51019
6	9.45	Divergence

The next section describes how these goals were achieved in this work.

3.2. Formulation of the new 2D/1D coupling approaches

The 2-D planar transport equation was presented above in the Eq. 3.1 and is solved together with the associated 1-D axial diffusion equation:

$$-D\frac{d^2\phi^{XY}(z)}{dz^2} + \Sigma_r\phi^{XY}(z) = Q - L^{XY}(z)$$

Eq. 3.3

where

$$\phi^{XY}(z) = \frac{1}{A}\int_{y_l}^{y_r}\int_{x_l}^{x_r}\phi(x,y,z)dxdy$$

$$TL^{XY}(z) = \frac{1}{A}\int_{-1}^{1}\sqrt{1-\mu^2}\int_{0}^{2\pi}\left(\begin{array}{c}\cos\alpha\int_{y^l}^{y^r}\left(\varphi^w(x^r,y,z)-\varphi^w(x^l,y,z)\right)dy\\ +\sin\alpha\int_{x^l}^{x^r}\left(\varphi^w(x,y^r,z)-\varphi^w(x,y^l,z)\right)dx\end{array}\right)d\alpha d\mu$$

Eq. 3.4

The main challenge of the 2D-1D methodology is to properly determine the term $TL_w^Z(x,y)$ of Eq. 3.2 using information coming from the 1-D diffusion solution. Currently, $TL_w^Z(x,y)$ is evaluated using the DP_0 approximation:

$$\frac{\mu_w}{h_z}\left(\varphi^w(x,y,z^T)-\varphi^w(x,y,z^B)\right) = \begin{cases}\frac{\mu_w}{\pi h_z}\left(j^{T,out}-j^{B,in}\right)\text{for }\mu_w > 0\\ \frac{\mu_w}{\pi h_z}\left(j^{T,in}-j^{B,out}\right)\text{for }\mu_w < 0\end{cases}$$

Eq. 3.5

where $j^{T,out}$ and $j^{T,in}$ are the partial outgoing and incoming currents at the top surface, and $j^{B,out}$ and $j^{B,in}$ are the corresponding values at the bottom surface. They are computed by solving the Eq. 3.4.

Two alternate formulations to the Eq. 3.5 are proposed in the following sections.

3.2.1. *Isotropic Leakage Coupling*

In this approximation, the axial leakage is assumed to be isotropic:

$$\overline{TL}_w^z(x,y) \approx \frac{1}{4\pi}\int_{-1}^{1}\int_{0}^{2\pi}TL_w^z(x,y)d\alpha d\mu$$

Eq. 3.6

Note: $TL_w^z(x, y)$ represents the true axial leakage and $\overline{TL}_w^z(x, y)$ its approximation, in the direction w defined by an azimuthal angle α and a polar angle μ.

Using the Eq. 3.2,

$$TL_w^z(x, y) = \frac{\mu_w}{h_z}\left(\varphi^w(x, y, z^T) - \varphi^w(x, y, z^B)\right) \qquad \text{Eq. 3.7}$$

By inserting Eq. 3.6 into the previous equation, it becomes:

$$\overline{TL}_w^z(x, y) = \frac{1}{4\pi}\int_{-1}^{1}\int_0^{2\pi}\frac{\mu_w}{h_z}\left(\varphi^w(x, y, z^T)\right)d\alpha d\mu - \frac{1}{4\pi}\int_{-1}^{1}\int_0^{2\pi}\frac{\mu_w}{h_z}\left(\varphi^w(x, y, z^B)\right)d\alpha d\mu \qquad \text{Eq. 3.8}$$

By definition of the net neutron current,

$$\overset{\rho}{J}(x, y, z) = \int_{-1}^{1}\int_0^{2\pi}\overset{\rho}{w}(\alpha, \mu)\left(\varphi^w(x, y, z)\right)d\alpha d\mu \qquad \text{Eq. 3.9}$$

Projecting along the z direction leads to the needed quantity:

$$J^{XY}(z) = \overset{\rho}{J}(x, y, z).\overset{\rho}{u}_z = \int_{-1}^{1}\int_0^{2\pi}\mu_w\left(\varphi^w(x, y, z)\right)d\alpha d\mu \qquad \text{Eq. 3.10}$$

Finally:

$$\overline{TL}_w^z(x, y) = \frac{1}{4\pi h_z}\left(J^{XY}(z^T) - J^{XY}(z^B)\right) \qquad \text{Eq. 3.11}$$

3.2.2. P_1 coupling

In this approximation, the angular flux on top and bottom of the considered spatial mesh is assumed to have a linear dependence in angle:

$$\overline{\varphi}^w(x, y, z) \approx \frac{1}{2}\phi(x, y, z) + \frac{3}{2}\overset{\rho}{w}(\alpha, \mu).\overset{\rho}{J}(x, y, z) \qquad \text{Eq. 3.12}$$

Integrating $\overline{\varphi}^w(x, y, z)$ over the top and bottom faces of a considered axial mesh, it becomes:

$$TL_w^z(x, y) \approx \overline{TL}_w^z(x, y) = \frac{\mu_w}{h_z}\left(\begin{array}{c}\frac{1}{2}\phi(x, y, z^T) - \phi(x, y, z^B) \\ +\frac{3}{2}\overset{\rho}{w}(\alpha, \mu).\left(\overset{\rho}{J}(x, y, z^T) - \overset{\rho}{J}(x, y, z^B)\right)\end{array}\right) \qquad \text{Eq. 3.13}$$

By projecting the net current J along the direction z, and integrating over x and y, it comes:

$$\overline{TL}_w^z(x, y) = \frac{\mu_w}{2h_z}\left(\phi^{XY}(z^T) - \phi^{XY}(z^B) + 3\mu_m.\left(J^{XY}(z^T) - J^{XY}(z^B)\right)\right) \qquad \text{Eq. 3.14}$$

Both formulations of Eq. 3.11 and Eq. 3.14 were implemented into DeCART as new user's options for the 2D-1D transverse leakage coupling to replace the original formulation of Eq. 3.5. Because of its consistency with the diffusion theory (both are based on a P_1 approximation of the angular flux) the formulation of Eq. 3.14 is expected to give the best results in terms of accuracy. The isotropic leakage formulation of Eq. 3.11 represents a step down in terms of accuracy compared to the DP_0 approximation because it assumes a completely isotropic leakage instead of a half-space isotropic leakage in the DP_0 approximation. However, since the Eq. 3.11 produces the same axial transverse leakage for symmetric polar angles with respect to the *(x,y)* plane, it is possible to solve the MOC formulation only for half the polar angles, reducing the computational cost of the calculation.

If the formulation of Eq. 3.14 is expected to improve the accuracy of the 2D-1D methodology, and the formulation of Eq. 3.11 is expected to reduce its cost, neither of them does solve the potential occurrence of negative MOC source term as discussed in section 3.1. The next section details a potential fix to the problem by proposing a splitting of the transverse leakage term between the Left Hand Side (LHS) and RHS of Eq. 3.1.

3.3. Transverse Leakage Splitting Formulation

The principal idea of the transverse leakage splitting formulation is to separate the quantity $TL_w^z(x,y)$ between the LHS and RHS of Eq. 3.1. By moving part of $TL_w^z(x,y)$ on the LHS, Eq. 3.1 can be reformulated as:

$$\sqrt{1-\mu_m}\left(\cos(\alpha_w)\frac{\partial}{\partial x}+\sin(\alpha_w)\frac{\partial}{\partial y}\right)\varphi_w^Z(x,y)+\left(\Sigma_{tg}+\Sigma_{Lg}\right)\varphi_w^Z(x,y)$$
$$=\frac{Q(x,y)}{4\pi}-TL_w^z(x,y)+\Sigma_{Lg}\tilde{\varphi}_w^Z(x,y)$$

Eq. 3.15

Where Σ_{Lg} is an angle independent "leakage" cross sections, and $\tilde{\varphi}_w^Z(x,y)$ some approximation of the angular flux. To simplify the notations, the leakage term in the LHS of Eq. 3.16 is referred as L_w^{XY}. The goal is to avoid cases where $TL_w^z(x,y)$ is bigger than $\frac{Q(x,y)}{4\pi}$ causing negative MOC sources, or cases where the modified removal term, $\left(\Sigma_{tg}+\Sigma_{Lg}\right)$, becomes itself negative.

Before going any further, the reason why Σ_{Lg} must be angle independent needs to be clarified. As described in Chapter II, the macroscopic cross sections in DeCART are evaluated during the calculation given a local flux shape and thermal hydraulic conditions. They are computed before the inner most loop of the MOC algorithm, i.e. before the sweeping through every segment of every region for each angle. Having angle dependent macroscopic cross sections would require their evaluation during the MOC inner most loop which would undesirably increase the cost of the calculation.

The next sections describe how to properly choose Σ_{Lg} and $\tilde{\varphi}_w^Z(x,y)$. Three different splitting are considered. A partial current splitting using a formulation of

$TL_w^z(x, y)$ based on Eq. 3.11 is discussed first. Then a splitting also related to the isotropic formulation of $TL_w^z(x, y)$, see Eq. 3.11, is presented. Finally a splitting based on the formulation of Eq. 3.14, for $TL_w^z(x, y)$ is the last to be considered.

3.3.1. *Partial Current Splitting*

For this approach, the starting point is the isotropic leakage formulation for $TL_w^z(x, y)$, Eq. 3.11. Expressing the net current $J^{XY}(z)$ as function of its associated partial currents leads to:

$$J^{XY}(z^T) = j^{T,out} - j^{T,in} \qquad \text{Eq. 3.16}$$

$j^{T,out}$ and $j^{T,in}$ are the partial outgoing and incoming currents at the top surface.

By inserting Eq. 3.16 into Eq. 3.11, it becomes:

$$\overline{TL}_w^z(x, y) = \frac{1}{4\pi h_z}\left(j^{T,out} - j^{T,in} + j^{B,out} - j^{B,in}\right) \qquad \text{Eq. 3.17}$$

Then Σ_{Lg} and $\tilde{\varphi}_w^Z(x, y)$ can be defined as follow:

$$\Sigma_{Lg} = \frac{1}{\phi^Z(x, y)h_z}\left(j^{T,out} + j^{B,out}\right)$$

$$\tilde{\varphi}_w^Z(x, y) = \frac{\phi^Z(x, y)}{4\pi} \qquad \text{Eq. 3.18}$$

With the choices of Eq. 3.18, the RHS of Eq. 3.16 becomes:

$$\frac{Q(x, y)}{4\pi} - TL_w^z(x, y) + \Sigma_{Lg}\tilde{\varphi}_w^Z(x, y) = \frac{Q(x, y)}{4\pi} + \frac{1}{4\pi h_z}\left(j^{T,in} + j^{B,in}\right) \qquad \text{Eq. 3.19}$$

This quantity will always be positive, being the sum of positive quantities.

The LHS of Eq. 3.16 is also modified:

$$L_w^{XY} + \left(\Sigma_{tg} + \Sigma_{Lg}\right)\varphi_w^Z(x, y)$$

$$= L_w^{XY} + \left(\Sigma_{tg} + \frac{1}{\phi^Z(x, y)h_z}\left(j^{T,out} + j^{B,out}\right)\right)\varphi_w^Z(x, y) \qquad \text{Eq. 3.20}$$

This approach has been implemented in the ANL version of DeCART to analyze gas cooled reactors. It is reported in (Pointer, Lee et al. 2009) to have good convergence properties.

3.3.2. *Isotropic Leakage Splitting*

Similarly to section 3.3.1, the starting point for the isotropic leakage splitting is Eq. 3.11. Σ_{Lg} and $\tilde{\varphi}_w^Z(x, y)$ are chosen as follow:

$$\Sigma_{Lg} = \max\left(\frac{1}{\phi^Z(x,y)h_z}\left(J^{XY}(z^T) - J^{XY}(z^B)\right),0\right)$$

$$\tilde{\varphi}_w^Z(x,y) = \frac{\phi^Z(x,y)}{4\pi}$$

Eq. 3.21

The logic behind the choice of Σ_{Lg} is that if the quantity $\frac{1}{\phi^Z(x,y)h_z}\left(J^{XY}(z^T) - J^{XY}(z^B)\right)$ is positive, the axial leakage contribution is negative potentially causing the MOC source term to become itself negative. By transferring it to the LHS, the added removal term is positive ensuring that both removal and source terms are positive.

3.3.3. *P₁ Splitting*

For this approach, the starting point is the P_1 transverse leakage formulation for $TL_w^z(x,y)$, Eq. 3.14. It is possible to define an angle dependent leakage cross section, Σ_{Lg}^w:

$$\Sigma_{Lg}^w = \frac{\mu_w}{2h_z\overline{\varphi}_w^Z(x,y,\mu_w)}\left(\phi^{XY}(z^T) - \phi^{XY}(z^B) + 3\mu_m\left(J^{XY}(z^T) - J^{XY}(z^B)\right)\right)$$

$$\overline{\varphi}_w^Z(x,y,\mu_w) = \int_0^{2\pi}\varphi_w^Z(x,y,\mu_w,\alpha_w)d\alpha$$

Eq. 3.22

Consequently, the choice of $\tilde{\varphi}_w^Z(x,y)$ is:

$$\Sigma_{Lg}^w = \frac{\mu_w}{2h_z\overline{\varphi}_w^Z(x,y,\mu_w)}\left(\phi^{XY}(z^T) - \phi^{XY}(z^B) + 3\mu_m\left(J^{XY}(z^T) - J^{XY}(z^B)\right)\right)$$

$$\tilde{\varphi}_w^Z(x,y) = \frac{1}{2\pi}\overline{\varphi}_w^Z(x,y,\mu_w)$$

Eq. 3.23

One of the issues of the P_1 splitting is the determination of $\overline{\varphi}_w^Z(x,y,\mu_w)$, which is the azimuthally integrated, polar dependent angular flux. It is easily determined during the 2-D MOC calculation but requires additional memory storage, hence a higher computational cost.

The other issue is the angular dependence of Σ_{Lg}^w. As stated at the beginning of this section, having a angular dependent cross section would require the evaluation of the removal term in the inner most loop of the MOC sweep which is not desirable in terms of computational cost. Similar to what was shown in 3.3.2, an angular independent splitting is chosen:

$$\Sigma_{Lg}^w = \max_w\left(2\pi\frac{TL_w^z(x,y) - Q(x,y)/4\pi}{h_z\overline{\varphi}_w^Z(x,y,\mu_w)},0\right)$$

Eq. 3.24

So the angular direction, w_m, for which the MOC source term, including axial transverse leakage, is the most negative, is selected and the leakage cross section is defined as:

$$\Sigma_{Lg} = 2\pi \frac{TL_{w_m}^z(x,y) - Q(x,y)\Big/4\pi}{h_z \overline{\varphi}_{w_m}^Z(x,y,\mu_{w_m})} \qquad \text{Eq. 3.25}$$

where $TL_{w_m}^z(x,y)$ is defined as follow:

$$TL_{w_m}^z(x,y) = \max_w \left(TL_w^z(x,y),0\right) \qquad \text{Eq. 3.26}$$

Σ_{Lg} is now angular independent and it is applied to all angular directions w, even though it was determined from the direction, w_m. For the direction w_m, the complete axial transverse leakage is moved to the LHS. The other directions corresponding to other polar direction, the source term is given by:

$$\frac{Q(x,y)}{4\pi} - TL_w^z(x,y) = TL_{w_m}^z(x,y) - TL_w^z(x,y) \qquad \text{Eq. 3.27}$$

Since the direction has been chosen for its maximum axial transverse leakage, the quantity $TL_{w_m}^z(x,y) - TL_{w_m}^z(x,y)$ is positive. The potential for negative source is eliminated.

3.3.1. _Approximation involved in transverse leakage splitting_

Because of $\phi^Z(x,y) = \int_{4\pi} \varphi_w^Z(x,y)dw$ in the partial current splitting, and

$\widetilde{\varphi}_w^Z(x,y) = \int_{2\pi} \overline{\varphi}_w^Z(x,y,\mu_w)d\alpha_w$ for the P$_1$ transverse leakage splitting, the overall neutron balance of the considered spatial mesh is preserved. However, depending on which side of the equation the transverse leakage is applied, the approximation made to the 3-D transport equation is different. When the additional leakage cross section Σ_{Lg} is added to the LHS, its angular dependence is proportional to the angular dependence of $\varphi_w^Z(x,y)$. Added on the RHS, the contribution to the source term is isotropic. The approximation introduced by transverse leakage splitting is shown in Eq. 3.28:

$$TL_w^z(x,y) = L_1 \varphi_w^Z(x,y) + L_2 + \varepsilon \qquad \text{Eq. 3.28}$$

where $L_1 \varphi_w^Z(x,y)$ is the contribution to the LHS, L$_2$ the contribution to the RHS and ε the error term. The transverse leakage term has the same order of magnitude than a net current gradient.

For the partial current splitting,

$$TL_w^z(x, y) = \frac{1}{\phi^Z(x, y)h_z}\left(j^{T,out} + j^{B,out}\right)\!\varphi_w^Z(x, y) + \frac{1}{4\pi h_z}\left(j^{T,in} + j^{B,in}\right) + \varepsilon$$ Eq. 3.29

The transverse leakage term has the order of magnitude of the sum of partial currents divided by the mesh size, which in the P_1 approximation have the order of magnitude of a scalar flux. In the limit of a fine mesh, the sum of partial currents goes to a finite quantity while the denominator goes to zero. This formulation will produce poor results in the limit of small mesh size.

For the P_1 transverse leakage splitting and isotropic transverse leakage, L1 and L2 are chosen to have the same order of magnitude than the initial transverse leakage, limiting the amount of error introduced by the transverse leakage approximation.

3.4. Results

3.4.1. Foreword about CMFD and convergence

The convergence analysis of the CMFD method has shown (Cho, Lee et al. 2003; Lee, Downar et al. 2004; Lee, Lee et al. 2004) that under certain conditions, especially for small mesh size, the CMFD is not stable. Since the primary purpose of the work summarized here is to improve the 2D-1D algorithm itself, the CMFD acceleration has been turned off. Any occurrence of divergence is then solely due to the breakdown of the 2D-1D methodology.

During the course of a given calculation, the DeCART convergence can break down in two different manners. The first one is a divergence, where the residual increases exponentially and eventually causes the calculation to fail. This failure mode is recorded as "D.V." for divergence in the result's table. The second one is a non convergence, where the residual stops decreasing and k_{eff} oscillates between two values until the maximum number of outer iterations is reached. This failure mode is recorded as "N.C." for non convergence in the result's table.

3.4.2. Mesh refinement problems

The 2 new coupling approaches and their associated three splitting are applied to the problem described in section 3.1.1 to evaluate their effect on the convergence and accuracy of the DeCART solution. Pin 3 is replaced first by a water hole, then by a partially inserted control rod. Finally, the convergence issue described in section 3.1.2.2 is investigated by looking at a problem where the water density in the water hole is reduced from 100% to 1%.

For each of the 3 problems, 6 DeCART calculations are recorded; each of them represents the original 2D-1D DeCART coupling and the new approaches described above. Each option is described in the Table 3.3 below.

3.4.2.1. Water Hole case

For this case, the pin 3 of the problem described in section 3.1.1 is made of a water hole. For each of the 6 coupling options, the axial mesh is refined by subdividing

equally the initial geometry. Initially, there are 3 planes of 21.42cm thickness each. Each plane is subdivided in 2 equal size subdivisions to form the next problem.

A reference solution is obtained by running DeCART on the equivalent 2D model using only the MOC solver. The transport solution obtained is used as a reference to compare with each of the 2D-1D calculations.

Table 3.3. 2D-1D coupling options summary

Option Index	Description
0	Partial current splitting (section3.3.1)
1a	Isotropic Leakage, splitting (section 3.2.1 and 3.3.2)
1b	Isotropic Leakage, no splitting (section 3.2.1)
2	DP0 coupling, no splitting (original DeCART)
3a	P1 coupling, splitting (section 3.2.2 and 3.3.3)
3b	P1 coupling, no splitting (section 3.2.2)

For each DeCART run, the effective multiplication coefficient k_{eff} is recorded. The results for the water hole case are summarized in Table 3.4 and Fig. 3.3. In the Fig. 3.3, all the curves besides option 0 are located on top of each other. Instead of showing the actual effective multiplication coefficients, Table 3.4 presents the difference with the reference k_{eff} expressed in terms of pcm. The definitions of pcm and relative pinpower difference are given in the equations Eq. 3.30 and Eq. 3.31 below:

$$pcm = \left(\frac{k_{eff}^{2D-1D}}{k_{eff}^{2D}} - 1 \right) 10^5$$

Eq. 3.30

$$\Delta P = \left(\frac{P^{2D-1D}}{P^{2D}} - 1 \right) 10^2$$

Eq. 3.31

The effective multiplication coefficients represent a measure of the global differences between calculations. In order to have a better understanding of the local differences, the averaged power generated by fuel rod per initial axial mesh is also recorded and compared between calculations. In the DeCART model, there are 2 axial slice, see section 3.1.1. Their local power comparison is summarized in Table 3.5 and Table 3.6.

The original coupling of DeCART, option 2, converges monotonically toward its asymptotic solution when the axial mesh is refined. Since the CMFD has been turned off, the convergence issues observed in the literature for small mesh size do not appear.

Similarly, the potential convergence problem, related to a negative MOC source in the case of strong axial leakage, is not observed in the Water Hole case. As far as accuracy is concerned, the spatial convergence is smooth towards a k_{eff} equal to 1.2614. The difference of about 130 pcm with respect to the reference solution is rather small but expected because the reference solution is obtained by a pure transport solution, whereas the 2D-1D method is based on a mix of diffusion and transport theories. The relatively good agreement was expected given the weak axial heterogeneities of the Water Hole problem. The pinpower predictions, shown in Table 3.5 and Table 3.6 show that besides the case of partial current splitting, all methods converge to the same pinpower distribution.

Table 3.4. Convergence behavior of k_{eff} for the water hole geometry

DeCART 2D Reference k_{eff}	1.2614					

Pcm Difference with respect to 2D k_{eff}

Number of Planes	Axial Mesh Size [cm]	0	1a	1b	2	3a	3b
3	18.90	-248	-260	-262	-261	-259	-259
6	9.45	-121	-143	-143	-143	-142	-142
9	6.30	-104	-134	-134	-134	-132	-132
12	4.73	-94	-132	-133	-132	-131	-131
15	3.78	-87	-131	-131	-131	-130	-130
18	3.15	-81	-130	-130	-130	-129	-129
21	2.70	-51	-129	-130	-129	-128	-128
24	2.36	112	-127	-128	-127	-126	-126
27	2.10	-800	-128	-129	-128	-128	-128
30	1.89	-859	-128	-128	-128	-128	-128
33	1.72	N.C	-128	-129	-128	-128	-128
36	1.58	N.C	-128	-128	-128	-127	-127
39	1.45	N.C	-127	-128	-127	-126	-126
42	1.35	N.C	-128	-128	-128	-127	-127
45	1.26	N.C	-128	-128	-128	-126	-126
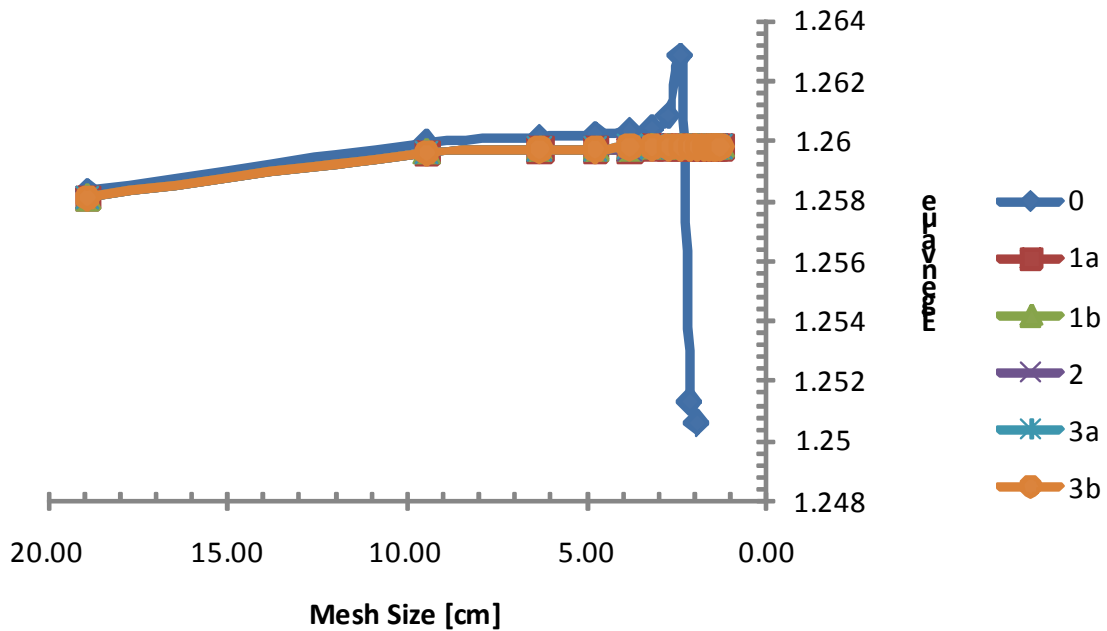
Fig. 3.3. Convergence Behavior of k_{eff} for water hole geometry

The difference with the reference solution is less that 0.4% for the finest spatial mesh for the lower fuel region, where the error is about 0.7% for the upper mesh. The agreement is better in the lower part of the problem because the leakage plays a lesser role, making the diffusion solution in the axial direction less of a liability. In the vicinity of the axial water reflector, i.e. in the upper fuel region, the neutron leakage plays a more important role, and causes the 2D-1D methodology to predict less accurate results.

Except for the partial current coupling, the other coupling methods all have similar convergence and accuracy properties. They all converge to eigenvalue around 1.2614 in a conventional manner: when the spatial mesh is refined, the solution converges to a constant k_{eff}. The small discrepancies in terms of eigenvalue observed from isotropic leakage to DP_0 to P_1 come from the different approximations applied to the transverse leakage term as described in the section 3.2 and 3.3.

Table 3.5. Relative pinpower difference with the 2D DeCART reference for the lower fuel region for the Water Hole case

		% Relative pinpower difference for lower fuel region					
Number of Planes	Axial Mesh Size [cm]	0	1a	1b	2	3a	3b
3	18.90	0.81	0.98	0.98	0.98	0.90	0.90
6	9.45	0.29	0.55	0.55	0.55	0.51	0.51
9	6.30	0.09	0.43	0.43	0.43	0.40	0.40
12	4.73	0.06	0.42	0.42	0.42	0.42	0.42
15	3.78	0.18	0.39	0.41	0.39	0.39	0.39
18	3.15	0.29	0.40	0.40	0.40	0.38	0.38
21	2.70	0.36	0.38	0.38	0.38	0.36	0.36
24	2.36	0.47	0.40	0.40	0.40	0.36	0.36
27	2.10	0.51	0.39	0.39	0.39	0.39	0.39
30	1.89	0.38	0.37	0.38	0.37	0.37	0.37
33	1.72	N.C	0.38	0.38	0.37	0.35	0.35
36	1.58	N.C	0.37	0.37	0.37	0.35	0.35
39	1.45	N.C	0.36	0.38	0.36	0.35	0.35
42	1.35	N.C	0.36	0.37	0.36	0.35	0.35
45	1.26	N.C	0.37	0.38	0.37	0.35	0.35

For this first test problem, there were no benefits of using the transverse leakage splitting techniques recently implemented in DeCART since no convergence issues are observed even for very small mesh size of 1.26 cm. This finding was expected since the Water Hole case is not driven by neutron leakage. However, it allows us to confirm that the 2D-1D methodology has no convergence issues for regular PWR problems even if the axial mesh is refined to about the size of the radial mesh.

For the Water Hole problem, the benefits of the recently implemented treatment of the transverse leakage at the planar interface, namely the isotropic leakage and P_1 coupling, are not visible. For relatively homogeneous problem, all the available coupling

return the same answer, both in terms of global and local information, i.e. effective multiplication coefficients and fuel rod power. The main benefit of using the isotropic leakage coupling instead of the P_1 coupling is the same level of accuracy in term of k_{eff} is reached while considering half of the polar directions, reducing the computing cost of the calculation.

The worst 2D-1D coupling option, both in terms of convergence and accuracy is the partial current splitting option, since no converged solution is obtained for an axial mesh of less than 1.8 cm. For the converged solutions, the accuracy is questionable since no spatial convergence seems to be observed: k_{eff} keeps increasing without reaching a plateau as it is observed for the other methods. This behavior can be explained by the limitations already formulated in section 3.3.1 about the partial current splitting. The better convergence properties and the accuracy issues both come from an artificially increased removal and source terms in Eq. 3.15. The partial currents are always a much bigger quantity than the net currents, which makes the transferring of partial currents from one side to the other, not a physically correct approach as already discussed in 3.3.1.

Table 3.6. Relative pinpower difference with the 2D DeCART reference for the upper fuel region for the Water Hole case

Number of Planes	Axial Mesh Size [cm]	0	1a	1b	2	3a	3b
% Relative pinpower difference for lower fuel region							
3	18.90	0.81	0.98	0.98	0.98	0.90	0.90
6	9.45	0.29	0.55	0.55	0.55	0.51	0.51
9	6.30	0.09	0.43	0.43	0.43	0.40	0.40
12	4.73	0.06	0.42	0.42	0.42	0.42	0.42
15	3.78	0.18	0.39	0.41	0.39	0.39	0.39
18	3.15	0.29	0.40	0.40	0.40	0.38	0.38
21	2.70	0.36	0.38	0.38	0.38	0.36	0.36
24	2.36	0.47	0.40	0.40	0.40	0.36	0.36
27	2.10	0.51	0.39	0.39	0.39	0.39	0.39
30	1.89	0.38	0.37	0.38	0.37	0.37	0.37
33	1.72	N.C	0.38	0.38	0.37	0.35	0.35
36	1.58	N.C	0.37	0.37	0.37	0.35	0.35
39	1.45	N.C	0.36	0.38	0.36	0.35	0.35
42	1.35	N.C	0.36	0.37	0.36	0.35	0.35
45	1.26	N.C	0.37	0.38	0.37	0.35	0.35

3.4.2.2. *Control Rod case*

For this case, the pin 3 of the problem described in section 3.1.1 is made of a partially inserted control rod. The control rod is inserted from the top surface to 18.9 cm from the bottom of the problem geometry. The types of calculation performed are the

same as in section 3.4.2.1 above. The results for the water hole case are summarized in Fig. 3.4 and Table 3.7, Table 3.8 and Table 3.9.

The original coupling of DeCART, option 2, converges monotonically toward its asymptotic solution when the axial mesh is refined. Since the CMFD has been turned off, the convergence issues observed in the literature for small mesh size do not appear either for the Control Rod case. As far as accuracy is concerned, the spatial convergence is smooth towards a k_{eff} equals to 1.168277.

The conclusions for the control rod case are similar to the water hole case in that potential convergence problems related to negative MOC source in case of strong axial leakage are not observed. As far as accuracy is concerned, the spatial convergence is smooth toward a k_{eff} equals to 1.168277. The difference of about 250 pcm with respect to the reference solution is larger than that observed in the Water Hole case. It was expected since the Control Rod case presents more axial heterogeneities. The departure from a purely diffusive media is more important in the Control Rod case. The pinpower predictions, shown in Table 3.8 and Table 3.9 show that besides the case of partial current splitting, all methods converge to the same pinpower distribution. The difference with the reference solution is less that 0.01% for the finest spatial mesh for the lower fuel region, where the error is about 0.03% for the upper mesh. The agreement is surprisingly good and much better than in the Water Hole case, which is likely attributable to some cancellation of errors.

Table 3.7. Convergence behavior of k_{eff} for the control rod geometry

DeCART 2D Reference k_{eff}		1.168277					
Pcm Difference with respect to 2D k_{eff}							
Number of Planes	Axial Mesh Size [cm]	0	1a	1b	2	3a	3b
3	18.90	1619	D.V.	1573	1571	1568	1568
6	9.45	223	176	174	170	166	166
9	6.30	-23	-85	-87	-90	-95	-95
12	4.73	-82	-170	-171	-175	-179	-179
15	3.78	-237	-203	-205	-207	-211	-211
18	3.15	277	-221	-223	-225	-229	-229
21	2.70	-227	-231	-233	-235	-240	-240
24	2.36	451	-234	-235	-238	-241	-241
27	2.10	-708	-241	-242	-245	-248	-248
30	1.89	N.C.	-243	-244	-247	-251	-251
33	1.72	1219	-246	-247	-250	-253	-253
36	1.58	N.C.	-246	-247	-249	-253	-253
39	1.45	N.C.	-244	-246	-248	-251	-251
42	1.35	N.C.	-247	-248	-250	-253	-253
45	1.26	N.C.	-247	-248	-251	-253	-253
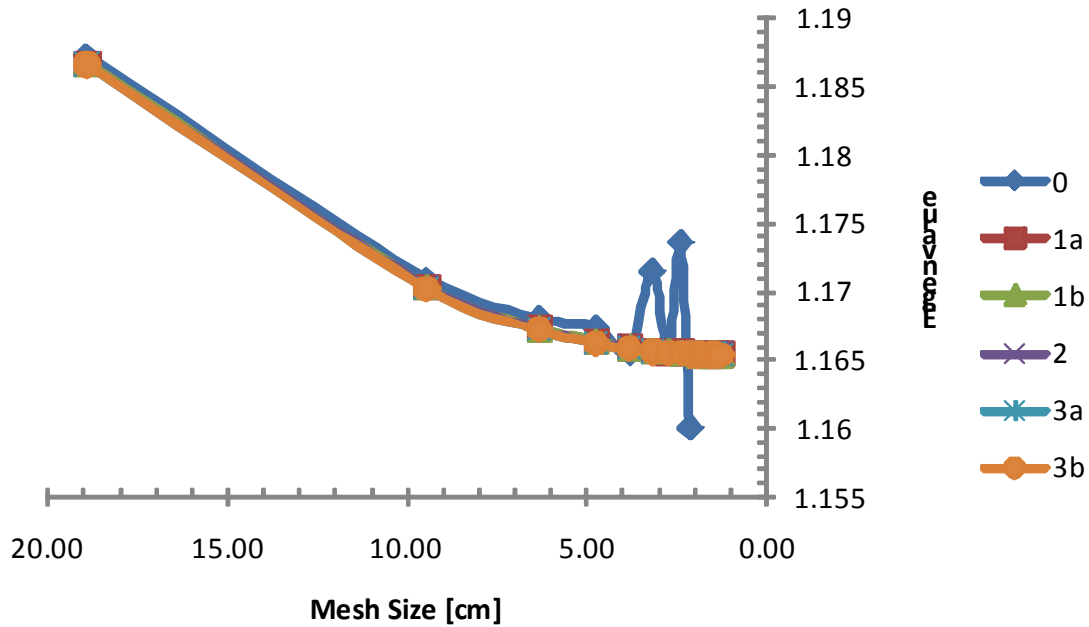
Fig. 3.4. Convergence Behavior of k_{eff} for control rod geometry

Table 3.8. Relative pinpower difference with the 2D DeCART reference for the lower fuel region for the Control Rod case

% Relative pinpower difference for lower fuel region							
Number of Planes	Axial Mesh Size [cm]	0	1a	1b	2	3a	3b
3	18.90	0.65	D.V.	0.89	0.95	0.95	0.95
6	9.45	0.11	0.44	0.47	0.47	0.47	0.47
9	6.30	0.25	0.19	0.21	0.21	0.23	0.23
12	4.73	0.47	0.11	0.11	0.11	0.11	0.11
15	3.78	0.63	0.05	0.06	0.08	0.08	0.08
18	3.15	0.74	0.03	0.03	0.03	0.06	0.06
21	2.70	0.85	0.02	0.03	0.03	0.03	0.03
24	2.36	0.93	0.01	0.01	0.02	0.02	0.02
27	2.10	1.07	0.01	0.01	0.01	0.02	0.02
30	1.89	N.C	0.02	0.03	0.03	0.03	0.03
33	1.72	1.26	0.01	0.01	0.01	0.02	0.02
36	1.58	N.C	0.01	0.02	0.02	0.02	0.02
39	1.45	N.C	0.01	0.02	0.02	0.02	0.02
42	1.35	N.C	0.01	0.01	0.02	0.02	0.02
45	1.26	N.C	0.01	0.01	0.01	0.01	0.01

The pinpower comparison tends to show the same trend as already observed in the Water Hole case, the agreement with the reference pinpower prediction is better in the

42

lower part of the problem because the leakage plays a lesser role, making the diffusion solution in the axial direction less of a liability. In the vicinity of the axial water reflector, i.e. in the upper fuel region, the neutron leakage plays a more important role, and causes the 2D-1D methodology to predict less accurate results. Another important item highlighted by the Control Rod case, is the need for refined spatial meshing in the region of large flux gradients. The errors in terms of pinpower prediction for the coarser mesh are around 1% in the lower part of the fuel, but in the area of the control rod tip, i.e. in the upper part of the fuel, the error is about 9%. It is quickly reduced as the spatial mesh is refined.

Table 3.9. Relative pinpower difference with the 2D DeCART reference for the upper fuel region for the Control Rod case

% Relative pinpower difference for upper fuel region							
Number of Planes	Axial Mesh Size [cm]	0	1a	1b	2	3a	3b
3	18.90	6.76	D.V.	8.68	8.68	9.16	9.16
6	9.45	2.44	4.12	4.12	4.12	4.36	4.36
9	6.30	0.29	1.79	1.79	1.95	1.79	1.79
12	4.73	1.53	0.99	0.99	0.99	0.99	0.99
15	3.78	2.37	0.42	0.42	0.51	0.61	0.61
18	3.15	2.69	0.27	0.27	0.19	0.27	0.27
21	2.70	3.33	0.24	0.24	0.24	0.10	0.10
24	2.36	3.39	0.09	0.15	0.15	0.09	0.09
27	2.10	4.19	0.03	0.03	0.09	0.03	0.03
30	1.89	N.C	0.02	0.02	0.03	0.08	0.08
33	1.72	5.25	0.03	0.03	0.01	0.03	0.03
36	1.58	N.C	0.07	0.01	0.05	0.05	0.05
39	1.45	N.C	0.03	0.03	0.00	0.03	0.03
42	1.35	N.C	0.03	0.03	0.03	0.00	0.00
45	1.26	N.C	0.03	0.03	0.03	0.06	0.06

The other conclusions from the Water Hole case are also evident in the results of the control rod case, i.e. the convergence and accuracy of partial current coupling, benefits of transverse leakage splitting, and more accurate formulation of transverse leakage.

3.4.3.   *Low density case.*

For this problem, the pin 3 of the geometry described in section 3.1.1 is replaced by a fuel rod, and the water density, both in the coolant and in the axial reflector is reduced from 100% to 1% to simulate a high neutron leakage environment. The types of calculation performed are the same as in section 3.4.2.1 above. The results for the water hole case are summarized in Fig. 3.5, Table 3.10, Table 3.11and Table 3.12.

The original coupling of DeCART, option 2, diverges as soon as the axial mesh is refined, as already stated in section 3.1.2.2 due to a strong axial leakage that causes the MOC source to become negative. Both newly implemented transverse leakage coupling, based on either isotropic leakage or P_1 approximations, diverge for the same reason as the original DeCART coupling. The partial current splitting as well as the transverse leakage splitting associated with the isotropic leakage coupling, option 1a, produces results for a spatial mesh equivalent to the radial mesh size. However, the limitations observed in the previous test cases with respect to the accuracy of the partial current splitting, are also observed in the Low Density case. Option 1a performs well, with a smooth spatial convergence toward a k_{eff} equals to 0.47431. Surprisingly, option 3a does not converge as well as expected. When the local polar wise angular flux becomes small, the division by $\overline{\varphi}_{w_m}^Z\left(x, y, \mu_{w_m}\right)$ in Eq. 3.24 tends to create very large value for Σ_{Lg}^w, which increases the local removal term and further reduce the local angular flux eventually causing the calculation to crash.

Table 3.10. Convergence behavior of k_{eff} for the low density problem

DeCART 2D Reference k_{eff}	0.47515					
Pcm Difference with respect to 2D k_{eff}						
Number of Planes	Axial Mesh Size [cm]	0	1a	1b	2	3a	3b
3	18.90	-276	-229	-156	-158	D.V.	-147
6	9.45	-135	-147	D.V	D.V	D.V	135
9	6.30	-114	-175	D.V	D.V	D.V	D.V
12	4.73	-120	-189	D.V	D.V	D.V	D.V
15	3.78	-105	-183	D.V	D.V	D.V	D.V
18	3.15	36	-181	D.V	D.V	D.V	D.V
21	2.70	276	-177	D.V	D.V	D.V	D.V
24	2.36	-126	-170	D.V	D.V	D.V	D.V
27	2.10	-152	-175	D.V	D.V	D.V	D.V
30	1.89	23	-177	D.V	D.V	D.V	D.V
33	1.72	17	-183	D.V	D.V	D.V	D.V
36	1.58	-6	-177	D.V	D.V	D.V	D.V
39	1.45	-97	-168	D.V	D.V	D.V	D.V
42	1.35	-78	-175	D.V	D.V	D.V	D.V
45	1.26	40	-177	D.V	D.V	D.V	D.V

The local pinpower agreement is also too good for such a "hard" problem, probably coming from a cancellation of errors. The pinpower comparison tends to show the same trend as already observed in both previous problems, the agreement with the reference pinpower prediction is better in the lower part of the problem because the leakage plays a lesser role, making the diffusion solution in the axial direction less of a liability. In the vicinity of the axial water reflector, i.e. in the upper fuel region, the

neutron leakage plays a more important role, and causes the 2D-1D methodology to predict less accurate results. For the partial current splitting, the differences are 2% and 0.2% respectively, which comes from error cancellation since the accuracy of the results is poor as seen in Fig. 3.5.
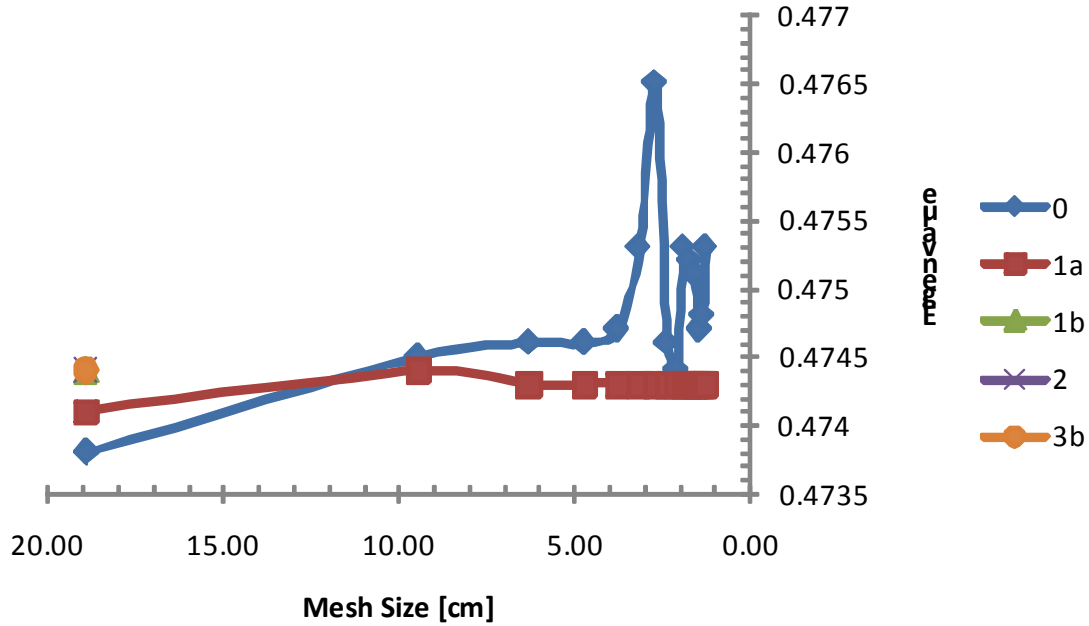
Fig. 3.5. Convergence Behavior of k_{eff} for low density problem

Table 3.11. Relative pinpower difference with the 2D DeCART reference for the lower fuel region for the Low Density case

Number of Planes	Axial Mesh Size[cm]	0	1a	1b	2	3a	3b
3	18.90	0.19	0.19	0.04	0.04	D.V.	0.04
6	9.45	0.00	0.19	D.V	D.V	D.V	135
9	6.30	0.09	0.19	D.V	D.V	D.V	D.V
12	4.73	0.17	0.19	D.V	D.V	D.V	D.V
15	3.78	0.22	0.19	D.V	D.V	D.V	D.V
18	3.15	0.74	0.20	D.V	D.V	D.V	D.V
21	2.70	1.29	0.21	D.V	D.V	D.V	D.V
24	2.36	0.43	0.20	D.V	D.V	D.V	D.V
27	2.10	0.51	0.20	D.V	D.V	D.V	D.V
30	1.89	0.09	0.20	D.V	D.V	D.V	D.V
33	1.72	0.08	0.19	D.V	D.V	D.V	D.V
36	1.58	0.03	0.21	D.V	D.V	D.V	D.V
39	1.45	0.23	0.21	D.V	D.V	D.V	D.V
42	1.35	0.85	0.21	D.V	D.V	D.V	D.V
45	1.26	2.01	0.21	D.V	D.V	D.V	D.V

The difference of about 180 pcm with respect to the reference solution is surprisingly good for a problem where neutron leakage is dominant and should require transport theory to be captured properly. The pinpower predictions, shown in and Table 3.11 and Table 3.12, show that the difference from the reference solution is less than 0.2% for the finest spatial mesh for the lower fuel region, where the error is about 0.6% for the upper mesh, for the option 1a.

The convergence flaws of the 2D-1D methodology have been highlighted in the Low Density case and the proposed fix based on splitting of the transverse leakage has worked successfully, making high neutron leakage in the axial direction possible to model with DeCART. The partial current splitting, although converging, has a poor accuracy and should not be used. For options 1a and 3a, the accuracy of the DeCART solution for such a high leakage case is still questionable since the axial solver still uses diffusion theory which tends to return poor results in leakage dominated problems. This emphasizes the importance of upgrading the DeCART axial solver to be able to perform transport calculations.

Table 3.12. Relative pinpower difference with the 2D DeCART reference for the upper fuel region for the Low density case

Number of Planes	Axial Mesh Size [cm]	0	1a	1b	2	3a	3b
3	18.90	0.22	0.51	0.08	D.V.	0.00	0.08
6	9.45	0.15	0.58	D.V	D.V	D.V	135
9	6.30	0.11	0.70	D.V	D.V	D.V	D.V
12	4.73	0.28	0.65	D.V	D.V	D.V	D.V
15	3.78	0.38	0.71	D.V	D.V	D.V	D.V
18	3.15	2.05	0.67	D.V	D.V	D.V	D.V
21	2.70	3.46	0.69	D.V	D.V	D.V	D.V
24	2.36	0.78	0.68	D.V	D.V	D.V	D.V
27	2.10	0.94	0.66	D.V	D.V	D.V	D.V
30	1.89	0.15	0.66	D.V	D.V	D.V	D.V
33	1.72	0.12	0.68	D.V	D.V	D.V	D.V
36	1.58	0.12	0.68	D.V	D.V	D.V	D.V
39	1.45	0.12	0.68	D.V	D.V	D.V	D.V
42	1.35	0.06	0.68	D.V	D.V	D.V	D.V
45	1.26	0.25	0.67	D.V	D.V	D.V	D.V

Above the data table, spanning all value columns: % Relative pinpower difference for upper fuel region

3.4.4. *Impact of improvements on calculation cost*

In order to assess the effect of the different transverse leakage approximations and coupling techniques on the computing cost of a DeCART calculation, the Water Hole case was run for 10 subdivisions of the initial mesh structure, i.e. 30 MOC planes in each 3D model. All calculations were performed on an idle personal computer to insure

consistency of results: i.e. only DeCART was running at the time the computing time was recorded.

The memory requirements as well as the total computing time and the computing time per outer iteration are summarized in the Table 3.13.

Table 3.13. Computational cost for each transverse leakage option

Option	0	1a	1b	2	3a	3b
Memory Requirement [Mb]	9.39	9.39	9.39	9.39	9.72	9.39
Total Time [s]	34.01	22.12	21.27	26.12	28.82	25.88
Number of Outer Iterations	141	90	88	93	93	93
Time per Iteration [s]	0.24	0.25	0.24	0.28	0.31	0.28

As expected, the memory requirements of all the options are identical besides the P1 coupling with splitting, since an additional memory structure to store the axial leakage and its associated leakage cross section. However, the memory increase is marginal. In terms of running time, all the methods involving an isotropic leakage at the planar interface, option 0, 1a and 1b, require less time per iteration, since only half of the polar angles belonging to the same half space need to be tracked. The gain is not as important as expected, but this is due to the small size of the problem. For a full core model, the saving of those options will be more evident.

3.5. Summary

The limitations of the current 2D-1D coupling have been investigated in the section 3.1. Five new 2D-1D coupling approaches have been derived and successfully implemented in DeCART in order to investigate the potential for improving the convergence properties of the 2D-1D methodology in the case of low density, high neutron leakage cases and improving the accuracy of the solution for a given axial mesh. The latter is particularly important for the purpose of performing 3D full core calculations since the axial mesh dictates the number of MOC sweeps to be performed per outer iteration.

Two new approximations were investigated to represent the angular flux on the top and bottom of a MOC plane: one where the axial leakage is considered isotropic and a second one where a linear approximation of the angular flux (P_1 approximation) is used. The main benefit of the isotropic leakage approximation is to reduce by a factor of 2 the number of MOC polar angles considered, thereby reducing the computing cost of the MOC solver. Conversely the P_1 coupling approach allows complete consistency between the axial solver and the transverse leakage provided to the MOC solver: both are based on the P_1 expansion of the angular flux.

47

To address the issues related to negative MOC source terms, the axial leakage in the 2D transport formulation, Eq. 3.1, was split between the LHS and RHS. Three different splitting were considered, two related to the previously mentioned new coupling approaches, isotropic leakage and P_1 coupling, and the last one based on a rearrangement of the partial currents.

The three test cases considered have shown that:

- In all cases, the P_1 coupling failed to improve the accuracy of the calculation for a given axial mesh.
- The isotropic leakage based coupling produced results as accurate as DP_0 and P_1 coupling while reducing the computational burden.
- The negative source term which was isolated as the main reason for divergence of 3D calculations was fixed successfully by the transverse leakage splitting formulation and worked very well for Low Density case.

The newly added user's options have improved the convergence properties of the 2D-1D coupling methodology, provided that the CMFD acceleration was turned off. Improvements to the accuracy have not been observed, all three coupling approximations return almost identical local power prediction. The initial thought that the discrete 2D-1D equations may not provide a spatial convergence when the numerical grid is refined have been invalidated, at least until a mesh size equivalent to the radial mesh is used. This was examined using a set of problems representative of the conditions in a PWR both under normal and accidental conditions. It should be noted that such low density conditions as examined here are unlikely to be observed in the context of typical LWR transients such as a RIA. However, future analysis of LOCA events will certainly produce high neutron leakage conditions and the improvements to the DeCART should be able to handle such conditions.

Future work will include an investigation of the convergence properties of the CMFD algorithm for the various new 2D-1D splitting methods introduced here, since without CMFD, full core steady state and transient calculations will not be practical.

4. Improvement of the axial solver

One of the principle approximations of the 2D-1D algorithm in DeCART is the axial 1D solver. The presence of heterogeneity in the axial direction (partially inserted control assembly, severe void variation, part length fuel rod, axial enrichment zoning, etc …) can potentially lead to 3D solutions of poor accuracy. The current 2D-1D algorithm available in DeCART provides a 1D axial solution based on diffusion theory whose accuracy deteriorates in regions of strong flux gradients, such as the one observed for the problems listed above.

The present chapter is aimed at describing the implementation in DeCART of an axial solver based on transport theory. A literature review is presented first to show what are the potential solvers and their limitations. It is followed by the mathematical derivation of the NEM-Sn method. The NEM-Sn method resolves the spatial variation of the flux through the Nodal Expansion Method (NEM) and its angular variation through the discrete ordinate method (Sn). The next section is devoted to the description of the NEM-Sn implementation in DeCART. In order to reduce the computational cost and improve the accuracy of the calculations, an existing algorithm, the sub-plane scheme is implemented in DeCART. It is described in the fourth section. The last section provides a summary of a set of calculations performed by DeCART for the C5G7 benchmark problem.

4.1. Literature Review

Few codes are based on the 2D-1D methodology: CHAPELET(Kosaka and Takeda 2004), CRX (Cho and Lee 2006) and DeCART (KAERI version) (Cho, Kim et al. 2007). All three are capable of performing 3D explicit whole core analysis by linking radial 2D MOC solutions to an axial solver to take into account the axial neutron transport.

In the CHAPLET code, the method of characteristics is employed as a radial 2D solver, and a finite difference method (FDM), nodal expansion method (NEM) in diffusion theory or MOC can be chosen as an axial 1D solver. The MOC is based on the flat source region approximation, where the fission and scattering source is assumed to be constant throughout the spatial mesh. In order to achieve a reasonable accuracy, a fine mesh is needed involving a very detailed spatial mesh in the axial direction, requiring a large number of planes, and consequently a number of 2D MOC calculations prescriptive in order to perform accurate full core calculations in a reasonable amount of time. Additionally, as discussed in Chapter III, convergence problems that originate from the transverse leakage coupled scheme tends to happen for a very fine axial mesh.

In the CRX code, the MOC is used for radial 2D heterogeneous calculation and Sn-like methods such as diamond difference (DD) scheme is used for the axial 1D calculation. Similarly to CHAPELET, in order to achieve accurate results, a fine axial mesh is needed, making full core calculations based on 1D transport kernel not practical.

Various advanced nodal transport methods have been developed for an accurate and efficient core neutronics calculation (Smith 1986; Lee and Downar 2004). In these methods, the Simplified Pn (SPn) approximation has been popular as a transport method since it can produce an accurate transport solution with a minimal modification of the existing diffusion code. In the KAERI version of DeCART, a Simplified P_n (SP_n) solver replaces the axial diffusion solver of the DeCART direct whole core transport code to provide more accurate, transport theory based axial solutions. In solving the SPn equations, the NEM is applied to treat the axial variations of the angular moments. Two different orders of SPn are available, SP_3 and SP_5. DeCART-KAERI was tested against the C5G7 benchmark problem and the addition of an axial nodal transport based solver proved to be very worthwhile (Cho, Kim et al. 2007).

As far as the 2D-1D methodology is concerned, a direct correspondence between the discrete directions considered in the 2D MOC and the chosen axial solver would provide a benefit in terms of consistency. No extrapolation would be required to estimate the angular flux in a given direction from the SPn angular flux moments. Although the SPn method has been popular for full core transport calculations, its accuracy is also an issue (Brantley and Larsen 2000). A different transport solver is considered. As already mentioned above, both Sn and MOC have been used. Because of a simpler implementation and relative lower computational cost, the Sn method was chosen for the work here. The spatial variation of the fluxes is still handled through nodal methods.

Besides the NEM method, both the SANM and Analytic Nodal Method (ANM) (Lee, Downar et al. 2004) are potential methods to resolve the spatial variation of the flux. SANM and NEM are currently used in the axial diffusion solver of the DeCART code. Both SANM and ANM use exponential functions to represent, respectively, the source term and the flux which, in the limit of optically thin or thick medium, can create numerical instabilities (Thomas 2006). Finally, the NEM methodology is chosen to resolve the spatial variation of the flux and the Sn method, its angular dependence. The derivation of the NEM-Sn method is presented next.

4.2. NEM-Sn derivation

The following derivation is given for a 1-D problem. The incorporation in the framework of the 2D-1D methodology is described in the next section.

4.2.1. Legendre Polynomials

The derivation of the NEM-Sn method begins with definitions of the node and expansion coefficients. The node is the name of a spatial mesh in nodal method. Its length h is first normalized so it ranges from -1 to 1 by defining a new spatial variable, ξ:

$$\xi = \frac{2z}{h}$$

Eq. 4.1

This normalization makes it convenient to expand the flux using Legendre polynomials. The first five Legendre Polynomials are listed below:

$$P_0(\xi) = 1, P_1(\xi) = \xi, P_2(\xi) = \frac{1}{2}(3\xi^2 - 1),$$

Eq. 4.2

$$P_3(\xi) = \frac{1}{2}\left(5\xi^3 - 3\xi\right), \; P_4(\xi) = \frac{1}{8}\left(35\xi^4 - 30\xi^2 + 3\right)$$

The spatial variation of the angular flux is expanded to the 4th order using the Legendre Polynomials:

$$\varphi_{g,w}(z) = \sum_{i=0}^{4} \varphi_i P_i(\xi)$$

Eq. 4.3

where φ_i is the ith order moment of the angular flux $\varphi_{g,w}(z)$.

4.2.2. *Discrete Ordinate Method*

The discrete ordinates equations solve for the angular flux based on an angular quadrature set. For a given direction w, the angular flux is obtained from the 1-D Boltzmann equation:

$$\frac{2\mu_w}{h}\frac{\partial}{\partial\xi}\varphi_{g,w}(\xi) + \Sigma_{tg}\varphi_{g,w}(\xi) = \frac{\chi}{4\pi k_{eff}}\sum_{g'=1}^{G}\nu\Sigma_{f,g'}\phi_{g'}(\xi) + \sum_{g'=1}^{G}\Sigma_{s,w\leftarrow w',g\leftarrow g'}\varphi_{g',w'}(\xi)$$

Eq. 4.4

The scalar flux results from the weighted sum of the discrete angular fluxes:

$$\phi_{g'}(\xi) = \sum_{w'=1}^{W}\varphi_{g,w}(\xi)w_{w'}$$

Eq. 4.5

Where $w_{w'}$ are the weights associated to the discrete directions of the angular quadrature. For simplicity of the notations, the energy index g is dropped. Furthermore, the scattering is assumed to be isotropic, Eq. 3.1 becomes:

$$\frac{2\mu_w}{h}\frac{\partial}{\partial\xi}\varphi_w(\xi) + \Sigma_t\varphi_w(\xi) = \frac{Q(\xi)}{4\pi}$$

Eq. 4.6

With

$$Q(\xi) = \frac{\chi}{k_{eff}}\sum_{g'=1}^{G}\nu\Sigma_{f,g'}\phi_{g'}(\xi) + \sum_{g'=1}^{G}\Sigma_{s,g\leftarrow g'}\phi_{g'}(\xi)$$

Eq. 4.7

4.2.3. *Nodal Expansion Method*

Similarly to the diffusion NEM method described in Chapter II, there are 5 unknowns per discrete directions. Therefore 5 constraints are needed:

- Flux continuity at the node interface
- Neutron balance equation, Eq. 4.1.
- 3 weighted residual balance equations which are obtained by in multiplying the neutron balance equation by a Legendre Polynomials P_i and integrating it over [0,1]. The ith weighted residual balance equation is obtained. The neutron balance is identical to the 0th order weighted residual balance.

The NEM is solved in a sweeping fashion, where the incoming angular flux at the node boundary is assumed to be known and the outgoing angular flux is computed. The flux continuity equation at the node interface between the node *n-1* and *n* leads to:

$$\varphi_w(-1) = \varphi_{in} = \sum_{i=0}^{4} \varphi_i P_i(-1) = \varphi_0 - \varphi_1 + \varphi_2 - \varphi_3 + \varphi_4 \qquad \text{Eq. 4.8}$$

The 4 weighted residual equations are obtained by multiplying Eq. 4.1 by a Legendre Polynomial P_i to give:

$$\int_{-1}^{1} \left(\frac{2\mu_w}{h} \frac{\partial}{\partial \xi} \varphi_w(\xi) + \Sigma_t \varphi_w(\xi) \right) P_0(\xi) d\xi = \int_{-1}^{1} \left(\frac{Q(\xi)}{4\pi} \right) P_0(\xi) d\xi = S$$

$$\int_{-1}^{1} \left(\frac{2\mu_w}{h} \frac{\partial}{\partial \xi} \varphi_w(\xi) + \Sigma_t \varphi_w(\xi) \right) P_1(\xi) d\xi = \int_{-1}^{1} \left(\frac{Q(\xi)}{4\pi} \right) P_1(\xi) d\xi = \tilde{S}_1$$

$$\int_{-1}^{1} \left(\frac{2\mu_w}{h} \frac{\partial}{\partial \xi} \varphi_w(\xi) + \Sigma_t \varphi_w(\xi) \right) P_2(\xi) d\xi = \int_{-1}^{1} \left(\frac{Q(\xi)}{4\pi} \right) P_2(\xi) d\xi = \tilde{S}_2 \qquad \text{Eq. 4.9}$$

$$\int_{-1}^{1} \left(\frac{2\mu_w}{h} \frac{\partial}{\partial \xi} \varphi_w(\xi) + \Sigma_t \varphi_w(\xi) \right) P_3(\xi) d\xi = \int_{-1}^{1} \left(\frac{Q(\xi)}{4\pi} \right) P_3(\xi) d\xi = \tilde{S}_3$$

Replacing $\varphi_w(\xi)$ by its polynomial expansion, integrating and rearranging the terms lead to the four equations below:

$$\Sigma_t \varphi_0 + \frac{2\mu_w}{h} (\varphi_1 + \varphi_3) = S$$

$$\frac{\Sigma_t}{3} \varphi_1 + \frac{2\mu_w}{h} (\varphi_2 + \varphi_4) = \tilde{S}_1$$

$$\frac{\Sigma_t}{5} \varphi_2 + \frac{2\mu_w}{h} \varphi_3 = \tilde{S}_2 \qquad \text{Eq. 4.10}$$

$$\frac{\Sigma_t}{7} \varphi_3 + \frac{2\mu_w}{h} \varphi_4 = \tilde{S}_3$$

Together with Eq. 4.8, a complete set of 5 equations and 5 unknowns has been constructed. It can be solved. Given 4 source terms, computed using previous iteration results, and an incoming angular flux, coming from boundary conditions or the outgoing flux of a previous node, the angular flux moments $\varphi_i, i = 0..4$ are obtained and the spatial variation of the angular flux for the direction *w* and energy group *g* is fully determined. The next section described the numerical approach used in DeCART to solve the NEM-Sn equations.

4.3. Numerical NEM-Sn implementation

4.3.1. *Choice of angular quadrature*

In order to insure consistency with the directions chosen in the 2D transport solution, the angular quadrature chosen for the NEM-Sn kernel is the same as chosen for

the polar angle of the 2D MOC solver. Usually for a low number of angles which would be less than four per half space, the quadrature proposed by (Leonard and McDaniel 1995) is used. However, for a higher number of polar directions, the quadrature proposed in (Halsall 1980) is used. Finally, the Gauss-Legendre quadrature has been added to DeCART for the polar directions, up to 8 directions per half space.

4.3.2. *Transverse leakage*

4.3.2.1. *Formulation of the modified 1D equation with transverse leakage*

The NEM-Sn is used in the framework of the 2D-1D methodology. The 1-D equations derived in section 4.2 need to be modified in order to reflect the 3-D movement of the neutrons. The 3-D Boltzmann equation, assuming an isotropic neutron source, is:

$$
\left(\sqrt{1-\mu_w^2} \left(\cos(\alpha_w) \frac{\partial}{\partial x} + \sin(\alpha_w) \frac{\partial}{\partial y} \right) + \mu_w \frac{\partial}{\partial z} \right) \varphi_w(x,y,z,\alpha_w,\mu_w)...
$$

$$
+ \Sigma_t \varphi_w(x,y,z,\alpha_w,\mu_w) = \frac{Q(x,y,z)}{4\pi}
$$

Eq. 4.11

By integrating Eq. 4.11 along the *x* and *y* faces of the considered node and moving the x and y derivatives on the RHS, it becomes:

$$
\mu_w \frac{\partial}{\partial z} \varphi_w^{XY}(z,\alpha_w,\mu_w) + \Sigma_t \varphi_w^{XY}(z,\alpha_w,\mu_w) = \frac{Q(x,y,z)}{4\pi} - TL_w^{XY}(z,\alpha_w,\mu_w)
$$

Eq. 4.12

with

$$
\varphi_w^{XY}(z,\alpha_w,\mu_w) = \frac{1}{A} \int_{y_l}^{y_r} \int_{x_l}^{x_r} \varphi_w(x,y,z,\alpha_w,\mu_w) dx dy
$$

$$
TL_w^{XY}(z,\alpha_w,\mu_w) = \frac{\sqrt{1-\mu_w^2}}{A} \left(\begin{array}{l} \cos\alpha \int_{y^l}^{y^r} \left(\varphi_w(x^r,y,z,\alpha_w,\mu_w) - \varphi_w(x^l,y,z,\alpha_w,\mu_w) \right) dy \\ + \sin\alpha \int_{x^l}^{x^r} \left(\varphi_w(x,y^r,z,\alpha_w,\mu_w) - \varphi_w(x,y^l,z,\alpha_w,\mu_w) \right) dx \end{array} \right)
$$

Eq. 4.13

Theoretically, provided that an azimuthally dependent transverse leakage was available from the 2D MOC calculations, the exact solution of the 3-D Boltzmann equation is possible, the only approximation would be the use of transverse leakage, i.e. the averaging of the leakage over the (x,y) faces of the node.

However, in order to reduce both storage and computing time, only a polar dependent transverse leakage is considered. Even with only polar dependent transverse leakage, the need for additional storage is significant, since the azimuthally integrated, polar dependent angular flux from each 2D MOC plane is stored for each node faces. In DeCART, a node corresponds to an axial segment of a fuel rod, typically an elongated cube of 1.26 by 1.26 by 20 cm. There are about 150 000 nodes in a full PWR core model.

Consequently, the azimuthal variation of Eq. 4.12 is integrated to give the following:

$$\mu_w \frac{\partial}{\partial z} \overline{\varphi}_w^{XY}(z, \mu_w) + \Sigma_t \overline{\varphi}_w^{XY}(z, \mu_w) = \frac{Q(z)}{4\pi} - \overline{TL}_w^{XY}(z, \mu_w)$$

Eq. 4.14

with

$$\overline{\varphi}_w^{XY}(z, \mu_w) = \int_0^{2\pi} \varphi_w^{XY}(z, \alpha_w, \mu_w) d\alpha_w$$

Eq. 4.15

$$\overline{TL}_w^{XY}(z, \mu_w) = ...$$

$$\frac{\sqrt{1-\mu_w^2}}{A} \int_0^{2\pi} \left(\begin{array}{l} \cos\alpha \int_{y^l}^{y^r} \left(\varphi_w(x^r, y, z, \alpha_w, \mu_w) - \varphi_w(x^l, y, z, \alpha_w, \mu_w)\right) dy \\ + \sin\alpha \int_{x^l}^{x^r} \left(\varphi_w(x, y^r, z, \alpha_w, \mu_w) - \varphi_w(x, y^l, z, \alpha_w, \mu_w)\right) dx \end{array} \right) d\alpha_w$$

Eq. 4.16

Eq. 4.15 is very similar to the starting point for the NEM-Sn derivation, Eq. 4.1, if the transverse leakage is incorporated in the source term on the LHS. The four weighted residual balances source terms of Eq. 4.10 are modified by the corresponding moments of the transverse leakage. The next section is dedicated to the definition and calculations of the moments of the transverse leakage.

4.3.2.2. *Transverse Leakage Approximation*

The accuracy of the spatial variation of the angular flux in NEM-Sn solution increases as the axial node size decreases. Thus it is better to employ thinner planes when formulating the 3D problem. However, it is not always desirable to reduce the plane thickness since this will result in the increase of the number of planes for each of which the radial MOC calculations which have to be performed or potentially cause some convergence issue as seen in Chapter III. Since the MOC calculations are costly, it is better to avoid using very thin planes. However, to retain accuracy, the axial variation of the transverse leakage within a node needs to be taken into account. A typical quadratic expansion of the transverse leakage is then used:

$$\overline{TL}_w^{XY}(\xi, \mu_w) = \sum_{i=0}^{2} a_i P_i(\xi)$$

Eq. 4.17

Where a_i is the ith transverse leakage moment and P_i the ith Legendre Polynomial.

For a given spatial mesh l, the expansion coefficients are determined from the mesh averaged transverse leakage $\overline{\overline{TL}}_w^{XY}$ and the transverse leakages at the top and bottom surfaces as followings:

$$a_0 = \overline{\overline{TL}}_{w,l}^{XY}(\mu_w)$$

Eq. 4.18

$$a_1 = \frac{\overline{\overline{TL}}_{w,l}^{XY,T}(\mu_w) - \overline{\overline{TL}}_{w,l}^{XY,B}(\mu_w)}{2}$$

$$a_2 = \overline{\overline{TL}}_{w,l}^{XY} - \frac{\overline{\overline{TL}}_{w,l}^{XY,T}(\mu_w) + \overline{\overline{TL}}_{w,l}^{XY,B}(\mu_w)}{2}$$

Where $\overline{\overline{TL}}_{w,l}^{XY,B}$ and $\overline{\overline{TL}}_{w,l}^{XY,B}$ are the transverse leakages at the top and bottom surfaces of the considered node l. They are calculated from the mesh averaged transverse leakages of neighboring nodes so as to preserve the mesh averaged leakage:

$$\overline{\overline{TL}}_{w,l}^{XY,B} = \frac{\dfrac{\overline{\overline{TL}}_{w,l}^{XY}(\mu_w)}{h^l} + \dfrac{\overline{\overline{TL}}_{w,l-1}^{XY}(\mu_w)}{h^{l-1}}}{\dfrac{1}{D^l} + \dfrac{1}{h^{l-1}}}$$

$$\overline{\overline{TL}}_{w,l}^{XY,T} = \frac{\dfrac{\overline{\overline{TL}}_{w,l}^{XY}(\mu_w)}{h^l} + \dfrac{\overline{\overline{TL}}_{w,l+1}^{XY}(\mu_w)}{h^{l+1}}}{\dfrac{1}{h^l} + \dfrac{1}{h^{l+1}}}$$

Eq. 4.19

The first, second and third moments of the transverse leakage term are obtained by multiplying Eq. 4.17 by its proper Legendre Polynomials and integrating over the spatial mesh size. The j$^{\text{th}}$ moment of the transverse leakage is then defined as follow:

$$\tilde{T}L_w^{XY,j}(\xi, \mu_w) = \int_{-1}^{1} \sum_{i=0}^{2} a_i P_i(\xi) P_j(\xi) d\xi$$

Eq. 4.20

By properties of the Legendre Polynomials, it comes:

$$\tilde{T}L_w^{XY,j}(\xi, \mu_w) = a_j \int_{-1}^{1} P_j(\xi) P_j(\xi) d\xi$$

Eq. 4.21

And since the transverse leakage is a second order polynomial, the contribution of the third moment of the transverse leakage to the source is equal to zero.

4.3.2.3. 2D-1D modified weighted residual equations

Given the previous definition for the j$^{\text{th}}$ moment of the transverse leakage, the 4 weighted residual equations become:

$$\Sigma_t \varphi_0 + \frac{2\mu_w}{h}(\varphi_1 + \varphi_3) = S - a_0$$

$$\frac{\Sigma_t}{3} \varphi_1 + \frac{2\mu_w}{h}(\varphi_2 + \varphi_4) = \tilde{S}_1 - \frac{a_1}{3}$$

Eq. 4.22

$$\frac{\Sigma_t}{5} \varphi_2 + \frac{2\mu_w}{h} \varphi_3 = \tilde{S}_2 - \frac{a_2}{5}$$

$$\frac{\Sigma_t}{7}\varphi_3 + \frac{2\mu_w}{h}\varphi_4 = \tilde{S}_3$$

4.3.3. *Solver for the NEM-Sn system of equations*

The flow chart of the NEM-Sn solver is shown in the Fig. 4.1. The NEM-Sn solver takes employs a sweeping approach per half-space polar direction. For each spatial mesh in the axial direction, a 5 by 5 NEM-Sn response matrix is generated with the Eq. 4.8 and Eq. 4.22 and solved by direct LU decomposition to determine the φ_i coefficients for the considered axial mesh, polar direction and energy group.

Given the small size of the NEM-Sn response matrix, a direct solver is acceptable in terms of computational cost. Additional inner iterations per fuel rod are aimed at converging the scattering source faster. It is a user's option. 5 is the default value and it has been chosen as being the optimum value for LWR applications.

Finally, the angular fluxes, and consequently, the φi coefficients, are not stored for each axial mesh, only the moments of the scalar fluxes are kept to reduce the memory requirements of the NEM-Sn solver. The angular flux at the problem boundary, on top and at the bottom of the geometry is kept in memory as well.

4.3.4. *Sub-plane Scheme*

The error introduced in each part of the DeCART solution had been quantified for a typical problem in (Cho, Kim et al. 2006). Specifically, the homogenization error, the diffusion approximation error, and the nodal solution error were separately evaluated for a LWR problem. The main conclusion of the work presented in the reference above, is that the homogenization error is small but the nodal and the diffusion errors can be large. The nodal error originates from the second order approximation of the axial variation of the radial transverse leakage as well as the fourth order intra-nodal flux shape, while the diffusion error is attributable to neglecting the angular dependence of the flux in the axial direction.

The diffusion and the nodal errors can be minimized by introducing a fine mesh transport solution for the axial direction that is realized in some codes (Kosaka and Takeda 2004; Cho and Lee 2006). However, a fine mesh calculation for the axial direction requires an increased computing time. In order to minimize the higher computing cost, a sub-plane scheme has been introduced in (Cho, Kim et al. 2007) and was successful in minimizing the nodal error while maintaining a reasonable computing time. The sub-plane scheme has been implemented in the DeCART code and is briefly described below, a more complete description is available in (Cho, Kim et al. 2007).

In the sub-plane scheme, the radial MOC calculation is performed for a thick plane whereas the axial calculation is performed with finer planes. Several sub-planes belonging to a thick MOC plane share radial equivalent constants which consist of the homogenized group constants and the radial transverse leakage determined for the thick MOC plane. The axial solver in DeCART which can be either NEM or NEM-Sn, uses a fine axial mesh and returns an axial transverse leakage to the radial MOC calculation at

each thick plane. The sub-plane scheme introduces much less nodal error while having little impact on the axial leakage representation of the radial MOC calculation.

```
┌─────────────────────┐         ┌─────────────────────┐
│ New outer iteration  │────────▶│  Update fission source │
└─────────────────────┘         └─────────────────────┘
                                           │
                                           ▼
                                ┌─────────────────────┐
                                │ Compute Transverse Leakage │
                                │ shape function coefficients │
                                └─────────────────────┘
                                           │
                                           ▼
                                ┌─────────────────────┐
                                │ Add transverse leakage source │
                                │   to fission source  │
                                └─────────────────────┘
                                           │
                                           ▼
                                ┌─────────────────────┐
                                │ Update scattering source │◀────┐
                                └─────────────────────┘         │
                                           │                    │
                                           ▼                    │
                                ┌─────────────────────┐         │
                                │ Sweep through axial geometry │  │
                                │ for a given polar direction │  │
                                └─────────────────────┘         │
                                           │                    │
                                           ▼                    │
                                ┌─────────────────────┐         │
                                │ Construct NEM-Sn response │    │
                                │        matrix        │        │
                                └─────────────────────┘         │
                                           │                    │
                                           ▼                    │
┌─────────────────────┐         ┌─────────────────────┐  ┌──────────────────┐
│ 5 iterations per fuel rod │   │ Direct solution of the matrix │ │ Loop over energy group │
└─────────────────────┘         │  by LU decomposition │  └──────────────────┘
                                └─────────────────────┘
                                           │
                                           ▼
            ┌─────────────────────┐  ┌─────────────────────┐
            │ Loop over half space polar │ │ Sweep through axial geometry │
            │     directions       │  │ for the opposite polar direction │
            └─────────────────────┘  └─────────────────────┘
                                           │
                                           ▼
                                ┌─────────────────────┐
                                │ Construct NEM-Sn response │
                                │        matrix        │
                                └─────────────────────┘
                                           │
                                           ▼
                                ┌─────────────────────┐
                                │ Direct solution of the matrix │
                                │  by LU decomposition │
                                └─────────────────────┘
                                           │
                                           ▼
                                ┌─────────────────────┐
                                │ Update axial transverse │
                                │       leakage        │
                                └─────────────────────┘
                                           │
┌─────────────────────┐                    ▼
│ Next outer iteration │◀──────────────────┘
└─────────────────────┘
```

Fig. 4.1. NEM-Sn Flow chart for axial transport solver

(a) 1D Axial Fuel Rods   (b) Global 3D Problem   (c) 2D MOC Planes
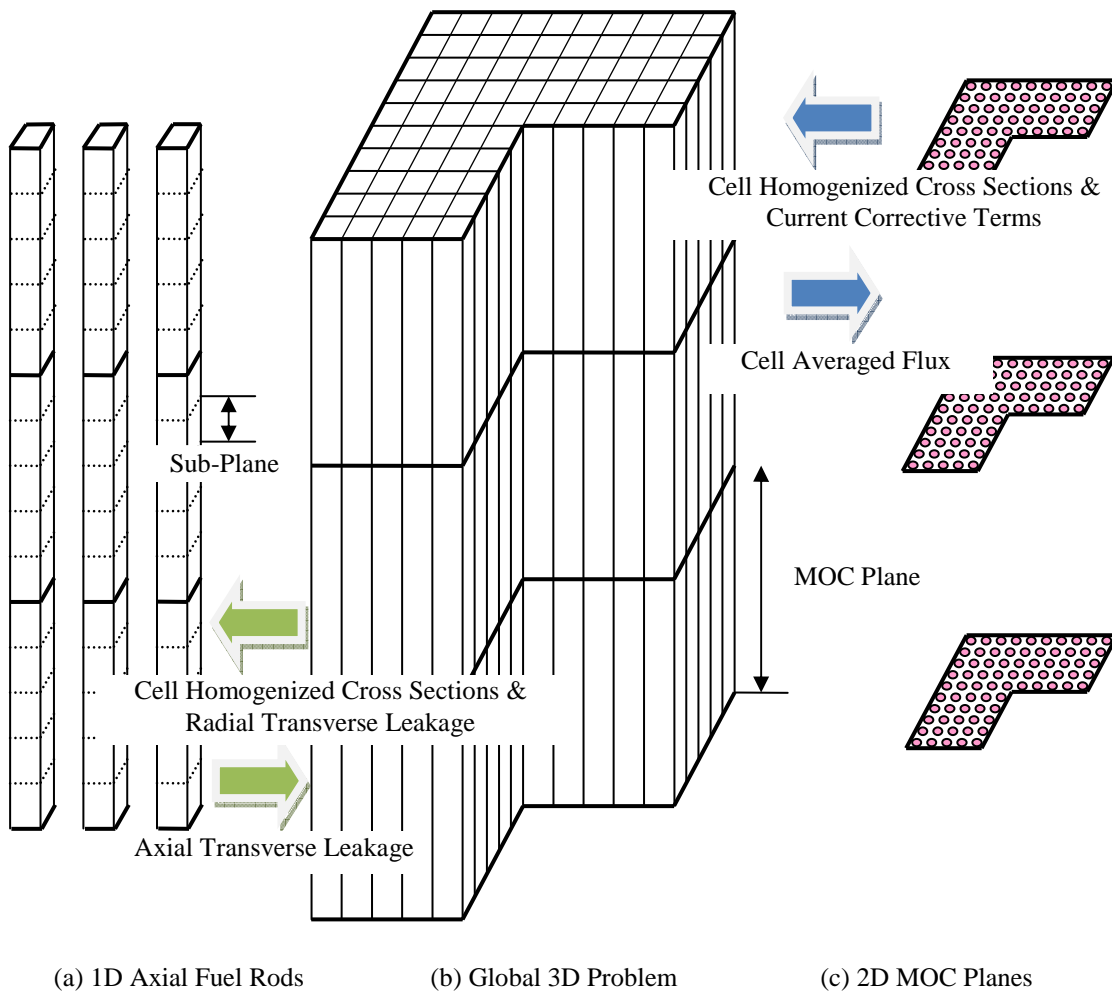
Fig. 4.2. Components and relations of the radial and axial problems in sub-plane scheme

4.4. Application: C5G7 benchmark

4.4.1. *Benchmark description*

The problem specifications of the C5G7 benchmark consist of the core geometry data and the seven group macroscopic cross sections specified for each material composition including the UOX and MOX fuel pins and also the control rods. A description of the core geometry is shown in the Fig. 4.3, Fig. 4.4 and Fig. 4.5. There are three configurations defined: Unrodded, Rodded A, and Rodded B. Among the two rodded configurations, Rodded B configuration is more heavily rodded. For all these three problems, a reflective boundary condition is applied to the bottom boundary which leads to unrealistic conditions, but more challenging problems. The reference solutions generated with the MCNP code is available for a comparison. The core effective multiplication coefficients k_{eff} is computed for each configuration and the pin wise power distributions were axially averaged for three equal thicknesses axial slices of the active

core for comparison purposes. The base DeCART model consists of four planes; three 14.28 cm planes for the fuel region and one 21.42 cm plane for the axial reflector region. Within each fuel cell, 40 flat source regions consisting of five annular regions and eight azimuthal sectors are defined. Two annular regions are assigned in the moderator region. The three fuel annular regions have the same area.
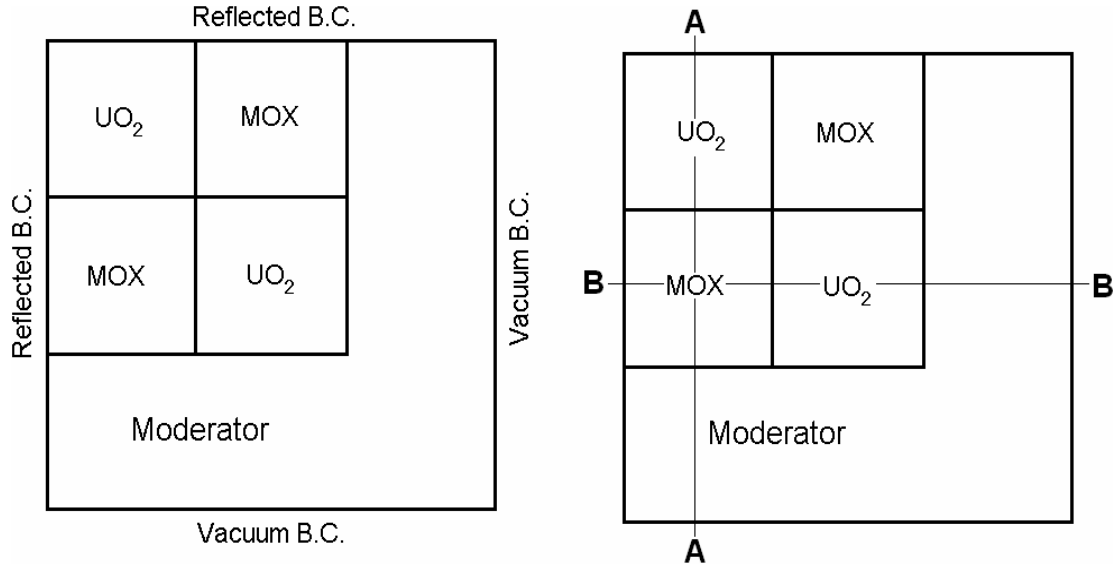
Fig. 4.3. Radial Cross Section of the C5G7 core
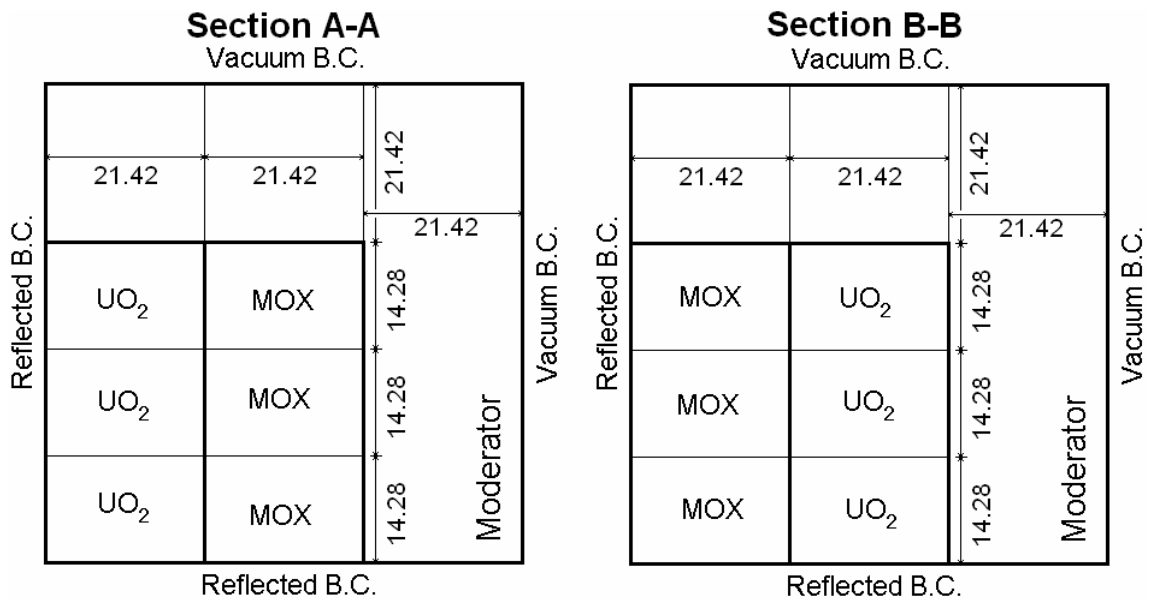
Fig. 4.4. Axial Cross Section of the C5G7 core
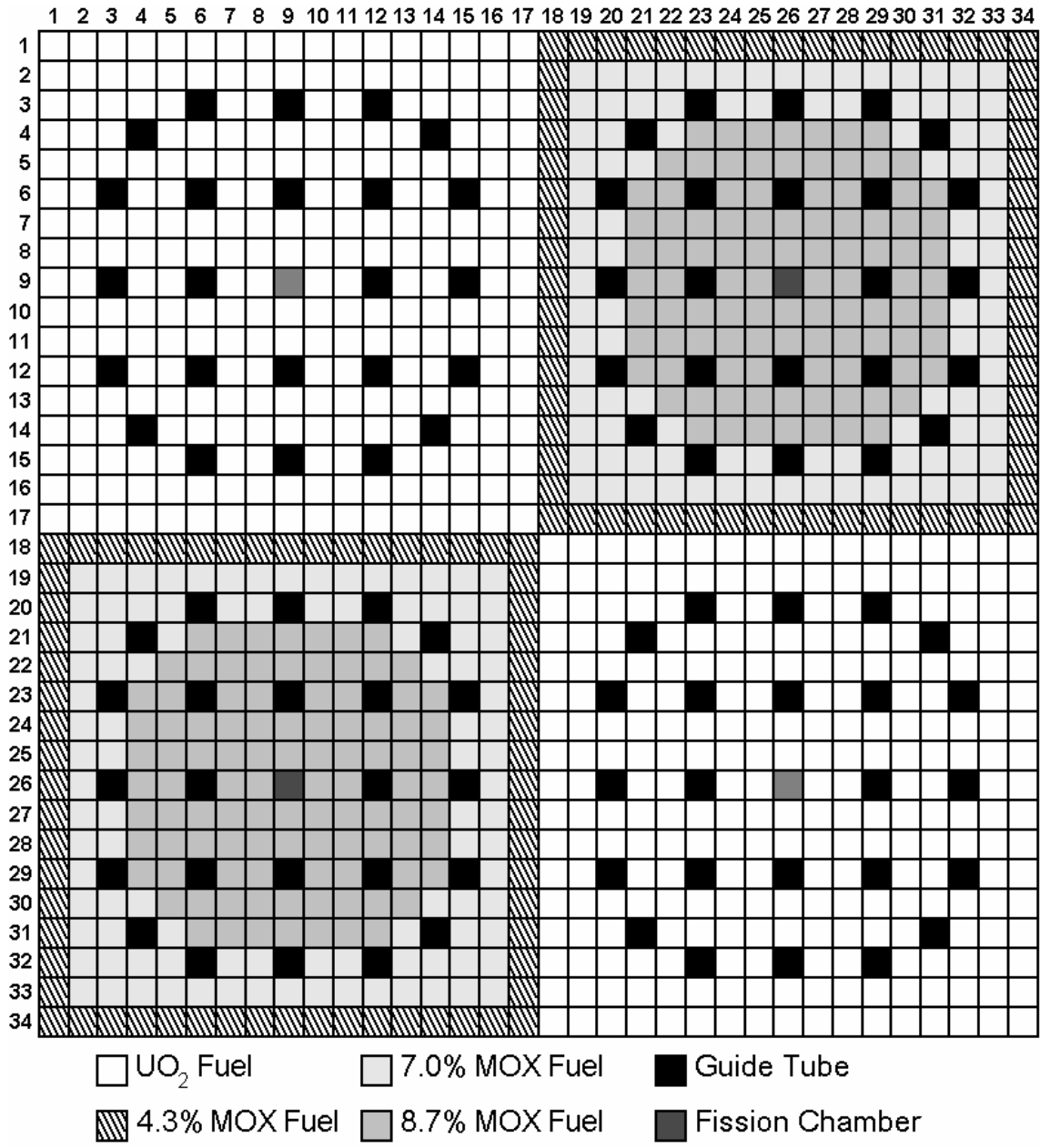
Fig. 4.5. Benchmark fuel pin compositions

4.4.2. *Results*

For each of the three configuration of the C5G7 benchmark, the effective multiplication coefficient as well as the pinpower are recorded and compared to a reference solution obtained with a Monte Carlo based code (MCNP) provided with the benchmark results.

To assess the overall pinpower distribution, the following per cent error measures were selected in the benchmark: average pinpower per cent error (AVG), root mean square (RMS) of pinpower per cent error distribution, mean relative pinpower per cent

error (MRE) and the maximum pinpower per cent error (MAX). The definitions of those quantities are shown in Eq. 4.23 below.

$$AVG = \frac{\sum_N |e_n|}{N}$$

$$RMS = \sqrt{\frac{\sum_N e_n^2}{N}}$$

$$MRE = \frac{\sum_N |e_n| \cdot p_n}{N \cdot p_{avg}}$$

Eq. 4.23

Where N is the number of fuel pins, e_n is the computed relative per cent error for the nth pinpower p_n.

This problem was previously solved by the DeCART code by using the diffusion NEM option and the solution accuracy was reported (Cho, Kim et al. 2006). The previous work showed that the eigenvalue and the power distribution errors are sensitive to the axial plane division, but not sensitive to the ray density and the number of azimuthal and polar directions considered. Therefore, in the examination of the newly developed axial solver, the ray option is fixed by using 4 azimuthal and 2 polar angles for each octant of the unit sphere to define the solid angle, and 0.05 cm ray spacing, and the effects of the sub-planes and the increase of the number of polar directions in the axial solver are examined.

4.4.2.1.   Effect of axial angular discretization

The effect of the Sn order is first analyzed to determine a proper angular discretion for the axial solver. The rodded configuration B is used as test case and its MCNP solution as reference. 2, 4, 8 and 16 polar directions are considered for the NEM-Sn solver. The effective multiplication coefficient and the pinpower comparison are shown in Table 4.1. The computing cost, CPU time and memory requirement is shown in Table 4.2. The calculations are run on the RESERV cluster of ANL, on four PENTIUM 3.0 GHz processors.

In terms of k_{eff} and power error, the increase of number of polar directions lead to an error reduction compared to the reference solution. The difference of k_{eff} goes from 150 pcm to about 7pcm difference while the maximum power error goes from 7% to about 4%.

The computational time increases more than linearly with the number of polar directions considered. The memory allocation required also increases when the number of polar directions considered. The increase is due to the additional storage of the angular flux at the problem boundary as well as polar dependent transverse leakage.

Consequently, increasing the number of polar directions from 4 to 16 does not improve the agreement with MCNP while it does increase the computing cost. Two polar angles per half space, i.e. S4 are enough to obtain a converged axial solution. This discretization is chosen for all the following NEM-Sn calculations.

Table 4.1. k_{eff} and powers errors for the polar angle discretization

Solver		NEM-Sn			
Order of Sn		2	4	8	16
Reference keff		1.07777			
keff difference[pcm]		-154.9	-10.2	6.5	7.4
Slice 1 Pin Power Error [%]	Maximum	4.2	2.7	2.4	2.2
	Mean	0.7	0.6	0.6	0.5
	RMS	1.0	0.8	0.7	0.7
	MRE	0.4	0.4	0.3	0.3
Slice 2 Pin Power Error [%]	Maximum	4.2	2.3	2.1	2.1
	Mean	0.9	0.7	0.6	0.6
	RMS	1.3	0.8	0.8	0.8
	MRE	0.3	0.2	0.2	0.2
Slice 3 Pin Power Error [%]	Maximum	7.6	6.0	5.8	5.7
	Mean	2.8	2.1	1.9	1.8
	RMS	3.4	2.7	2.5	2.3
	MRE	0.4	0.3	0.3	0.3
Axially Integrated Pin Power Error [%]	Maximum	4.2	2.4	2.1	2.0
	Mean	0.6	0.4	0.4	0.4
	RMS	1.0	0.6	0.5	0.5
	MRE	0.5	0.3	0.3	0.3

Table 4.2. Computational Requirements for the polar angle discretization

Solver	*NEM-Sn*			
Order of Sn	2	4	8	16
CPU time [s]	5594.1	10629	24660	57719
Memory Requirement [Mb]	286.4	369.4	535.4	867.4

4.4.2.2. Unrodded Case

The unrodded configuration is shown in the Fig. 4.6 below.

Section A-A
Vacuum B.C.

Reflected B.C.

UO₂	MOX
UO₂	MOX
UO₂	MOX

21.42
14.28
14.28
14.28

Moderator
Vacuum B.C.

Reflected B.C.

Section B-B
Vacuum B.C.

Reflected B.C.

MOX	UO₂
MOX	UO₂
MOX	UO₂

21.42
14.28
14.28
14.28

Moderator
Vacuum B.C.

Reflected B.C.
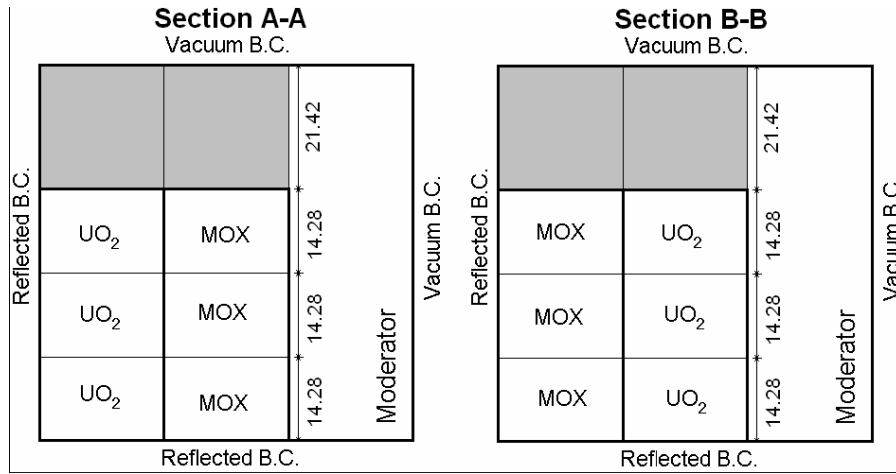
Fig. 4.6. Unrodded Configuration of the C5G7 benchmark

Table 4.3. k_{eff} and power errors for the unrodded configuration of the C5G7MOX 3-D benchmark problem

Solver		NEM		NEM-Sn	
Sub-Planes per MOC Plane		1	10	1	10
Reference keff		1.1431			
keff difference[pcm]		-151.3	-95.4	-48.1	-40.2
Slice 1 Pin Power Error [%]	Maximum	2.9	2.1	2.1	2
	Mean	0.4	0.6	0.6	0.7
	RMS	0.7	0.7	0.7	0.8
	MRE	0.1	0.3	0.3	0.3
Slice 2 Pin Power Error [%]	Maximum	2.8	2.4	2.3	2.3
	Mean	0.5	0.5	0.3	0.5
	RMS	0.6	0.6	0.5	0.6
	MRE	0.1	0.2	0.1	0.2
Slice 3 Pin Power Error [%]	Maximum	2.5	4.1	3.2	4.1
	Mean	0.5	2	1.2	2.1
	RMS	0.7	2.2	1.3	2.2
	MRE	0.1	0.4	0.2	0.4
Axially Integrated Pin Power Error [%]	Maximum	2.7	2.5	2.3	2.4
	Mean	0.4	0.4	0.3	0.4
	RMS	0.6	0.6	0.5	0.5
	MRE	0.3	0.3	0.2	0.3

It is a fairly homogeneous geometry; the control rod is not inserted in the active fuel region, only in the upper water reflector. The computational results for this benchmark problem are summarized in the Table 4.3.

By increasing the number of sub-planes to 10 per thick MOC plane, the nodal error is reduced, as shown by the DeCART calculation using the NEM solver. k_{eff} is reduced from 150 to about 95 pcm, the axially averaged maximum error being reduced from 2.7 to 2.5%. It is worthwhile to note that the local maximum power error increases from 2.5% to 4%. However, this is not significant because it occurs at a very low power region (slice 3). The absolute error is actually reduced.

The remaining error is due to diffusion theory and is reduced when the new NEM-Sn solver is used. k_{eff} is reduced from 95 to about 40 pcm, the axially averaged maximum error being reduced from 2.5 to 2.4%.

Overall, the improvement in terms of k_{eff} and pinpower prediction is small. It is expected for such a homogeneous case, where the diffusion theory is enough to capture correctly the spatial variation of the neutron flux.

4.4.2.3.   Rodded Case A

The rodded configuration A is shown in the Fig. 4.7 below.
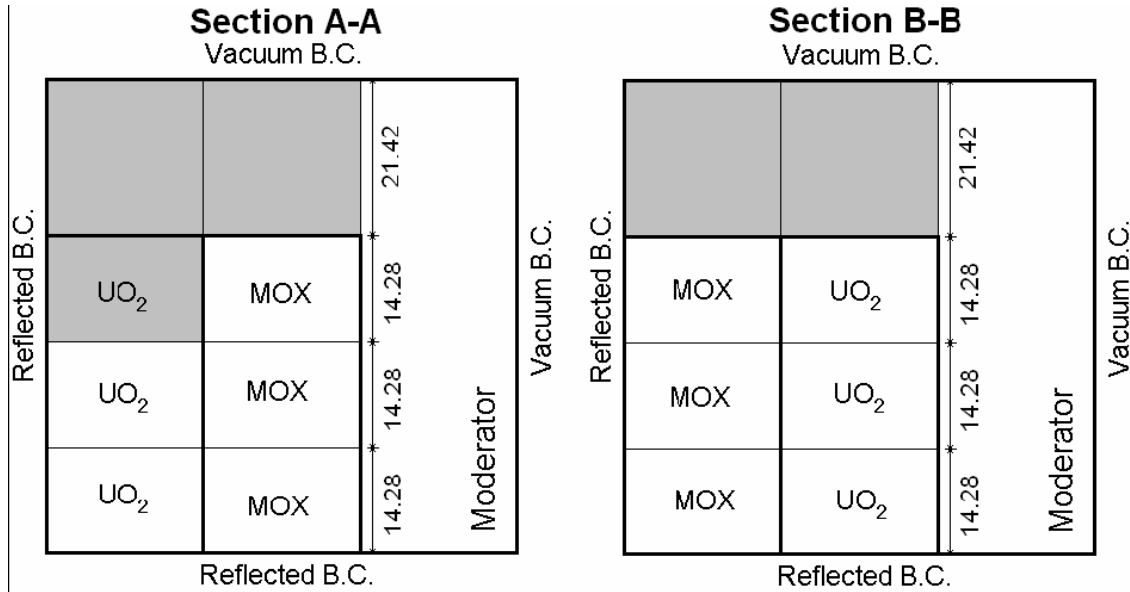
Fig. 4.7. Rodded Configuration A of the C5G7 benchmark

It is a harder problem to model, the control rod is slightly inserted in the active fuel region of the inner most fuel assembly as well as in the upper water reflector. The computational results for this benchmark problem are summarized in the Table 4.4.

By increasing the number of sub-planes to 10 per MOC plane, the nodal error is reduced, as shown by the DeCART calculation using the NEM solver. k_{eff} is reduced from 93 to about 74 pcm, the axially averaged maximum error remaining constant. It is

worthwhile to note that the local maximum power error increases from 2.3% to 6%. However, this is not very significant because it occurs at a very low power region (slice 3), and is due to the relative nature of the error.

Table 4.4. k_{eff} and power errors for the rodded configuration A of the C5G7MOX 3-D benchmark problem

Solver		NEM		*NEM-Sn*	
Sub-Planes per MOC Plane		1	10	1	10
Reference k_{eff}		1.1282			
k_{eff} difference[pcm]		-93.1	-74.5	3.5	-11.5
Slice 1 Pin Power Error [%]	Maximum	2.0	1.6	1.4	1.6
	Mean	0.4	0.6	0.6	0.5
	RMS	0.5	0.7	0.7	0.6
	MRE	0.1	0.3	0.3	0.2
Slice 2 Pin Power Error [%]	Maximum	2.5	2.4	2.1	2.3
	Mean	0.5	0.4	0.5	0.5
	RMS	0.7	0.6	0.7	0.6
	MRE	0.2	0.1	0.2	0.2
Slice 3 Pin Power Error [%]	Maximum	2.3	3.6	2.6	3
	Mean	0.7	1.6	0.8	1.3
	RMS	0.9	1.9	1	1.4
	MRE	0.1	0.2	0.1	0.2
Axially Integrated Pin Power Error [%]	Maximum	2.1	2.2	1.8	2.1
	Mean	0.3	0.4	0.3	0.3
	RMS	0.5	0.5	0.4	0.5
	MRE	0.3	0.3	0.2	0.3

The remaining error is due to the diffusion theory and is reduced when the new NEM-Sn solver is used. k_{eff} is reduced from 74 to about 11 pcm. The distortions introduced in the axial neutron flux by the partially inserted control rod, are more severe than in the unrodded case and the diffusion theory is not capable of capturing them. The NEM-Sn solver improves the accuracy of the calculation.

4.4.2.4.   Rodded Case B

The rodded configuration B is shown in the Fig. 4.8 below.
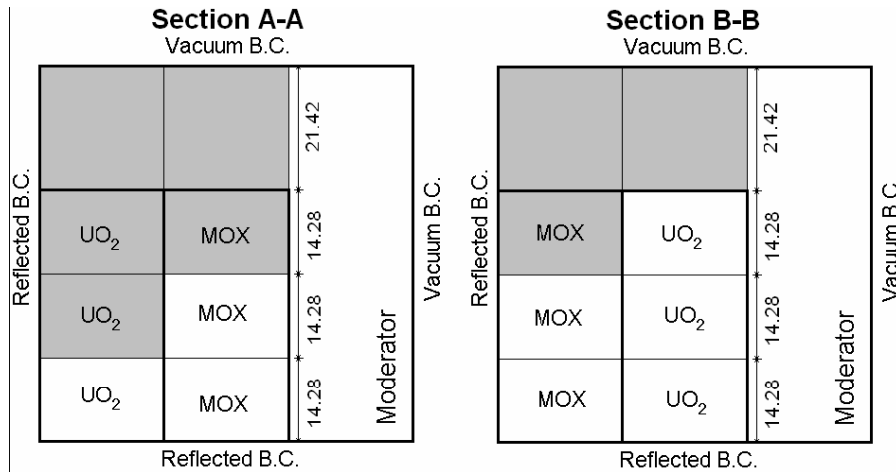
Fig. 4.8. Rodded Configuration B of the C5G7 benchmark

Table 4.5. k_{eff} and power errors for the rodded configuration A of the C5G7MOX 3-D benchmark problem

		NEM		NEM-Sn	
Sub-Planes per MOC Plane		1	10	1	10
Reference k_{eff}		1.07777			
k_{eff} difference[pcm]		-95.6	-110.4	63.1	-12.1
Slice 1 Pin Power Error [%]	Maximum	2.8	2.6	2.0	2.6
	Mean	0.5	0.4	0.6	0.6
	RMS	0.7	0.6	0.8	0.8
	MRE	0.3	0.2	0.4	0.3
Slice 2 Pin Power Error [%]	Maximum	2.5	2.6	1.9	2.2
	Mean	0.5	0.6	0.4	0.6
	RMS	0.7	0.8	0.6	0.8
	MRE	0.1	0.1	0.1	0.2
Slice 3 Pin Power Error [%]	Maximum	6.3	4.5	7.5	5.8
	Mean	2.2	1.6	2.5	2.0
	RMS	2.9	1.9	3.3	2.5
	MRE	0.3	0.2	0.4	0.3
Axially Integrated Pin Power Error [%]	Maximum	2.4	2.7	1.9	2.3
	Mean	0.4	0.5	0.3	0.4
	RMS	0.6	0.7	0.5	0.6
	MRE	0.3	0.4	0.3	0.3

This is the hardest problem of the benchmark to model. The core is heavily rodded with the control rod inserted in the active fuel region of the inner most UO_2 assembly and both of its MOX neighbor. The computational results for this benchmark problem are summarized in the Table 4.5.

By increasing the number of sub-planes to 10 per thick MOC plane, the nodal error is increased, as shown by the DeCART calculation using the NEM solver. k_{eff} is increased from 95 to about 110 pcm. This unexpected behavior comes from the additional nodal error introduced by the heavily rodded configuration. The axially averaged maximum error also increases. The remaining error is due to diffusion theory and is reduced when the new NEM-Sn solver is used. k_{eff} is reduced from 1104 to about 12 pcm, the axially averaged maximum error being reduced from 2.7 to 2.3

The distortions introduced in the axial neutron flux by the heavily rodded case, are more severe than in the rodded case A and the diffusion theory is not capable of capturing them. The NEM-Sn solver improves the accuracy of the calculation.

4.5. Summary

The computational results for this benchmark problem are summarized in Table 4.3, Table 4.4 and Table 4.5 for each of the problem configurations. In the eigenvalue error, the diffusion approximation shows about -95, -74 and -110 pcm errors for the unrodded, rodded configuration A and B, respectively. These eigenvalue errors decrease to about -40, -11 and -12 pcm by using the NEM-Sn solver. In the unrodded and rodded A configurations, the introduction of S4 instead of a diffusion approximation has a trivial effect on the pin power distribution. However, in the rodded configuration B where the control rods are heavily inserted and a large error is shown for the diffusion approximation, the introduction of the S4 approximation is required.

The implementation of the sub-plane scheme in DeCART also helped reduce the nodal error and keep the axial MOC mesh coarse which made it possible to reduce the computational cost of the 3-D calculations.

5. Application: Full core Reactivity Initiated Accident Calculation.

The overarching goal of the dissertation is to perform a full core transient analysis of a realistic RIA with the DeCART code and to compare its results with those obtained by the multi-step methodology to evaluate the benefits of the higher fidelity of the DeCART formulation. The multi-step methodology is represented by the U.S. NRC core simulator, PARCS.

The chapter is divided in three sections. In the first section, the handling of the thermal hydraulic feedbacks in DeCART during transient calculations is discussed. The second part is dedicated to the multi-steps methodology, its general approach to perform transient calculations and its main approximations. Finally, in the third part, a full core RIA is presented and its analysis with DeCART and PARCS summarized.

5.1. DeCART Transient Calculation with Thermal Hydraulic Feedbacks

In this section, the methodology in DeCART to handle time dependent thermal hydraulic feedback is discussed. One of the major contributions of the dissertation was to properly account for the time-dependent fuel and moderator temperatures as well as the moderator density provided by the thermal hydraulic solver. First, the theory involved in the subgroup methodology to deal with non uniform temperature field is reviewed. Then the new DeCART transient calculation flow is presented.

5.1.1. Uniform fuel temperature case

The spatial and energy self shielding treatment in DeCART, through the subgroup method, has been described in details in Chapter 2. However, the temperature treatment has not being addressed yet. Recall from the Chapter 2, the macroscopic absorption cross section is obtained as follow:

$$\Sigma_a = \frac{\sum_n w_n(T) \frac{\Sigma_{an}\Sigma_{bn}}{\Sigma_{an}+\Sigma_{bn}}}{1 - \sum_n w_n(T) \frac{\Sigma_{an}}{\Sigma_{an}+\Sigma_{bn}}} \qquad \text{Eq. 5.1}$$

With

$$\Sigma_{an} = N\sigma_{an}$$
$$\Sigma_{bn} = N\sigma_{bn} = \lambda N\sigma_p + \Sigma_e(\sigma_{an}) \qquad \text{Eq. 5.2}$$

σ_{an} represents the subgroup level of absorption n, and σ_{bn}, its associated background cross section. In DeCART, sets of σ_{an} and w_n for each isotope are available for five different temperatures. However, the same σ_{an} are used for all temperatures so only the w_n depend on the temperature through a linear interpolation according to the square root of the homogeneous temperature T.

5.1.2. *Non Uniform temperature treatment*

As already described in Chapter 2, the equivalence cross section, Σ_e, is determined by a set of fixed source transport calculations for fixed level of absorption σ_m

$$\hat{\Omega}_n \cdot \nabla \varphi_n(\vec{r}) + \left(N(\vec{r})\sigma_m + \lambda\Sigma_p(\vec{r}) \right)\varphi_n(\vec{r}) = \frac{1}{4\pi}\lambda\Sigma_p(\vec{r}) \qquad \text{Eq. 5.3}$$

The equivalence cross section is a function of its resulting heterogeneous fluxes ϕ_g as seen in Eq. 5.4.

$$\Sigma_e(\sigma_m) = \frac{\phi_g}{1-\phi_g}N\sigma_m - \lambda_g\Sigma_p \qquad \text{Eq. 5.4}$$

However, the use of the constant subgroup level σ_m throughout the domain becomes illogical in the non uniform temperature case. Now the cross section level must be adjusted depending on the temperature of the region. In DeCART, the temperature dependence is carried by the subgroup weight rather than by the subgroup level. It is thus not straightforward to incorporate the temperature dependence of the resonance cross section in Eq. 5.4. As an approximate measure to this problem is provided in (Joo, Beom et al. 2005). A forced subgroup level adjustment scheme is proposed to adjust the subgroup level using the ratio of the subgroup weights. Specifically, σ_m in Eq. 5.3 is replaced by the following:

$$\sigma_m(T_k) = \frac{w_n(T_k)}{w_n(T_{ref})}\sigma_m \qquad \text{Eq. 5.5}$$

where T_k and T_{ref} are the temperature of region k and the average temperature, respectively. The subgroup level is adjusted such that the product of weight and the subgroup level is preserved.

$$\Sigma_e(\sigma_m, T_k) = \frac{\phi_g}{1-\phi_g}N\frac{w_n(T_k)}{w_n(T_{ref})}\sigma_m - \lambda_g\Sigma_p \qquad \text{Eq. 5.6}$$

And the temperature effect on the macroscopic cross sections is accounted for as:

$$\Sigma_a(T_k) = \frac{\sum_n w_n(T_k)\dfrac{\Sigma_{an}\Sigma_{bn}(T_k)}{\Sigma_{an}+\Sigma_{bn}(T_k)}}{1-\sum_n w_n(T_k)\dfrac{\Sigma_{an}}{\Sigma_{an}+\Sigma_{bn}(T_k)}} \qquad \text{Eq. 5.7}$$

With

$$\Sigma_{an} = N\sigma_{an}$$
$$\Sigma_{bn}(T_k) = N\sigma_{bn}(T_k) = \lambda N\sigma_p + \Sigma_e(\sigma_{an}, T_k) \qquad \text{Eq. 5.8}$$

This process represents the detailed treatment of the temperature dependence of the macroscopic cross sections.

5.1.3. *Local temperature feedbacks in DeCART*

The typical neutronic mesh used in DeCART is shown in the Fig. 5.1. The fuel region is meshed in 24 regions, 3 rings and 8 azimuthal sectors. The cladding is divided in 8 azimuthal regions and the moderator in 2 rings for a total of 16 regions.

Because the subgroup method can handle non uniform temperature distribution, as described in the previous sections, a different temperature can be assigned to each region for which a macroscopic cross section is computed. Currently, in DeCART, two options are available. In the first one, a set of macroscopic cross sections is defined for each annular ring depicted in Fig. 5.1. The first option is the default option of the code. The second option allows evaluating cross sections for each sector of the spatial mesh described in the Fig. 5.1.
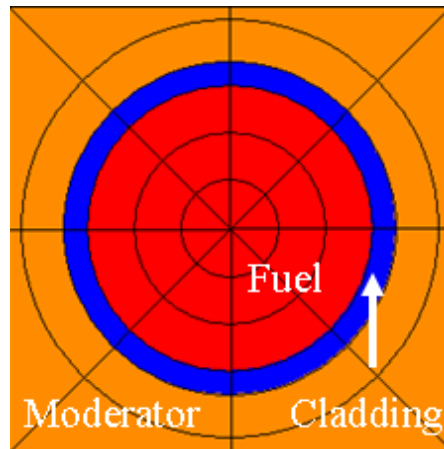
Fig. 5.1. Typical Neutronic Mesh of the DeCART code

5.1.4. *Temperature dependent macroscopic cross section for transient applications*

The approach used for steady state calculation described in the previous sections can be applied readily to transient calculations if a time dependent temperature distribution is provided to DeCART. Currently, there are two options to specify thermal hydraulic feedbacks, both for steady-state and transient applications. The first one is a solver internal to DeCART and described in the section 5.3.4 below. The second option is to use the CFD code, STAR-CD (CD-adapco 2004) to provide time dependent thermal hydraulic feedbacks. The coupling of DeCART and STAR-CD has been successfully performed for both steady state (Weber, Sofu et al. 2006) and transient (Hursin 2008) applications.

The recalculation of the equivalence cross section is needed only when the average core temperature changes significantly. It is a user defined parameter. For the RIA, since only local fuel temperatures change dramatically but not the overall core temperature, the effect on the equivalence cross sections is small and updating them is not necessary. The local temperature changes are mostly taken into account through the temperature dependent subgroup weight $w_n(T)$. The actual flow chart of a transient calculation with temperature feedbacks is shown in the Fig. 5.2.
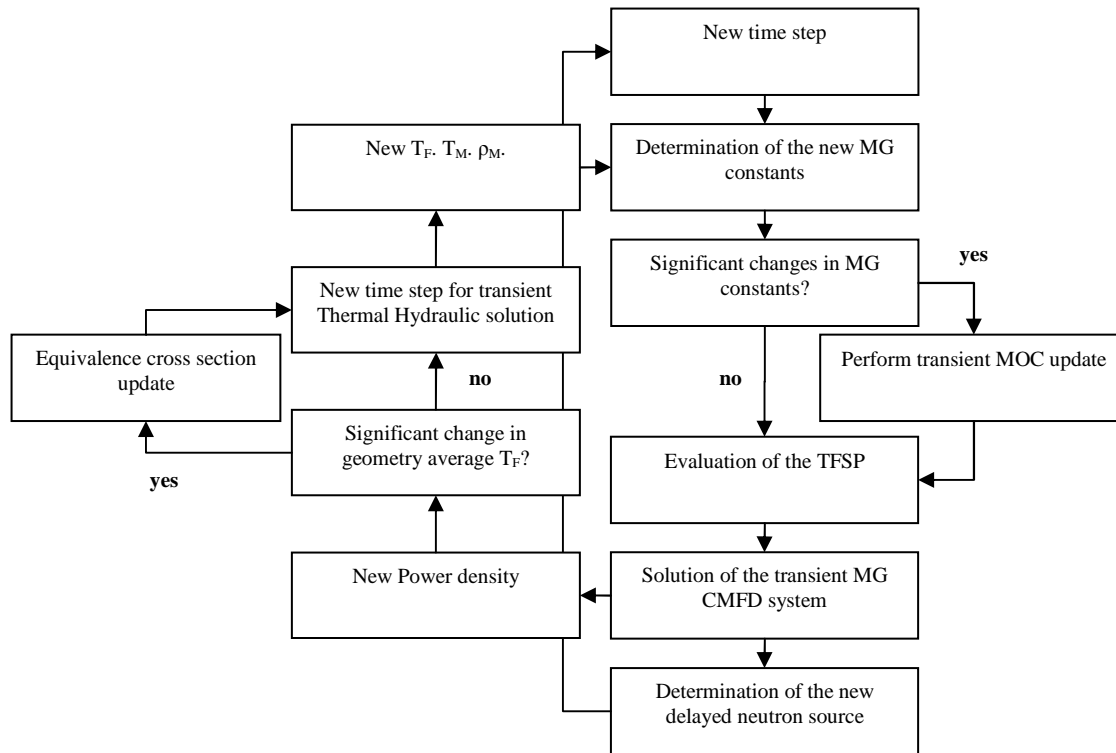
Fig. 5.2. DeCART Flow chart for transient calculation with thermal hydraulic feedbacks

5.2. Overview of the multi-step methodology

In order to understand the differences observed between PARCS and DeCART for core-wide transient calculations, and more specifically for RIA analyses, it is worthwhile to describe the multi-steps methodology in details.

5.2.1. General Approach

The neutronics analysis of a RIA transient requires a multi-steps calculation. The first step involves the generation of the homogenized cross sections by a lattice code for the range of conditions (temperatures, burnup, control rod position, etc...) anticipated during the transient. For each different state of the core, a two dimensional, single assembly transport calculation with reflective boundary condition is performed. The principle outcome of each calculation is the heterogeneous, fine energy group scalar fluxes that are used to collapse the fine energy group structure cross section library into a coarse energy group structure (usually two different neutron energies are considered) homogenized macroscopic cross sections for each fuel assembly and to generate the kinetics parameters (delayed neutron fractions, group velocities, delayed neutron decay constants). The heterogeneous surface fluxes are used to generate the assembly discontinuity factors (ADF) and the heterogeneous flux within the assembly is used to generate the form factors needed to perform the pinpower reconstruction in order to determine the fuel rod wise power distribution within the assembly.

The second step is to perform a core calculation with the standard coarse mesh nodal methods using the diffusion approximation. The geometry is homogenized at the

assembly level so that the local fuel rod information is not retained. The set of macroscopic cross sections determined during the first step is provided to the core simulator that interpolates the nuclear data (macroscopic cross sections and kinetic parameters) between all state points (temperature, burnup, etc...) to determine the nuclear data that corresponds to the local specific conditions in each node of the core during the transient. This process is illustrated in the Fig. 5.3.

The third step consists of determining fuel rod level information out of the assembly wise data coming from the second step. After the core calculation, knowledge of fuel rod information must be inferred from the assembly-wise information through some type of fuel rod reconstruction. The pinpower reconstruction is detailed in the section 5.2.2 below. It usually involves form functions which are pre-calculated at the assembly level during the lattice calculations, i.e. the first step. These forms functions do not represent exactly the conditions at the fuel rod level, especially during fast evolving transient events.
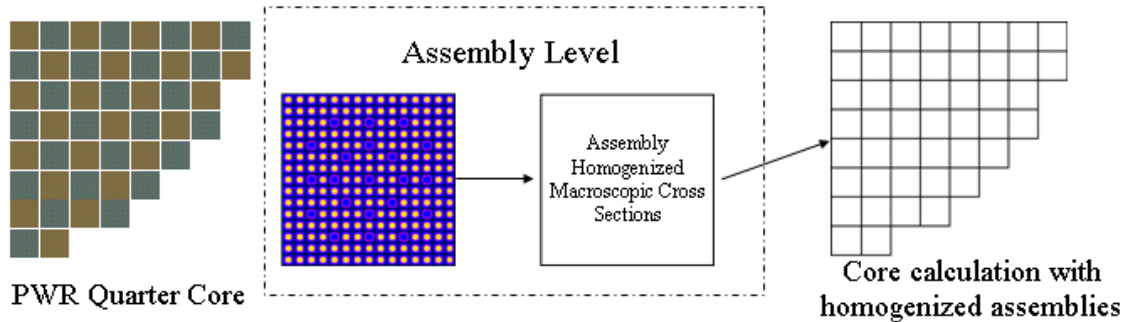
Fig. 5.3. Multi-steps methodology for core-wide transient analysis

In summary, the multi-steps methodology to analyze a RIA uses the following approximations:

- Diffusion theory.
- Coarse neutron energy discretization.
- Geometry homogenization at the assembly level.
- Fuel rod power reconstruction obtained through pre-calculated form functions obtained at the assembly level for steady state conditions.

5.2.2. *PARCS Code*

The PARCS code (Downar, Xu et al. 2006) represents the core simulator of the multi-steps methodology and performs step two and three described in the previous section. The PARCS code is used in the analyses of eigenvalue, transient and depletion problems in LWRs. As far as the dimensionality is concerned, PARCS is capable of performing calculations in any dimension, i.e., 0-D, 1- D, 2-D, and 3-D. PARCS uses the standard coarse mesh nodal methods where the geometry is homogenized at the assembly level. A library of macroscopic cross sections determined before the calculation for the anticipated range of conditions encountered is provided to PARCS, which interpolates the nuclear data between all state variables (burnup, control rod position, boron

concentration, fuel temperature, moderator temperature and density.) to determine the nuclear data that corresponds to the specific conditions in each assembly of the core during the calculation.

The PARCS spatial kinetics calculation involves the solution of the time-dependent neutron balance equations. The first step in the solution process is to discretize the balance equations in both time and space. For the temporal discretization, the theta-method with exponential transformation is employed in PARCS along with a second-order analytic precursor integration technique. The temporal discretization scheme allows sufficiently large time step sizes even in severe transients involving super-prompt critical reactivity insertion. For spatial discretization, the efficient nonlinear nodal method is employed in which the coarse mesh finite difference (CMFD) problems and the local two-node problems are repetitively solved during the course of the nonlinear iteration. The temporal and spatial differencing of the spatial kinetics equation results in a fixed source type of the problem at every time step.

The solution of a transient fixed source problem (TFSP) consists of the simultaneous solutions of the CMFD, two-node, and thermal-hydraulics problems. The CMFD problem involves a linear system with a block penta-diagonal matrix in three-dimensional problems. In PARCS, the solution of the linear system is obtained using a Krylov subspace method.

The two-node problems are solved to correct for the discretization error in the nodal interface current resulting from the finite difference approximation in a coarse mesh structure. They can be solved using any one of a number of so-called advanced nodal methods. In PARCS, the nodal expansion method (NEM) and the analytic nodal method (ANM) are used to obtain the two-node solution. Because the NEM can provide a more robust and faster solution than ANM, it has been preferred in many other reactor physics codes even though it is less accurate. However, the ANM is used as the primary nodal solver in PARCS because of the improvements which were used to produce a robust solution regardless of the nodal condition.

5.2.3. *Pinpower Reconstruction*

After the core calculation, knowledge of fuel rod power distribution must be inferred from the assembly-wise information through some type of fuel rod power reconstruction. During the second step of the multi-steps methodology, assembly averaged quantities are computed and a global coarse mesh solution is obtained, usually few energy group wise scalar fluxes.The pinpower reconstruction process is illustrated in the Fig. 5.4.

Depending on the nodal method used during the second step, NEM, ANM, or even finite difference, it is possible to reconstruct the spatial variation of the scalar flux within the node. As discussed in Chapter 2, the NEM is based on a 4th order polynomial expansion of the scalar flux, as shown in the Eq. 5.9.

$$\phi(u) \cong \sum_{i=0}^{4} \phi_i f_i(u) \qquad \text{Eq. 5.9}$$

Given its flux moments, ϕ_i, by product of the core calculation, it is possible to get information about the local scalar flux, $\phi(x, y, z)$. However, the flux distribution $\phi(x, y, z)$ is merely a shape and does not take into account the local heterogeneities, guide tube, different fuel enrichments, etc…
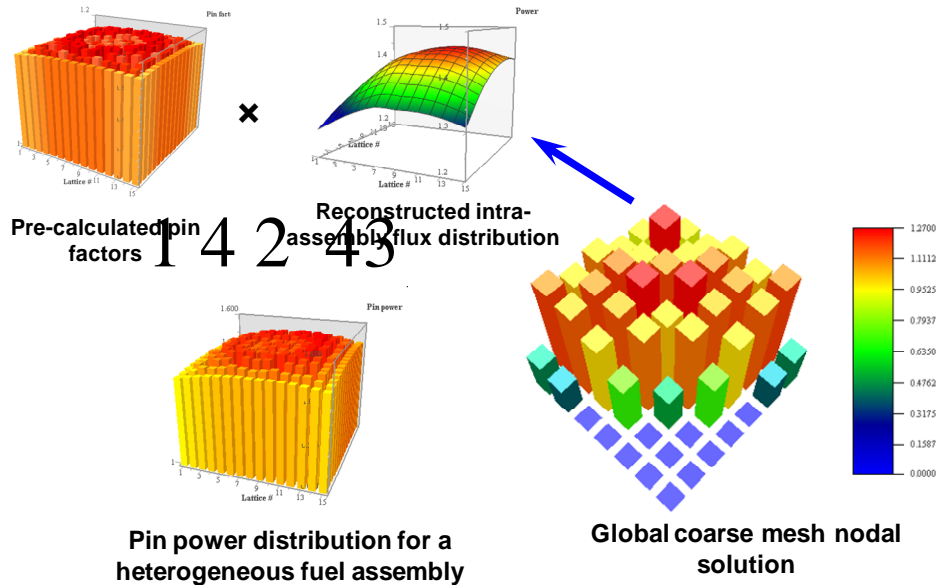
Fig. 5.4. Pinpower Reconstruction with multi-steps methodology

The effect of local heterogeneities is determined by the lattice code during the first step of the calculations. Form functions are computed assuming a flat assembly power and are superposed on the shape, $\phi(x, y, z)$ to reconstruct the local pinpower.

Even though, the form functions are generated for a wide range of thermal hydraulic and exposure conditions, they suffer from the same limitations than the macroscopic cross sections, i.e. their generation in 2-D, at the assembly level, assuming reflective boundary conditions and an approximate axial leakage. Consequently, the pinpower reconstruction process introduces approximation in the multi-steps methodology.

5.2.4. *Handling of Thermal Hydraulic Feedbacks*

Two different treatments for treating thermal hydraulic feedback are available in PARCS and are representative of the general approach used by core simulators. Below is described the native PARCS cross section handling. A more sophisticated approach, the PARCS cross section library tool, GenPMAXS (Xu and Downar 2005) was used for the calculation reported here, but fundamentally, both approaches are similar. The native treatment is interesting to understand the basics of how the cross sections are handled in a core simulator and how it differs from the DeCART treatment.

The first parameter treated is the local burnup of the fuel. In PARCS, only node wise macroscopic cross sections obtained for the node wise burnup distribution at the burnup state point of interest are necessary. The macroscopic cross sections are

functionalized on state parameters such as coolant density and boron concentration to incorporate the feedback and/or boron effects.

A set of base macroscopic cross sections are generated during the first step of the calculation, at a reference set of thermal hydraulic conditions, referred to as 0 in the Eq. 5.10. The macroscopic cross sections are assigned to each composition and four sets of partial (derivative) cross sections are also provided from the first calculation step, at the reference conditions to describe the boron and the T-H feedback effects. The thermal hydraulic effects considered are Doppler temperature T_F, moderator temperature T_M and moderator density ρ_M. The four partial group constant sets are used in the following way based on the assumption of linear variation of cross section over the state variables:

$$
\begin{aligned}
\Sigma\left(B, T_F, T_M, \rho_M\right) = \Sigma_0 + \left.\frac{\partial \Sigma}{\partial B}\right|_0 \left(B - B_0\right) + \left.\frac{\partial \Sigma}{\partial \sqrt{T_F}}\right|_0 \left(\sqrt{T_F} - \sqrt{T_{F,0}}\right) \\
+ \left.\frac{\partial \Sigma}{\partial T_M}\right|_0 \left(T_M - T_{M,0}\right) + \left.\frac{\partial \Sigma}{\partial \rho_M}\right|_0 \left(\rho_M - \rho_{M,0}\right)
\end{aligned}
$$

Eq. 5.10

where B is the boron concentration in ppm and the Doppler temperature is defined as a weighted average as:

$$
T_F = \omega T_F^{CL} + \left(1 - \varpi\right) T_F^{PS}
$$

Eq. 5.11

with the superscripts CL and PS designating centerline and pellet surface, respectively. In the PARCS model, the effective Doppler temperature is obtained by ω equal to 0.3(Finnemann and Bauer 1994).

After the T-H effect is incorporated, the cross sections are modified to incorporate the control rod effects as follows:

$$
\Sigma\left(\xi\right) = \Sigma_{UR} + \alpha \xi \Delta \Sigma_c
$$

Eq. 5.12

Where ξ is the nodal volume fraction of control rod, α is the flux weighting factor that accounts for the local flux depression in the control rod region, and Σ_c is the cross section change due to the control rod when it is fully inserted into the node and is given as a composition dependent input.

In terms of RIA analysis, the main difference between PARCS and DeCART is the way Doppler feedbacks are treated. As stated in section 5.1.3, local fuel temperatures are provided locally in DeCART and taken into account through changes in the subgroup parameters. In PARCS, a node averaged effective Doppler temperature, as defined in Eq. 5.11, is provided from the thermal hydraulic solver. This represents one of the most important differences between PARCS and DeCART in terms of RIA modeling.

75

5.3. Full Core PWR Model

5.3.1. PWR core model description

Assembly Layout

1/8th Core CR and Load Pattern For Typical 4-Loop PWR
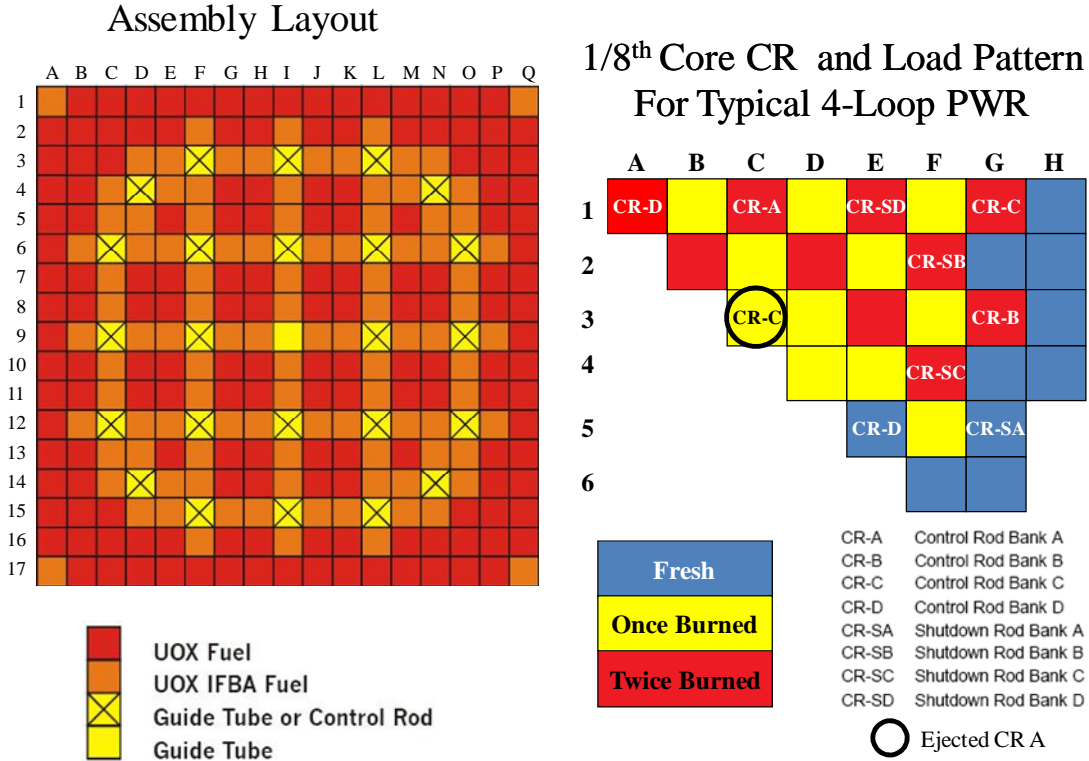
Fig. 5.5. Assembly and core layout for the 1/8th PWR core model

The model used in the RIA analysis was based on a typical 4-loop Westinghouse PWR. The core is a 3 batch core consisting of 193 fuel assemblies. Symmetric 1/8th core loading was assumed in order to minimize the computational burden. The core model used by PARCS and DeCART is shown in the Fig. 5.5 which also shows the position of the shutdown and control rod banks. The circle in Fig. 5.5 represents the control rod assembly that is to be ejected during the RIA analysis. The core design specifications are summarized in the Table 5.2. The PWR assembly uses the standard Westinghouse integrated fuel burnable absorber (IFBA) pins around each of the guide tubes. Three unique pin cell geometries are used to describe a normal fuel pin, an IFBA fuel pin, and a guide tube, as shown in Fig. 5.6. Their geometrical specifications are provided in the Table 5.1. An axially uniform U-235 enrichment of 4.2% is used for the fuel and all the fuel pins and IFBA fuel pins have the same enrichment.

The core geometry is divided into 22 axial planes of equal thickness (18.288 cm), for a total core height of about 402 cm. The active fuel height is spanned by 20 axial segments for a total length of 366 cm. The fuel is surrounded on the top and bottom by an axial water reflector. The radial discretization in the DeCART code, within each fuel rod and guide tube is shown previously in Fig. 5.1. For PARCS, the radial discretization consists of each fuel assembly being divided into four equal area nodes.

76

Table 5.1. Geometry Specifications [cm]

Pin Type	P	r1	r2	r3	t
	Fuel Pin Pitch	Fuel Pellet Outer radius	Clad Outer Radius	IFBA Layer Outer Radius	Cladding Thickness
Fuel Pin	1.26	0.3951	0.4583	---	0.0573
IFBA Pin	1.26	0.3951	0.4583	0.3991	0.0573
Guide Tube	1.26	---	0.6032	---	0.0408

Table 5.2. Core Parameters Specifications

Parameter	Value
Number of Fuel Assemblies	193
Pin Pitch [cm]	1.26
Assembly Pitch [cm]	21.42
Active Core Height [cm]	365.76
Baffle Thickness [cm]	2.52
Nominal Power [MWth]	3565
System Pressure [MPa]	15.5
Inlet Temperature [°C]	286.85
Core Flow Rate [kg/s]	15849.4
Cycle Length [EFPD]	352.95

a) Fuel Rod Geometry   b) IFBA Fuel Rod Geometry   c) Guide Tube Geometry
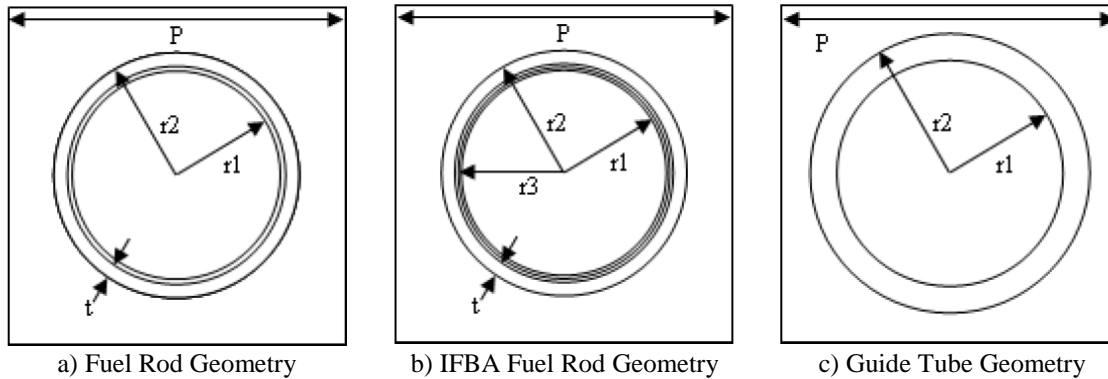
Fig. 5.6. Geometry Description of the components of a PWR assembly

Prior to describing the core loading pattern and the method used to determine the equilibrium core composition, it is worthwhile to examine the computational requirements of a 1/8th core steady state calculation with DeCART. The data described below was previously reported by (Kochunas 2008). The computational requirements of a 3-D problem in DeCART are reduced by using planar decomposition and solving each plane on a separate processor. However, the data for each plane problem must be contained on each parallel process for a 3-D calculation. The modeling requirements necessary for performing a 1/8th core calculation are shown in Table 5.3, with most of

the information being provided on a per plane basis. Note, for a quarter-core these values roughly double, and for a full core model with no symmetry the requirements would be approximately 8 times what is shown in the Table. The 3-D calculations that were performed were executed on the RESERV cluster at ANL which has 100 nodes each with 2 GB of memory and a 3.4 GHz Intel Pentium 4 processors. The calculations used 22 processors (one for each plane in the model).

Table 5.3. Computational requirements for 1/8th Core Model

Parameter	Value
Number of Energy Groups	47
Number of Axial Planes	22
Flat Source Regions per plane	~461,000
CMFD Nodes per plane	18,207
Depletable Regions per plane	15,000-20,000
Rays per plane	~32,000
Ray segments per plane	~16,000,000
Isotopes tracked per region	510
Memory Required per plane	~1.6 GB
Execution time	88h
CPU time	1936

5.3.2. *Generation of an equilibrium core composition*

In order to generate a realistic fuel composition for the once and twice burned assemblies of the model, an equilibrium core composition calculation was performed with DeCART prior to the transient calculations. The primary outcome of this calculation was the isotopic compositions of each intrapin flat source region of the 1/8th core model as well as a 3D assembly averaged exposure map which is used as input by PARCS.

5.3.2.1. *Methodology*

An equilibrium core calculation scheme with DeCART was developed by (Kochunas 2008). The objective was to determine the unique equilibrium composition corresponding to a specified fuel loading and fuel shuffling pattern. The algorithm implemented in DeCART uses a sequence of repetitive cycle depletions with the same fuel shuffling pattern until convergence of the fuel rod power prediction, i.e. the fuel rod power prediction from one cycle to the next is less than a user specified convergence criteria (10^{-2} was used in the search here).

The loading pattern and shuffling scheme used in the present study are shown in Fig. 5.7. The latter indicates the path along which the assembly will be shuffled during its life in the core and the number indicates its present cycle of residence in the core (e.g. 1 is the first cycle in residence and 3 is the third cycle in residence). The initial guess was determined from a single 3-D assembly depletion with radially reflective boundary condition and a void boundary condition on the top and bottom of the core.

A2^k	P$_a$2^k	B3^k	P$_b$2^k	P$_b$3^k	B2^k	P$_a$3^k	B1^k
A3^k	L2^k	D3^k	D2^k	F3^k	L1^k	J1^k
Q2^k	H2^k	H3^k	O2^k	O3^k	F1^k
Q3^k	F2^k	L3^k	H1^k	D1^k
Q1^k	J2^k	O1^k
A1^k	P1^k

**EOC Compositions
of Iteration k**

→ **Shuffle**

A1^k	P1^k	B2^k	P1^k	P$_b$2^k	B1^k	P$_a$2^k	Fresh
A2^k	L1^k	D2^k	D1^k	F2^k	Fresh	Fresh
Q1^k	H1^k	H2^k	O1^k	O2^k	Fresh
Q2^k	F1^k	L2^k	Fresh	Fresh
Fresh	J1^k	Fresh
Fresh	Fresh

**BOC Compositions
of Iteration $k+1$**

↙ **Deplete**

A2^{k+1}	P$_a$2^{k+1}	B3^{k+1}	P$_b$2^{k+1}	P$_b$3^{k+1}	B2^{k+1}	P$_a$3^{k+1}	B1^{k+1}
A3^{k+1}	L2^{k+1}	D3^{k+1}	D2^{k+1}	F3^{k+1}	L1^{k+1}	J1^{k+1}
Q2^{k+1}	H2^{k+1}	H3^k	O2^{k+1}	O3^{k+1}	F1^{k+1}
Q3^{k+1}	F2^{k+1}	L3^{k+1}	H1^{k+1}	D1^{k+1}
Q1^{k+1}	J2^{k1+}	O1^{k+1}
A1^{k+1}	P1^{k+1}

**EOC Compositions
of Iteration $k+1$**

Fig. 5.7. Loading pattern and shuffling scheme for the PWR 1/8th core model

For the loading pattern shown here, the fresh assemblies are on the periphery to limit the pinpower peaking at the center of the core; the once and twice burned assemblies are arranged in a checkerboard elsewhere in the core. It should be noted that no optimization was performed in the design of the loading pattern. It was simply chosen arbitrarily to be a realistic representative example since actual designs are typically proprietary.

The primary outcome of the equilibrium core composition calculation is the local fuel composition for the burned assemblies in DeCART as well as a 3-D exposure map which is used in PARCS. As noted earlier, the emphasis was to insure consistency between the burnup data used PARCS and DeCART.

5.3.2.2. Results

An important quantity that will be presented extensively during the next few sections is the relative difference of a certain quantity Q between DeCART and PARCS. The relative difference R in terms of Q is given in equation 5.13:

$$R = \frac{Q_{DeCART} - Q_{PARCS}}{Q_{DeCART}} \times 100$$

Eq. 5.13

Every time a relative difference is reported, the definition of Equation 5.13 is used in which the relative difference is expressed in %.

5.3.2.2.1. Convergence

The convergence behavior of the equilibrium Beginning of Cycle (BOC) power distributions is first described for the given core design. The local maximum absolute and relative differences of the relative pin power distribution in the entire core and also the percent RMS of the relative differences is shown in Fig. 5.8. These differences are calculated from the solutions of successive iterations.

The convergence criterion chosen for the equilibrium core was an RMS less than 1% because this equates to a maximum local relative difference in pin power of less than 0.1% and an absolute difference in the relative pin powers of less than 0.01. These differences in the relative pin power distribution are generally considered small for most code to code comparisons, and given the nature of the computation time of these calculations this level of error in the solution was deemed acceptable. The total computation time of the 3-D equilibrium core calculation was about 22 days.
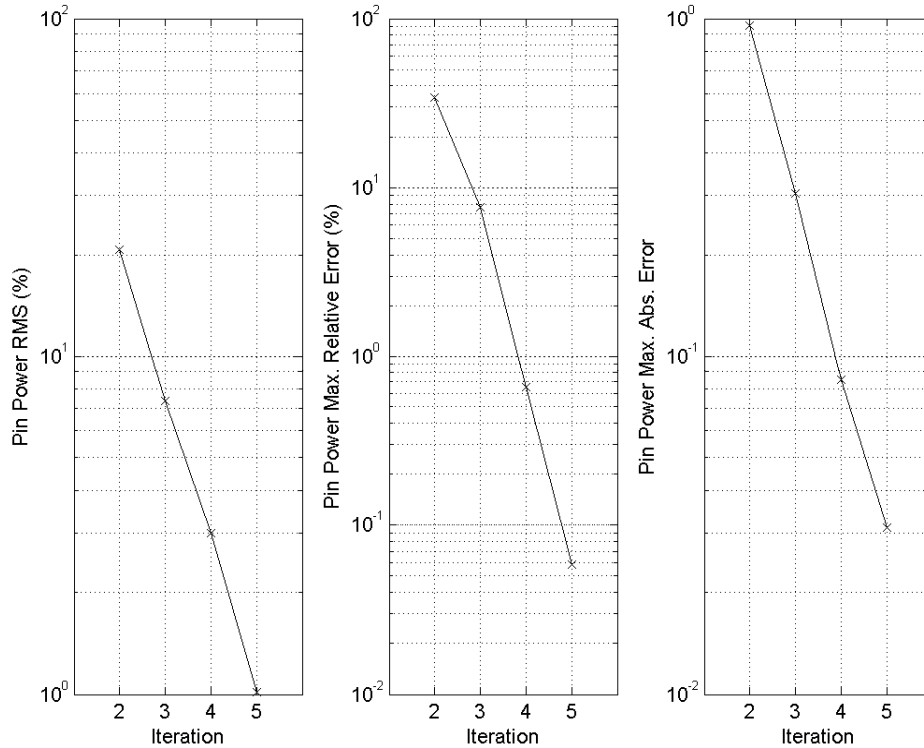
Fig. 5.8. Equilibrium calculation convergence behavior
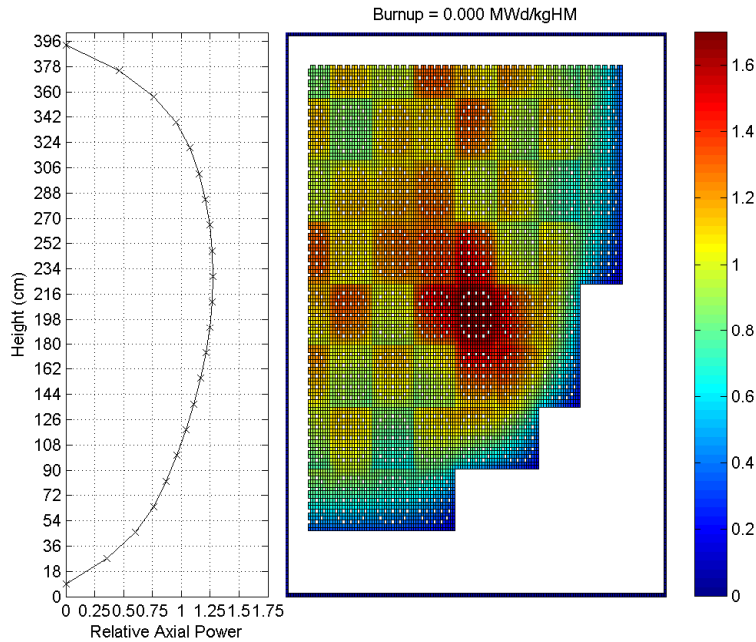
Fig. 5.9. BOC core power distributions - axial power variation and axially integrated radial variation -
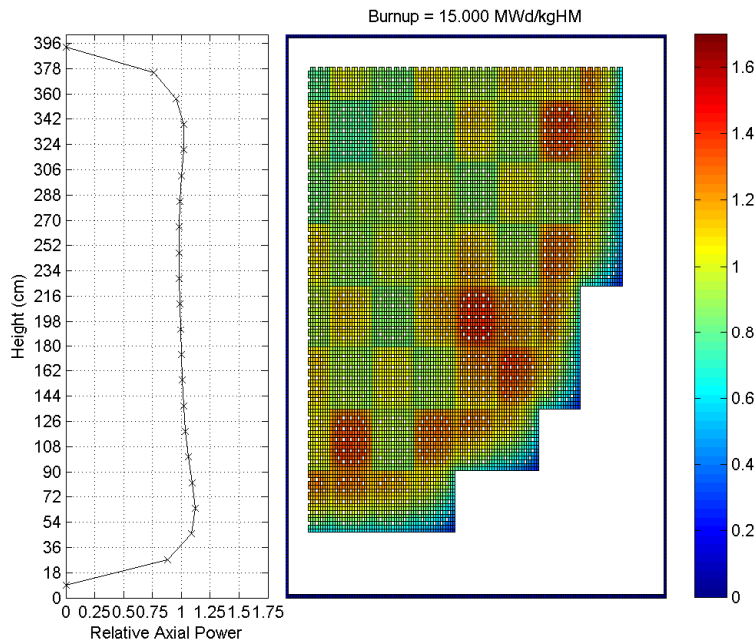
Fig. 5.10. EOC core power distributions - axial power variation and axially integrated radial variation -

5.3.2.2.2. Equilibrium core power distribution

In this section the evolution of the power distributions and peaking factors during the reactor cycle are examined. Fig. 5.9 and Fig. 5.10 show the radially integrated axial power shape and axially integrated radial assembly power distribution for the 1/8th core

at the BOC and End of Cycle (EOC), respectively. DeCART provides this level of detail without having to use homogenization or de-homogenization (pin power reconstruction) techniques such as used in PARCS and other industry standard core simulators.

It is worth noting that the radial power distributions in the previous figures are somewhat atypical since there is high peaking in an assembly close to the periphery of the core. As noted earlier, because of the computational burden in the DeCART calculation, no attempt was made to optimize the loading pattern to reduce this peaking. However, even though this result makes the reactor model less realistic, it does not detract from the primary goal of this study which is to perform a code-to-code comparison of current industry standard and higher fidelity methods.
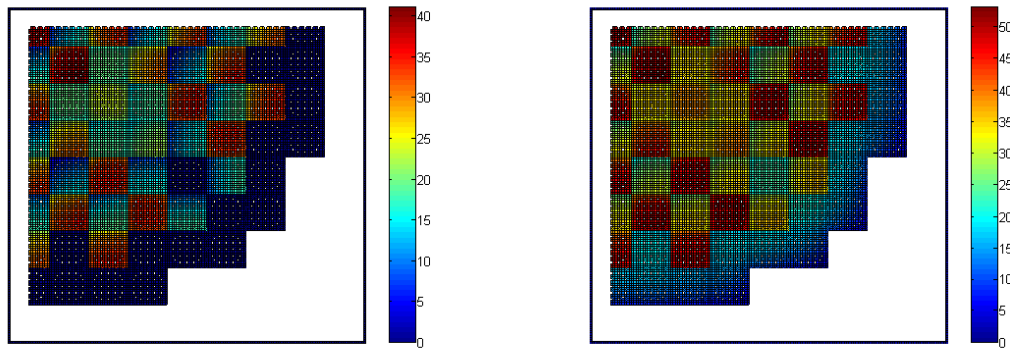
<table>
<tr><td>a) BOC burnup map [MWd/kgHM]</td><td>b) EOC burnup map [MWd/kgHM]</td></tr>
</table>

Fig. 5.11. Axially integrated exposure map at BOC and EOC

As shown in Fig. 5.10, the axially integrated radial pinpower distribution tends to flatten during the cycle and the power peaks tends to migrate closer to the periphery of the core. The current methodology used in codes such as PARCS typically has difficulty correctly describing the spatial variation of the pin power during depletion. The evolution of the axial power variation is typical of a PWR, with a relatively flat axial shape becoming "double-peaked" at the end of the cycle. The central deep in the axial power shape is due to higher burnup at the early part of the fuel residence in the core. Finally, a quantity of particular interest throughout the equilibrium core calculation is the burnup distribution. Fig. 5.11 shows the fuel rod axially integrated radial burnup distribution at the beginning and end of reactor cycle. One of the particular advantages of higher fidelity methods such as DeCART is to provide the detailed evolution of the exposure within fuel pins in the assembly. The once burned fuel assemblies show especially strong spatial exposure gradients with the maximum exposure at BOC of about 41 MWd/kgHM and 53 MWd/kgHM at EOC. At the end of the equilibrium cycle calculation, the DeCART output is processed with a MATLAB script to generate a 3D exposure map at the assembly level for the BOC and EOC. This provides PARCS with exposure data that is consistent with DeCART and insures consistency in the initial conditions for the transient calculations.

5.3.3. *Cross Sections and Kinetic Parameters Generation for PARCS*

In order to assure consistency in the nuclear data between PARCS and DeCART, it is desirable to use DeCART as a lattice code to generate the kinetic parameters and homogenized cross sections for PARCS. Part of the dissertation work involved the development of a lattice calculation capability in DeCART as well as an interface with the PARCS cross section library tool, GenPMAXS. The following sections described how the homogenisation and condensation processes required to generate the macroscopic cross sections library for PARCS are performed.

5.3.3.1. *Generation of the Homogeneous Parameters*

To generate a few group macroscopic cross sections, 2 steps are required. The first step is a homogenization step, where the spatial dependence of the cross section is integrated over an assembly in order to obtain an assembly-wise cross section. The fine energy group structure is retained. The cross section is given by a flux-volume weighted average as seen in the Eq. 5.14, in order to preserve the reaction rates over a given assembly.

$$\Sigma_x^g = \frac{\displaystyle\sum_{k \in Assembly} \Sigma_{x,k}^g \phi_k^g V_k}{\displaystyle\sum_{k \in Assembly} \phi_k^g V_k} \qquad \text{Eq. 5.14}$$

The second step is a condensation step to reduce the fine energy group structure to a coarse one, involving typically few energy groups. In the considered model, two coarse energy group are used. The goal is to take into account the energy dependence of the cross section. The energy cut-off is set to 3.9eV. Similarly to the homogenization step, the macroscopic cross section is obtained by a flux-volume weighted average, the flux being the assembly averaged flux.

The previous 2-steps process is valid for the following macroscopic cross sections: absorption, total, transport, fission, υ times fission, kappa times fission and scattering matrix. Chi and the diffusion coefficient treatment remain to be determined.

Chi is obtained in a similar fashion than the previous macroscopic cross sections, the only difference being that the average is a fission-volume weighted average instead of a flux-volume weighted average as seen in the Eq. 5.14.

$$\chi_G = \frac{\displaystyle\sum_{k \in Assembly} \chi_G \left(\sum_{g'=1, N_{group}} \nu \Sigma_{f,k}^{g'} \phi_k^{g'} V_k \right)}{\displaystyle\sum_{k \in Assembly} \left(\sum_{g'=1, N_{group}} \nu \Sigma_{f,k}^{g'} \phi_k^{g'} V_k \right)} \quad \& \quad \chi_G = \sum_{g' \in G} \chi_{g'} \qquad \text{Eq. 5.15}$$

The diffusion coefficient is the most complex macroscopic cross sections to obtain since preserving the reaction rates as it is done for the other quantities, doesn't produce accurate results. The common approach to generate diffusion coefficients is

through critical spectrum calculation, the diffusion coefficient being a byproduct of such a calculation.

5.3.3.2. *Critical Spectrum Calculation*

The critical spectrum calculation is needed in a lattice code in order to correct the fact that the lattice calculation is performed at the assembly level, in 2-D, with reflective boundary condition. The spectrum then corresponds to an infinite medium case that may be significantly different from the local spectrum inside a reactor because of the inter assembly leakage.

The critical spectrum is obtained by solving the B1 equation (Stamm'Ler and Abbate 1983). A B1 equation solver has been implemented in DeCART. The main outcome of such a solver is a 0-D critical spectrum with a fine energy group structure and a critical buckling value. The assembly averaged diffusion coefficient is then defined by Eq. 5.16:

$$D_g = \frac{|J_g|}{|B_{crit}|\phi^g}$$

Eq. 5.16

With J_g the net current, ϕ^g the fine energy group structure critical flux and B_{crit}, the critical buckling.

In order to obtain the coarse group diffusion coefficient, a condensation step is required, and the same flux weighted average is used. In section 5.3.3.1, the generation of the macroscopic cross sections needed by PARCS has been performed by homogenization and condensation using the infinite spectrum flux. In order to take into account the leakage in the lattice calculation, it is possible to homogenize and condense the microscopic cross sections using the critical spectrum flux instead of the infinite one. Since the critical flux is a 0-D flux and that some spatial variation of the flux is needed especially in the homogenization step, the region-wise, fine energy group structure scalar flux is obtained from the infinite one using Eq. 5.17.

$$\phi_{k,crit}^g = \frac{\phi_{k,crit}^g\left(B_{crit}^2\right)}{\phi_{k,crit}^g(0)}\phi_{k,\infty}^g$$

Eq. 5.17

$\phi_{k,crit}^g$ and $\phi_{k,\infty}^g$ are the region-wise, fine energy group structure critical and infinite spectrum scalar flux, respectively. $\phi_{k,crit}^g\left(B_{crit}^2\right)$ is the critical spectrum flux corresponding to the critical buckling and $\phi_{k,crit}^g(0)$ is the critical spectrum flux corresponding to 0 buckling.

5.3.3.3. *Kinetic Parameters*

The remaining information to be generated by a lattice code is the kinetic parameters, i.e. the neutron velocities and the delayed neutron fractions. Those quantities were already defined in Chapter 2. The generation of the assembly-wise data used by PARCS is described below.

In order to generate few group velocities, the homogenization and condensation processes described in section 5.3.3.1 are used. The generation of the delayed neutron fraction for a coarse energy group structure and homogenized geometry is difficult. In order to take into account delayed neutron leakage and their energy dependence, a complex treatment needs to be added to the usual the isotopic fission source weighting presented in Chapter 2. Weighting the physical delayed neutron fraction by the importance function, i.e. the adjoint of the infinite spectrum, region-wise, fine energy group structure scalar flux, as is shown in Eq. 5.18, takes the energy dependence as well as the spatial variation of the flux within the assembly into account. However, the inter-assembly leakage is not factored in, since the lattice calculation is performed at the assembly level with reflective boundary condition.

$$\beta_k^{\%eff} = \frac{\displaystyle\sum_{m\in Assembly}\left(\sum_{g'}^{G}\chi_{dkg'}\phi_{m,g'}^{*}\sum_{i=1}^{I^m}\sum_{j=1}^{J^m}\beta_k^{j}\left(\sum_{g=1}^{G}\nu\sigma_{fg}^{m,i,j}N_j^{m,i}\phi_g^{m,i}\right)V^{m,i}\right)}{\displaystyle\sum_{m\in Assembly}\left(\sum_{g'}^{G}\chi_{g'}\phi_{m,g'}^{*}\sum_{i=1}^{I^m}\sum_{j=1}^{J^m}\left(\sum_{g=1}^{G}\nu\sigma_{fg}^{m,i,j}N_j^{m,i}\phi_g^{m,i}\right)V^{m,i}\right)}$$

Eq. 5.18

Where $\phi_g^{m,i}$ and $\phi_{m,g}^{*}$ are the region-wise, fine energy group structure, infinite spectrum fluxes and its adjoint. In order to take into account the inter- assembly leakage, the energy dependence of the delayed neutron, and to use the critical flux instead of the infinite one, the following averaging formula (Eq. 5.19) is used to determine the effective delayed neutron fraction:

$$\beta_k^{\%eff} = \frac{\displaystyle\sum_{m\in Assembly}\left(\sum_{g'}^{G}\chi_{dkg'}\phi_{g'}^{*}\left(B_{cr}^2\right)\sum_{i=1}^{I^m}\sum_{j=1}^{J^m}\beta_k^{j}\left(\sum_{g=1}^{G}\nu\sigma_{fg}^{m,i,j}N_j^{m,i}\phi_g^{m,i}\right)V^{m,i}\right)}{\displaystyle\sum_{m\in Assembly}\left(\sum_{g'}^{G}\chi_{g'}\phi_{g'}^{*}\left(B_{cr}^2\right)\sum_{i=1}^{I^m}\sum_{j=1}^{J^m}\left(\sum_{g=1}^{G}\nu\sigma_{fg}^{m,i,j}N_j^{m,i}\phi_g^{m,i}\right)V^{m,i}\right)}$$

Eq. 5.19

Where $\phi_g^{m,i}$ is the region-wise, fine energy group structure, infinite spectrum fluxes and $\phi_{m,g}^{*}\left(B_{cr}^2\right)$ the adjoint to the fine energy group structure critical spectrum flux.

In order to compute the latter quantity, a module has been added to the DeCART code to calculate the adjoint of the critical spectrum flux. The DeCART has been developed to be able to perform all the needed functions to generate the macroscopic cross sections and kinetic parameters needed by a core simulator, i.e. by PARCS, to run any kind of steady-state or transient calculation. Finally, an interface has been developed between GenPMAXS and DeCART to streamline the process of generating cross sections library for PARCS with DeCART.

5.3.3.4.   *Branch Structure and Burnup Steps*

The process of generating the macroscopic cross sections library for PARCS requires a few lattice calculations for a range of conditions and burnup values representative of the conditions seen by the reactor during the analysis. For the current RIA model, 4 branches are considered:

- Control Rod
- Fuel Temperature
- Coolant Density /Moderator Temperature
- Boron Concentration

The reference case is obtained for an unrodded assembly, with a fuel temperature of 900K, a moderator temperature of 580K and a boron concentration of 1000ppm. The branch values are summarized in the Table 5.4 below.

The burnup steps considered are typical of a PWR core and are as follow: 0.2, 0.5, 1.0, 1.5, 2.0, 2.5, 3.0, 3.5, 4.0, 4.5, 5.0, 5.5, 6.0, 6.5, 7.0, 7.5, 8.0, 9.0, 10.0, 11.0, 13.5, 15.0, 16.5, 18.0, 20.0, 22.0, 25.0, 30.0, 35.0, 40.0, 45.0, 50.0 and 55.0 MWd/kgHM.

Table 5.4. DeCART lattice calculation branch structure

Branch	Low	Reference	High
Control Rod		Out	In
Fuel Temp [K]	560	900	1320
Moderator Temp [K]	560	580	600
B Concentration [ppm]	0	1000	2000

5.3.4. *Internal Thermal hydraulic solution*

In order to provide thermal hydraulic feedbacks to the neutronic solvers, a simplified one-dimensional thermal-hydraulic solver is used in both DeCART and PARCS. It solves the 1-D radial heat conduction and 1-D axial heat convection equations for steady-state and transient problems. In the heat convection solution, a one-dimensional single-phase flow model is employed under the assumption of constant pressure and boiling is not considered. Also, under the assumption of constant pressure, the momentum equation is not solved so that only mass continuity and energy conversation equations are solved in the flow problem. The constitutive relations which are required to close the field equations are provided as a form of polynomial of temperature at a given pressure. In the heat conduction solution, the radial temperature distribution within a fuel rod is solved to determine the Doppler temperature. A finite difference scheme is employed to obtain the radial temperature distribution during the transient. The axial heat conduction is neglected in the solution process since it is very small compared to the radial heat conduction. The applicability of the constitutive relations and the simplifications in flow modeling provide limitations on the application of this solver to a wider range of reactor transient conditions.

The fundamental difference between PARCS and DeCART solvers is the level at which the thermal hydraulic feedbacks are provided. In DeCART, the thermal-hydraulics equations are solved separately for each fuel rod, and provide intra pin fuel temperature. Conversely in PARCS, the thermal-hydraulics equations are solved for each fuel assembly and only an assembly averaged effective fuel temperature is used to determine the Doppler feedbacks.

The motivations behind the use of a simple thermal hydraulic feedback solver are twofold. Since the main objectives of the presented work is to evaluate the impact of the

86

neutronic approximations made by the current neutronic methodology in terms of fuel response during the RIA, it is desirable to use consistent thermal hydraulic solution for both PARCS and DeCART. Both internal solvers of DeCART and PARCS have the needed consistency.

Since the thermal hydraulic solver is based on a 1-D radial conduction solver, the temperature is averaged azimuthally. Consequently of the two options presented in section 5.1.3 above, the first one is selected: a different temperature is applied for each annular ring depicted in the Fig. 5.1.

5.3.5. *Transient model*

The transient event considered for the RIA analysis is the ejection of a control rod assembly with the reactor being in the hot zero power (HZP) conditions: the fuel and coolant temperatures are at the inlet coolant temperature, 287°C. The power generated is set to 10^{-4}% of its nominal value which are the typical conditions of a reactor in standby condition (control rods in, shutdown rods out).

The control rod assembly to be ejected is chosen in such a way that the transient is super prompt critical. The main reason for such a choice is to have a neutronic driven event; therefore a simple thermal hydraulic model is sufficient to capture the thermal hydraulic effects. Control rod cusping treatment is currently not available in DeCART. Hence, it is not possible to accurately model a control rod partially inserted within a plane. In order to avoid partially inserted control rod, the ejection time is assumed to be negligible and the rod withdrawal occurs instantaneously at time zero. The usual ejection time for a control rod assembly in a typical PWR is about 0.1s, with a transient time of about 0.5s. Consequently, an instantaneous ejection represents a significant approximation. However, since the main purpose of this work is to make a code-to-code comparison, the instantaneous ejection preserves the consistency of both DeCART and PARCS calculations.

5.4. DeCART/PARCS Comparison

In order to check the quality of the macroscopic cross sections and kinetic parameters, first steady state calculations are performed with both DeCART and PARCS. Then a RIA scenario is considered involving a control assembly near the center of the reactor.

5.4.1. *Steady State Comparison*

In order to evaluate the quality of the macroscopic cross sections and kinetic parameters generated with DeCART, steady state calculations are performed with both DeCART and PARCS. Since the RIA analysis is performed at BOC, the steady state comparison is presented for BOC conditions.

The steady state calculations were performed for the initial state of the reactor before the start of the RIA, i.e. at BOC, for hot zero power conditions. In order to obtain a realistic power distribution, the boron concentration of both DeCART and PARCS was adjusted in order to model a critical reactor. First, a steady calculation was performed with each code with all the control assemblies inserted. Then for the critical boron

concentration, the control rod assembly to be ejected during the RIA was withdrawn and the steady state eigenvalue and fuel rod relative power prediction of both DeCART and PARCS were calculated. For each steady state calculation, the effective multiplication coefficient and relative pinpower were compared and the results are summarized in Table 5.5. The axially integrated relative pinpower and the DeCART/PARCS relative difference is shown in Fig. 5.12. The axial evolution of the local relative power prediction is shown in Fig. 5.13.

The relative difference in terms of k_{eff} between DeCART and PARCS is less than 100 pcm for both the unrodded cases. The predicted amount of soluble boron necessary to achieve criticality is also very close between PARCS and DeCART, which provides confidence that the cross sections were properly generated.

Table 5.5. BOC Steady state comparison of PARCS and DeCART

Case	Multiplication Coefficient		Δk(pcm)	RMS Relative pinpower difference in %
	DeCART	PARCS		
Rods in	1.0 (946 ppm of B)	1.0 (970 ppm)	0	4.11
Rods out	1.010793	1.01179	-99	3.97

The relative difference in the axially integrated pinpower prediction is about 5% for both cases. The relative difference increases in the area of the core with sharp flux gradients, in the rodded control assemblies for example. Some differences are expected since the nuclear data (cross sections and assembly discontinuity factors) are generated at the assembly level with reflective boundary conditions which approximates the actual heterogeneous configuration in the reactor.

The rod worth for the considered RIA scenario is summarized in Table 5.6. ρ represents the total reactivity insertion in the reactor upon withdrawal of the control rod assembly. It is computed in Eq. 5.20 below. β represents the total delayed neutron fraction and ρ_1 is the reactivity expressed in \$, i.e. in fraction of β. In both cases, the control rod worth is well over a dollar of reactivity and the transient resulting from a rod ejection is super prompt critical.

$$\rho = \frac{k_{eff}^{unrodded}}{k_{eff}^{rodded}} - 1$$

Eq. 5.20

The worth predicted by PARCS is higher than the worth predicted by DeCART because of the combination of different k_{eff} and delayed neutron fractions. Consequently, different transient behaviors are expected between PARCS and DeCART.

Table 5.6. BOC Control rod worth predicted by DeCART and PARCS

	DeCART	PARCS
ρ	0.01079	0.01165
β	0.00617	0.00615
ρ [\$]	1.75	1.89
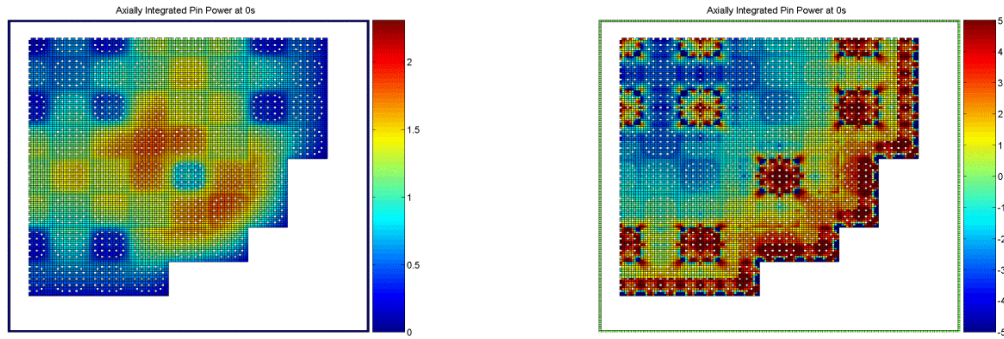
a) DeCART S.S. axially integrated fuel rod power

b) S.S. axially integrated pinpower relative difference in % between PARCS and DeCART

Fig. 5.12. BOC S.S. DeCART/PARCS axially integrated relative fuel rod power prediction for the rodded case

The control rod assembly to be withdrawn is close to the core center. In the central region of the reactor, the power predicted by DeCART is consistently lower than the power predicted by PARCS as seen in the Fig. 5.12. The worth of the control rod predicted by DeCART is then understandably lower.

The analysis of the relative difference in terms of the local fuel rod power prediction between PARCS and DeCART as shown in Fig. 5.12 and Fig. 5.13 suggests that the differences between PARCS and DeCART can be important, especially for the assemblies where the control rods are inserted. This is expected and is due to the known limitations of the multi-step methodology to accurately predict fuel rod powers in area of the reactor with sharp flux gradients. However, the biggest differences in the power predictions occur in regions of the reactor generating low power, and consequently of lower importance. Another important factor to consider is the effect of analyzing relative differences. In an area where the considered quantities are small, the relative difference tends to magnify the errors.

5.4.2. *Transient Comparison*

At BOC, a control rod assembly withdrawal is considered as shown in Fig. 5.6. During the transient analysis, the core averaged power generation is recorded as well as a comparison of the local fuel rod power. As discussed earlier, both DeCART and PARCS use similar simplified thermal hydraulic methods to simulate the fuel and moderator temperature response during the course of the transient, with the only difference being that DeCART provides temperature feedback at the fuel rod level whereas PARCS provides feedback at the assembly level.

In terms of computational cost, the memory requirements to run an eighth core transient model were similar to the one of the equilibrium core calculation discussed in Table 5.3 above. Each of the transient presented in the following sections was run on the RESERV cluster in ANL. It took approximately 5 days using 22 processors to run each transient. The PARCS transient were run on single personal computer in about one hour.

The Control assembly is ejected and the transient was run for 0.1s with a time step of 1ms. The average core power during the event obtained by each code is shown in Fig.

5.14 while the fuel rod power relative difference between DeCART and PARCS in % RMS is shown in the Fig. 5.15.
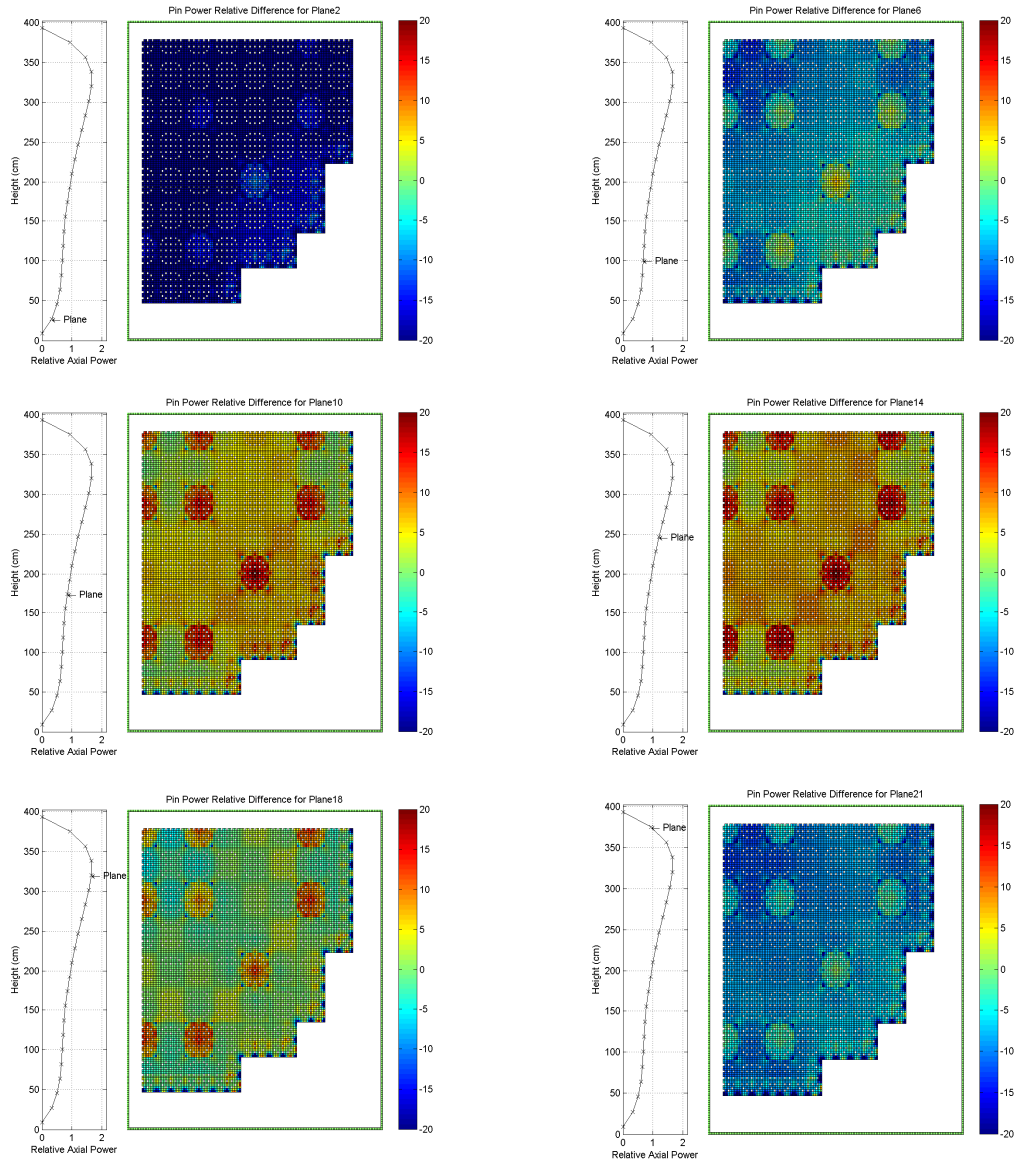
Fig. 5.13. Axial evolution of the relative fuel rod power difference between DeCART and PARCS at BOC

The predictions of core averaged power by DeCART and PARCS are significantly different. The peak power predicted by PARCS is higher by about 50% and occurs earlier in the transient. The difference in the peak power can be explained by the different rod worth predicted by the codes as shown in the Table 5.6, as well as the slightly different delayed neutron fractions. The reactivity inserted in the PARCS case is larger and the delayed neutron fraction is smaller than in the DeCART case. For the super prompt critical RIA event, the delayed neutron source of the point kinetics equation can be neglected and the point kinetics equation can be solved analytically. The principal quantities of interest, maximum power and the time at which the maximum power is reached, can be expressed as a function of the inserted reactivity, the prompt neutron life

time and the total delayed neutron fraction as shown in Eq. 5.20. This approach is referred to as the Nordheim Fuchs model which can be derived from the exact point kinetics equations. The kinetics parameters used in these relations are computed from the solution of the DeCART and PARCS spatial kinetics solutions. The details of the derivation are given in (Ott and Neuhold 1985).

$$p_m - p^0 = -\frac{\rho_{p1}^2}{2\Lambda\gamma} \quad \& \quad t_m \approx \frac{\Lambda}{\rho_{p1}} \ln\left(\frac{4p^0}{p_m}\right) \qquad \text{Eq. 5.21}$$

where ρ_{p1} is the inserted prompt reactivity in \$, Λ the neutron generation time, p^0 the initial power level and γ the feedback coefficient.
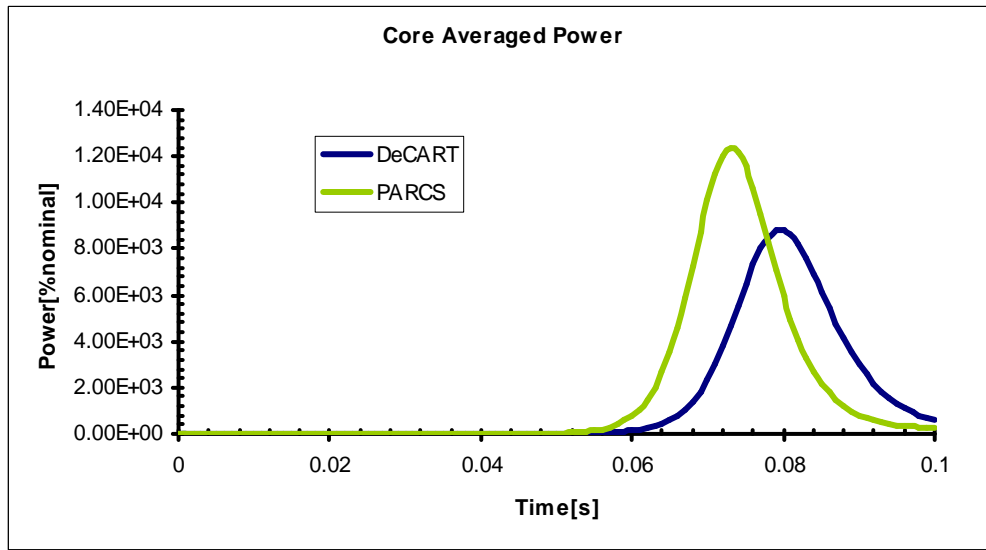
Fig. 5.14. BOC RIA scenario-DeCART/ PARCS Core average power comparison-
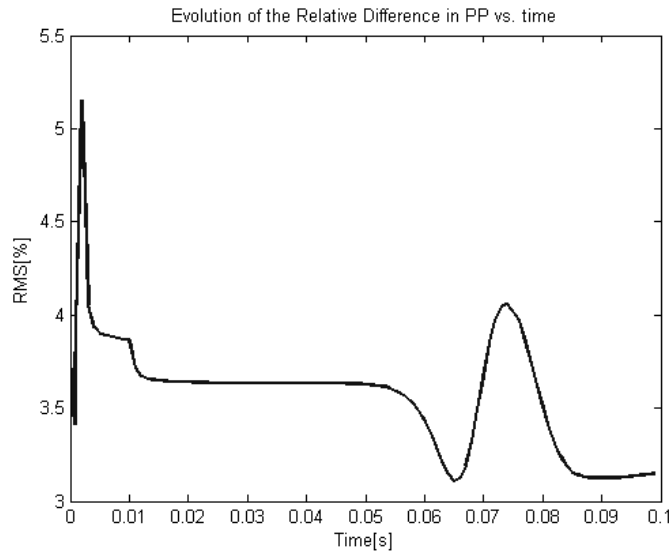
Fig. 5.15. BOC RIA scenario -DeCART/ PARCS pinpower RMS relative difference evolution with time-

Table 5.7. Nordheim Fuchs model results for BOC RIA

	Nordheim Fuchs Model		Spatial Kinetics Model	
	DeCART	PARCS	DeCART	PARCS
ρ	0.01079	0.01165	0.01079	0.01165
β	0.00617	0.00615	0.00617	0.00615
$\rho 1[\$]$	1.75	1.89	1.75	1.89
$\Lambda[s]$	1.70E-05	1.70E-05	1.70E-05	1.70E-05
$\gamma[1/fp\text{-}s]$	1.2	1.2	--	--
$p_m\text{-}p^0$	84.9	120.67	88.41	123.58
$t_m[s]$	6.91E-02	5.95E-02	8.00E-02	7.30E-02

The comparison of the Nordheim Fuchs model results with the spatial kinetic results of PARCS and DeCART, for the principal quantities of interest is summarized in the

Table 5.7. Since the prompt neutron lifetime and the total delayed neutron fraction in PARCS and DeCART are different, two results are provided for the Nordheim Fuchs model, one using the DeCART parameters and the other consistent with the PARCS parameters. The Nordheim Fuchs model predicts very accurately the maximum power seen by the core during the transient as well as the time at which it happens which provides confidence that the differences observed between PARCS and DeCART come from steady state differences. The effective generation time is obtained similarly to the effective delayed neutron fraction as shown in Eq. 5.22 and is computed by PARCS and DeCART.

$$\Lambda = \frac{\displaystyle\sum_{m \in Assembly} \phi_g^{m,*} \frac{\phi_g^m}{v}}{\displaystyle\sum_{m \in Assembly} \phi_g^{m,*} \chi_g \sum_{g'}^{G} \upsilon\Sigma_{f,g}^m \phi_{g'}^m} \qquad \text{Eq. 5.22}$$

As for the pinpower prediction, the overall conclusions are similar to the conclusions made during the steady state comparison. The variation of the %RMS relative difference in the time between 0.05s and 0.09s can be attributed to the differences of core averaged power during that time span. The PARCS overall power increases earlier and the temperature rise tends to flatten the shape of the fuel rod power distribution. Conversely in the DeCART prediction, the fuel temperature hasn't yet changed and the fuel rod power shape is still very similar to the initial shape causing the overall %RMS relative difference to increase. Later in the transient, the fuel temperature in the DeCART model increases reducing the relative %RMS difference. The %RMS difference after both the PARCS and DeCART power peaks is different from the initial difference since the temperature has been increased to compensate for the reactivity introduced by the withdrawal of the control rod which results in a transient fuel rod power shape different from the steady state shape.

In terms of accident analysis, the quantity of interest is the local fuel rod power during the transient. Fig. 5.16 shows the evolution of the core-wide fuel rod power distribution and the relative difference between PARCS and DeCART for the axial

segment of the core where the maximum power in the steady state occurs, i.e. at an axial position of about 340cm from the bottom of the core.
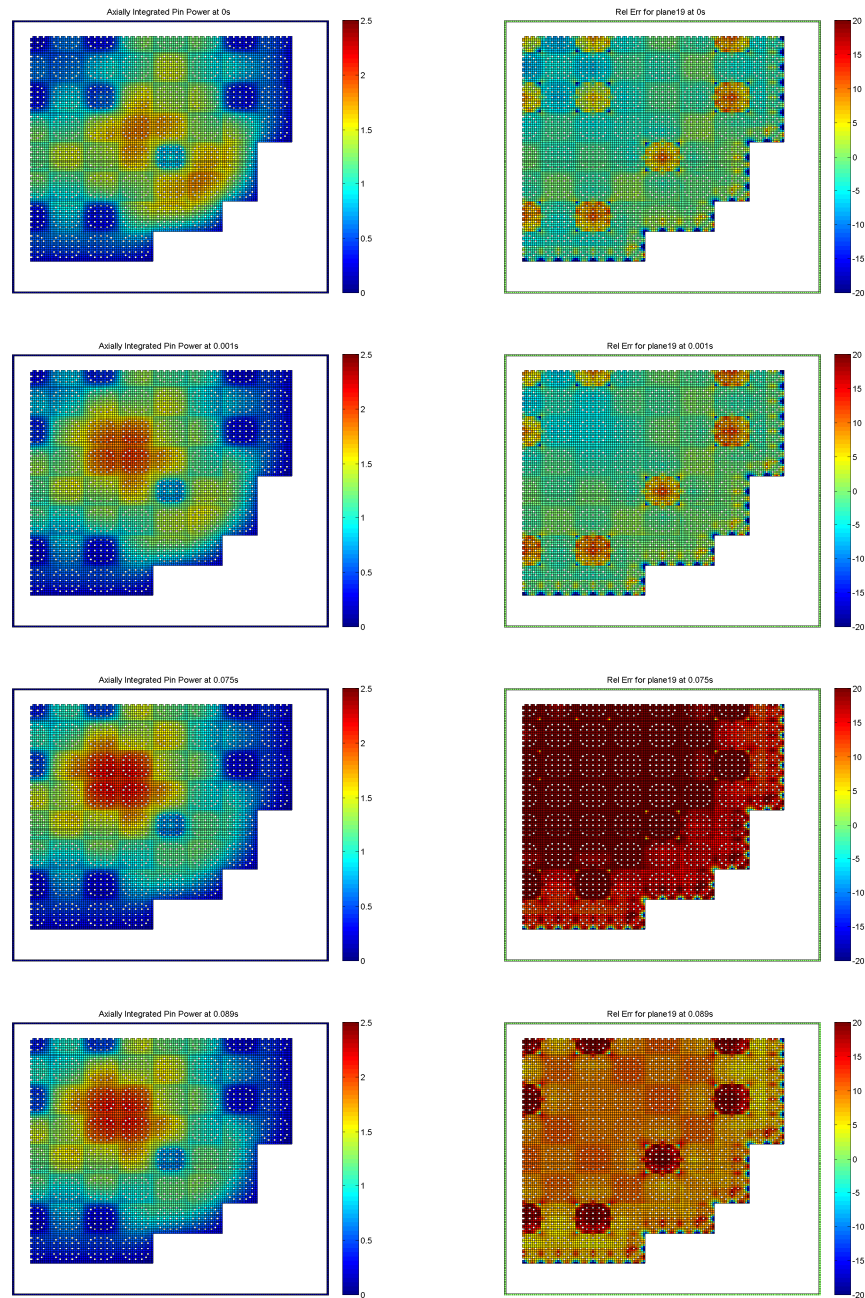
Fig. 5.16. Evolution of the local fuel rod power distribution during RIA case A scenario at BOC

The conclusion which can be drawn from the comparison of the core average power evolution and the relative difference between PARCS and DeCART is also applicable for the local fuel rod power prediction.

The difference observed in terms of core average power evolution can be attributed principally to different control rod worth in the PARCS and DeCART steady-

state solution. The steady state difference tends to mask the potential difference introduced by other neutronic approximations during the transient. The multi-steps methodology, for its approximation, produces results very close to the higher fidelity methodology of DeCART.

5.5. Summary

The DeCART code is capable of performing a full core RIA analysis with thermal hydraulic feedbacks. The procedure to include fuel and moderator temperature feedbacks as well as density was implemented in DeCART and represents a significant and original contribution to LWR reactor analysis methods since this is the first time a transport based transient calculation has been performed with local temperature feedback.

One of the other objectives of this project was to perform a code-to-code comparison between a high fidelity method such as used in DeCART and the multi-step methodology such as used in PARCS for a realistic full core RIA scenario. In order to insure the consistency of the code-to-code comparisons, some approximations were made to the modeling of the rod ejection accident scenario.

A high-fidelity analysis of representative fuel assemblies with explicit representation of individual fuel pins and surrounding coolant channels was performed using transient solution scheme in DeCART. As a basis of comparison, the same analysis was performed with the U.S. NRC PARCS neutronic code which is representative of the multi-steps methodology currently used by the industry for performing control rod ejection analysis. The RIA analysis performed here was applied to a 1/8th reactor core model corresponding to the equilibrium core composition of a PWR with fuel designs and cycle lengths representative of current utility operating strategies.

A 1/8th core model based on a 4-loop Westinghouse design was developed with fuel designs and cycle lengths representative of current utility operating strategies. Three different RIA analyses are performed. First at BOC, the ejection of two different control assemblies was performed in which one assembly was ejected near the center of the core and the other one near its periphery. At EOC, only the analysis of the ejection of the control assembly near the core periphery was performed. All three RIA analyses were performed using the DeCART code with a simplified thermal hydraulic feedback model. The DeCART results were compared to the current generation of LWR core analysis methods represented by the PARCS code which used a thermal hydraulic feedback model consistent with that used by DeCART. In order to achieve consistency between DeCART and PARCS, the DeCART code was used as a lattice code to generate the assembly homogenized macroscopic cross sections and kinetic parameters required by PARCS.

There is good overall agreement in terms of core average power and pin-wise power between DeCART and PARCS for the RIA at BOC. The differences observed in terms of time and magnitude of the peak power, are due to differences in the steady state calculations.

6. Conclusions

6.1. <u>Dissertation Summary</u>

The current state of the art in reactor physics methods to assess safety, fuel failure, and operability margins for Design Basis Accidents (DBAs) for Light Water Reactors (LWRs) rely upon the coupling of nodal neutronics and one-dimensional thermal hydraulic system codes. The neutronic calculations rely on a multistep approach which was identified as inadequate for several applications (Cho 2006) such as the design of MOX cores and other innovative reactor designs. Because of the considerable advances in computing power over the last several years, there has been interest in high-fidelity solutions of the Boltzmann Transport equation. A practical approach to solving the 3D transport equation is the 2D-1D methodology in which the method of characteristics (MOC) is applied to the heterogeneous 2D planar problem and a lower order solution is applied to the axial problem which is more uniform. Recently, there has been interest in taking advantage of advanced numerical methods to perform high-fidelity simulations of design basis accidents, such as control rod ejection accidents also known as reactivity initiated accidents (RIA).

The primary ojective of the dissertation is to improve the accuracy and range of applicability of the DeCART code and to investigate its ability to perform a full core transient analysis of a realistic RIA.. During preliminary RIA analysis, the accuracy of the DeCART "2D-1D" formulation was found to be insufficient due to an axial solver based on the diffusion theory and poor convergence properties in case of strong axial leakage or fine axial spatial meshing.

The specific research objectives of this work were accomplished. This included:

- The addition of more accurate 2D-1D coupling and transverse leakage splitting options to avoid the occurrence of negative source terms in the 2D MOC equations and the subsequent failure of the DeCART calculation and the improvement of the convergence of the 2D-1D method.
- The implementation of a higher order transport axial solver based on NEM-Sn derivation of the Boltzmann equation.
- The proper handling of thermal hydraulic feedbacks by DeCART during transient calculations.
- A consistent comparison of the DeCART transient methodology with the current multistep approach (PARCS) for a realistic full core RIA.

An efficient direct whole core transport calculation method involving the NEM-Sn formulation for the axial solution and the MOC for the 2-D radial solution was established. In this solution method, the solutions for the Sn equations were obtained by employing the Nodal Expansion Method. It was shown that the NEM-Sn solution turned out to be effective in reducing the eigenvalue error resulting from the diffusion approximation. The eigenvalue error could be reduced from 110 pcm to 12 pcm for the C5G7 Rodded Configuration B problem and the pin power error from 2.7 to 2.3%.

Therefore, it can be concluded that the newly implemented NEM-Sn axial solver improves the solution accuracy compared to the original NEM based solver. A 1/8th core model based on a 4-loop Westinghouse design was developed with fuel designs and cycle lengths representative of current utility operating strategies. A RIA analysis was performed and the DeCART results were compared to the current generation of LWR core analysis methods represented by the PARCS code. Consistent thermal hydraulic feedbacks model and cross section data were used for DeCART and PARCS. The DeCART code was used as a lattice code to generate the assembly homogenized macroscopic cross sections and kinetic parameters required by PARCS. There is good overall agreement in terms of global and local pin-wise power information DeCART and PARCS for the RIA considered. However, it is important to keep in mind that the considered RIA represents a relatively "easy" problem. A more drastic event, where the control assembly is closer to the core periphery is expected to show the limitation of the current methodology.

6.2. Recommended Future Work

One of the main approximations of the 2D-1D methodology is the azimuthal integration of the transverse leakage at the planar surface. Introducing an azimuthally dependent transverse leakage would produce real 3D transport accuracy, while still not performing a full 3D MOC calculation. It would represent an intermediate step towards a 3D MOC.

In term of full core transient analysis with DeCART, the work summarized in the dissertation has been limited to the analysis of RIA event because of the simplified thermal hydraulic solver available. Future work on this project should take advantage of the coupling of DeCART to STAR-CD in order to improve the fidelity of the thermal-hydraulics solution and to extend the range of potential applications: extend RIA analysis post departure from nucleate boiling (DNB), analyze LOCA, etc... Another way to extend the range of multi-physics analysis capability would be the coupling to a fuel performance code (e.g. FALCON). Such coupling would be needed in order to investigate the effect in terms of fuel and cladding response (strain energy density, stress) of the local conditions (power, temperature, pressure) during the transient analysis. Finally, the DeCART transient methodology has been validated against the current multi-step methodology, but a comparison with experimental results would be needed to show the benefits of the higher fidelity approach and the flaws of the current methodology. A very good candidate for validation would be the Short Period Excursion Reactor Transients (SPERT) (Spano 1964) experiments.

REFERENCES

Brantley, P. S. and E. W. Larsen (2000). "The simplified P3 approximation." <u>Nuclear Science and Engineering</u> **134**(Copyright 2000, IEE): 1-21.

CD-adapco (2004). STAR-CD Version 3.27 Methodology Manual. U.K.

Cho, J.-Y., K.-S. Kim, et al. (2006). <u>Error quantification of the axial nodal diffusion kernel of the DeCART code</u>. PHYSOR-2006 - American Nuclear Society's Topical Meeting on Reactor Physics, September 10, 2006 - September 14, 2006, Vancouver, BC, Canada, American Nuclear Society.

Cho, J.-Y., K. S. Kim, et al. (2007). "Axial SPN and radial MOC coupled whole core transport calculation." <u>Journal of Nuclear Science and Technology</u> **44**(Copyright 2008, The Institution of Engineering and Technology): 1156-1171.

Cho, J. Y., K. S. Kim, et al. (2005). "Transient capability for a MOC-based whole core transport code DeCART." <u>Transactions of the American Nuclear Society</u> **92**(Copyright 2006, IEE): 721-722.

Cho, N. Z. (2002). "Refinement of the 2-D/1-D Fusion Method for 3-D Whole-Core Transport Calculation." <u>Transactions of the American Nuclear Society</u> **87**: 417.

Cho, N. Z. (2006). "Fundamentals and Recent Developments of Reactor Physics Methods." <u>Nuclear Engineering and Techmology</u> **1**(37): 53.

Cho, N. Z. and G. S. Lee (2006). "2D/1D fusion method solutions of the three-dimensional transport OECD benchmark problem C5G7 MOX." <u>Progress in Nuclear Energy</u> **48**(Copyright 2006, The Institution of Engineering and Technology): 410-423.

Cho, N. Z., G. S. Lee, et al. (2002). "Fusion of Method of Characteristics and Nodal Method for 3-D Whole-Core Transport Calculation." <u>Transactions of the American Nuclear Society</u> **86**: 322.

Cho, N. Z., G. S. Lee, et al. (2003). <u>Partial current-based CMFD acceleration of the 2D/1D fusion method for 3D whole-core transport calculations</u>. 2003 Annual Meeting of the American Nuclear Society, 1-5 June 2003, USA, ANS.

Downar, T., Y. Xu, et al. (2006). <u>PARCS: Purdue advance reactor core simulator</u>. Proceedings of ANS Reactor Physics Topical Meeting PHYSOR 2006, Vancouver, BC.

Finnemann, H. and H. Bauer (1994). <u>Status and future of the NEACRP PWR core transient benchmark</u>. 1994 Winter Meeting of American Nuclear Society (papers in summary form only received), 13-17 Nov. 1994, USA.

Finnemann, H., F. Bennewitz, et al. (1977). "Interface nodal current technique for multi-dimensional reactor calculation." <u>Atomkernenergie</u> **30**.

Fu, X. D. and N. Z. Cho (2002). "Nonlinear analytic and semi-analytic nodal methods for multigroup neutron diffusion calculations." <u>Journal of Nuclear Science and Technology</u> **39**(Copyright 2003, IEE): 1015-1025.

Goldstein, R. and E. R. Cohen (1962). "Theory of resonance absorption of neutrons." Nuclear Science and Engineering **13**(Copyright 2004, IEE): 132-140.

Halsall, M. J. (1980). CACTUS, a characteristics solution to the neutron transport equations in complicated geometries. UK, UKAEA, Winfrith, Dorset, UK. **AEEW-R 1291:** 49.

Hursin, M. (2008). PWR Control Rod Ejection Analysis with the Method Of Characteristic Code DeCART. Physor Interlaken, Swtizerland.

Hursin, M. (2008). Pwr control rod ejection analysis with the numerical nuclear reactor. 2008 Water Reactor Fuel Performance Meeting, Seoul, Korea.

Joo, H. G., S. H. Beom, et al. (2005). Implementation of subgroup method in direct core transport calculation involving nonuniform temperature distribution. Mathematics and Computation, Supercomputing, Reactor Physics and Nuclear and Biological Applications, Palais des Papes, Avignon, France, American Nuclear Society, LaGrange Park, IL.

Joo, H. G., J. Y. Cho, et al. (2004). Methods and performance of a three-dimensional whole-core transport code DeCART. PHYSOR 2004: The Physics of Fuel Cycles and Advanced Nuclear Systems - Global Developments, April 25, 2004 - April 29, 2004, Chicago, IL, United states, American Nuclear Society.

Keepin, G. R., T. F. Wimmett, et al. (1957). "Delayed Neutrons from Fissionable Isotopes of Uranium, Plutonium and Thorium." Physical Review **107**.

Kochunas, B. (2008). Advanced Simulations of Heterogeneous Light Water Reactor Cores for Transuranic Recycle. Nuclear Engineering. Berkeley, University of California at Berkeley. **Master**.

Kosaka, S. and E. Saji (2000). "Transport theory calculation for a heterogeneous multi-assembly problem by characteristics method with direct neutron path linking technique." Journal of Nuclear Science and Technology **37**(Compendex): 1015-1023.

Kosaka, S. and T. Takeda (2004). "Verification of 3D heterogeneous core transport calculation utilizing nonlinear iteration technique." Journal of Nuclear Science and Technology **41**(Copyright 2004, IEE): 645-654.

Lee, C. H. and T. J. Downar (2004). "A hybrid nodal diffusion/SP3 method using one-node coarse-mesh finite difference formulation." Nuclear Science and Engineering **146**(Copyright 2005, IEE): 176-187.

Lee, D., T. J. Downar, et al. (2004). Numerical convergence analysis of the CMFD method for the three-dimensional two-group diffusion problem. PHYSOR 2004: The Physics of Fuel Cycles and Advanced Nuclear Systems - Global Developments, April 25, 2004 - April 29, 2004, Chicago, IL, United states, American Nuclear Society.

Lee, D., T. J. Downar, et al. (2004). "A nodal and finite difference hybrid method for pin-by-pin heterogeneous three-dimensional light water reactor diffusion

calculations." <u>Nuclear Science and Engineering</u> **146**(Copyright 2005, IEE): 319-339.

Lee, H. C., D. Lee, et al. (2004). <u>Convergence analysis of 2-D/1-D coupling methods for the three-dimensional neutron diffusion equation</u>. PHYSOR 2004: The Physics of Fuel Cycles and Advanced Nuclear Systems - Global Developments, April 25, 2004 - April 29, 2004, Chicago, IL, United states, American Nuclear Society.

Leonard, A. and C. T. McDaniel (1995). <u>Optimal polar angles and weights for the characteristics method</u>. 1995 Winter Meeting of American Nuclear Society (papers in summary form only received), 29 Oct.-2 Nov. 1995, USA.

Lewis, E., M. Smith, et al. (2001). Benchmark Specification for Deterministic 2-D13-D MOX Fuel Assembly Transport Calculations without Spatial Homogenization (C5G7 MOX). <u>NEA/NSC/DOC(2001)4</u>. NEA.

Notari, C. and Z. Garraffo (1987). "Spatial self-shielding for heterogeneous cells." <u>Annals of Nuclear Energy</u> **14**(Copyright 1988, IEE): 615-618.

NRC (2001). RELAP5/MOD3.3 Code Manual Volume I: Code Structure, System Models and Solution Methods.

Odar, F., C. Murray, et al. (2004). TRACE V4.0 User's manual, US. Nuclear Regulatory Commission.

Ott, K. O. and R. J. Neuhold (1985). <u>Introductory Nuclear Reactor Dynamics</u>. La Grange Park, IL, American Nuclear Society.

Pointer, D., C. H. Lee, et al. (2009). Steady State, Whole-Core VHTR Simulation with Consistent Coupling of Neutronics and Thermo-fluid Analysis. Argonne, IL 60439, Argonne National Laboratory.

Rhodes, J. e. a. (2008). CASMO-5 Energy Release Model. <u>Physor 2008</u>. Interlaken Switzerland.

Scandpower, S. (2000). HELIOS 1.7 Methods.

Smith, K. S. (1983). "Nodal Method Storage Reduction by Nonlinear Iteration." <u>Transactions of the American Nuclear Society</u> **44**: 265.

Smith, K. S. (1986). <u>Multidimensional nodal transport using the simplified PL method</u>. 1986 Annual Meeting of the American Nuclear Society (papers in summary form only received), 15-19 June 1986, USA.

Smith, K. S. (1999). <u>SIMULATE-3 Neutronic Enhancements and MOX Verification Tests</u>, Studsvik Scandpower SSP-99/439.

Stamm'Ler, R. J. J. and M. J. Abbate (1983). "Methods of Steady-State Reactor Physics in Nuclear Design."

Sutton, T. M. (1989). "NODEX: A High Order NEM-Based Multigroup Nodal Code." <u>Proc. Topical Meeting on Advances in Nuclear Engineering Computations and Radiation Shielding</u>: 38:31.

Thomas, J. (2006). Neutron Transport with the Method of Characteristics for 3-D Full Core Boiling Water Reactor Applications. Nuclear Engineering. Lafayette, IN, Purdue. **Ph. D.**

Weber, D., T. Sofu, et al. (2006). Extension of integrated neutronic and thermal-hydraulic analysis capabilities of the "numerical nuclear reactor" software system for BWR applications. PHYSOR-2006 - American Nuclear Society's Topical Meeting on Reactor Physics, September 10, 2006 - September 14, 2006, Vancouver, BC, Canada, American Nuclear Society.

Xu, Y. and T. Downar (2005). GenPMAXS Code For Generating the PARCS Cross Section Interface File PMAXS, Purdue University School Of Engineering.

Appendix A DeCART Inputs for Chapter 3

A.1. Input Information for Water Hole Case

The following represents the base DeCART input deck used for the Water Hole case study. The 2D-1D coupling options are refined through the card *split_opt* and the axial meshing is increased through the card *ax_mesh* and *stack*. The file c5g7.xsl contains the 7 energy group cross sections specified in the C5G7 benchmark.

```
CASEID WaterHole

MATERIAL

GEOM
 ncells  1
 pitch   1.26
!
 pin  1  0.2665 0.9935 1.260 / 1.260 / 7 1 7 / 1 3 1/ 5
 pin  2           1.260 / 1.260 / 7 / 5 / 5
 pin  3           1.260 / 1.260 / 8 / 5 / 5
!
 cell 1 1 1
  1
 cell 2 1 1
  2
 cell 3 1 1
  3
!
!
 assembly 1  360   1
  1

 assembly 2  360   1
  2

 assembly 3  360    1
  3
! Axial Description
!
 ax_mesh  3*18.900
 stack 1 2*1 1*2
 stack 2 1*2 2*2
 stack 3 1*2 2*3
!
 rad_conf 360
  1 1 2 1 1

 albedo 0.0 0.0 0.5
OPTION
 cmfd F F
 split_opt -2
!
XSEC
 lib_type 1
 group_spec  7 4
 file c5g7.xsl
.
```

A.2. Input Information for Control Rod Case

The following represents the base DeCART input deck used for the Contro Rod case study. The 2D-1D coupling options are refined through the card *split_opt* and the

axial meshing is increased through the card *ax_mesh* and *stack*. The file c5g7.xsl contains the 7 energy group cross sections specified in the C5G7 benchmark.

```
CASEID ControlRod

MATERIAL

GEOM
 ncells  1
 pitch   1.26
!
 pin  1  0.2665 0.9935 1.260 / 1.260 / 7 1 7 / 1 3 1/ 5
 pin  2            1.260 / 1.260 / 7 / 5 / 5
 pin  3            1.260 / 1.260 / 8 / 5 / 5
!
 cell 1 1 1
  1
 cell 2 1 1
  2
 cell 3 1 1
  3
!
!
 assembly 1  360   1
 1

 assembly 2  360   1
 2

 assembly 3  360    1
 3
! Axial Description
!
 ax_mesh  3*18.900
 stack 1 2*1 1*2
 stack 2 1*2 2*2
 stack 3 1*2 2*3
!
 rad_conf 360
  1 1 3 1 1

 albedo 0.0 0.0 0.5
OPTION
 cmfd F F
 split_opt -2
!
XSEC
 lib_type 1
 group_spec  7 4
 file c5g7.xsl
.
```

A.3. Input Information for Low density Case

A.3.1. Low Density Cross Sections

The cross sections used to model a reduced coolant density are detailed in the Table A. 1 below. They were obtained by multiplying the original coolant cross section by 0.01.

Table A. 1 Main cross sections for the Low Density case.

Group	Σ_a	$\nu\Sigma_f$	$\kappa\Sigma_f$	χ

1	6.01E-06	0.0	0.0	5.88E-01
2	1.58E-07	0.0	0.0	4.12E-01
3	3.37E-06	0.0	0.0	3.39E-04
4	1.94E-05	0.0	0.0	1.18E-07
5	5.74E-05	0.0	0.0	0.00E+00
6	1.50E-04	0.0	0.0	0.00E+00
7	3.72E-04	0.0	0.0	0.00E+00

Table A. 2 Scattering cross sections for the Low Density case

		To Group						
		1	2	3	4	5	6	7
	1	4.45E-04	1.13E-03	7.23E-06	3.75E-08	5.32E-10	0.00E+00	0.00E+00
	2	0.0	2.82E-03	1.30E-03	6.23E-06	4.80E-07	7.45E-08	1.05E-08
	3	0.0	0.0	3.45E-03	2.25E-03	1.70E-04	2.64E-05	5.03E-06
From Group	4	0.0	0.0	0.0	9.10E-04	4.16E-03	6.37E-04	1.21E-04
	5	0.0	0.0	0.0	7.14E-07	1.39E-03	5.12E-03	6.12E-04
	6	0.0	0.0	0.0	0.0	2.22E-05	7.00E-03	5.37E-03
	7	0.0	0.0	0.0	0.0	0.0	1.32E-03	2.48E-02

A.3.2. *DeCART Input*

The following represents the base DeCART input deck used for the Low Density case study. The 2D-1D coupling options are refined through the card *split_opt* and the axial meshing is increased through the card *ax_mesh* and *stack*. The file c5g7.xsl contains the 7 energy group cross sections specified in the C5G7 benchmark.

```
CASEID Void

MATERIAL

GEOM
 ncells  1
 pitch   1.26
 !
 pin  1  0.2665 0.9935 1.260 / 1.260 / 12 1 12 / 1 3 1/ 5
 pin  2            1.260 / 1.260 / 12 / 5 / 5
 pin  3            1.260 / 1.260 / 12 / 5 / 5
 !
 cell 1 1 1
  1
 cell 2 1 1
  2
 cell 3 1 1
  3
 !
 !
 assembly 1  360   1
 1
```

```
 assembly 2  360   1
 2

 assembly 3  360    1
 3
! Axial Description
!
 ax_mesh  3*18.900
 stack 1 2*1 1*2
 stack 2 1*2 2*2
 stack 3 1*2 2*3
!
 rad_conf 360
  1 1 1 1 1

 albedo 0.0 0.0 0.5
OPTION
 cmfd F F
 split_opt -2
!
XSEC
 lib_type 1
 group_spec  7 4
 file c5g7.xsl
.
```

Appendix B DeCART Input for Chapter 4

The geometry is described in the main body of the dissertation. Here is some additional information. The pin cell geometry is shown in the Fig B. 1below.

■Fuel-Clad Mix
□Moderator
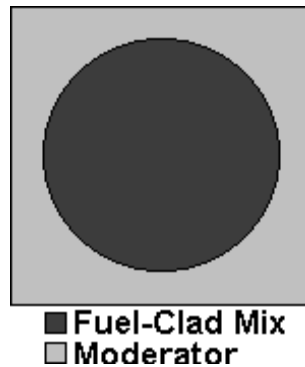
Fig B. 1 Pin cell geometry

The following represents the base DeCART input deck used for unrodded case and the rodded configuration A and B. The base DeCART model consists of four planes of three 14.28 cm planes for the fuel region and one 21.42 cm plane for the axial reflector region. In the sub-plane calculation, each plane is divided into several sub-planes for an accurate treatment of the axial neutron leakage. Within each fuel cell, 64 flat source regions consisting of eight annular regions and eight azimuthal sectors are defined. Two additional annular regions are assigned in the moderator region. The five inner annular regions have the same area.

The ray option is fixed by using 4 azimuthal and 2 polar angles for each octant of the unit sphere to define the solid angle, and 0.05 cm ray spacing. The convergence criterion is set to 1e-5 for the eigenvalue and the 2-norm of the fission source.

The axial NEM-Sn solver is called by using the card *nemsn* and the number of sub-planes is specified by the card *submesh*. The Gaussian angular quadrature is used by setting the card *pol_quad* to T. The file c5g7.xsl contains the 7 energy group cross sections specified in the C5G7 benchmark.

The next three sections describe the base input DeCART for the unrodded, rodded case A and rodded case B respectively.

B.1. Unrodded Case DeCART Input

CASEID 3d_ur C5G7 BENCHMARK Problem

MATERIAL

GEOM
ncells 17
pitch 1.26
ax_mesh 3*14.28 21.42
albedo 0.5 0.0 0.5
!

```
! 1:UO2-3.3, 2:MOX4.3, 3:MOX7.0, 4:MOX8.7,  5:FissCham, 6:GT, 7:MOD
pin 1 0.540 0.62 0.63 / 1 7 7 / 3 1 / 24 8 8
pin 2 0.540 0.62 0.63 / 2 7 7 / 3 1 / 24 8 8
pin 3 0.540 0.62 0.63 / 3 7 7 / 3 1 / 24 8 8
pin 4 0.540 0.62 0.63 / 4 7 7 / 3 1 / 24 8 8
pin 5 0.540 0.62 0.63 / 5 7 7 / 3 1 / 24 8 8
pin 6 0.540 0.62 0.63 / 6 7 7 / 3 1 / 24 8 8
pin 7 0.540 0.62 0.63 / 7 7 7 / 3 1 / 24 8 8
pin 8 0.540 0.62 0.63 / 8 7 7 / 3 1 / 24 8 8
!
cell 1 1 1
 1
cell 2 1 1
 2
cell 3 1 1
 3
cell 4 1 1
 4
cell 5 1 1
 5
cell 6 1 1
 6
cell 7 1 1
 7
cell 8 1 1
 8
!
 stack 1  3*1  4*7
 stack 2  3*2  4*7
 stack 3  3*3  4*7
 stack 4  3*4  4*7
 stack 5  3*5  4*5
 stack 6  3*6  4*8
 stack 7  3*7  4*7
 stack 8  2*6 1*8  4*8
 stack 9  1*6 2*8  4*8
!
 assembly 1  360  1
 1 1 1 1 1 1 1 1 1 1 1 1 1 1 1 1 1
 1 1 1 1 1 1 1 1 1 1 1 1 1 1 1 1 1
 1 1 1 1 1 6 1 1 6 1 1 6 1 1 1 1 1
 1 1 1 6 1 1 1 1 1 1 1 1 1 6 1 1 1
 1 1 1 1 1 1 1 1 1 1 1 1 1 1 1 1 1
 1 1 6 1 1 6 1 1 6 1 1 6 1 1 6 1 1
 1 1 1 1 1 1 1 1 1 1 1 1 1 1 1 1 1
 1 1 1 1 1 1 1 1 1 1 1 1 1 1 1 1 1
 1 1 6 1 1 6 1 1 5 1 1 6 1 1 6 1 1
 1 1 1 1 1 1 1 1 1 1 1 1 1 1 1 1 1
 1 1 1 1 1 1 1 1 1 1 1 1 1 1 1 1 1
 1 1 6 1 1 6 1 1 6 1 1 6 1 1 6 1 1
 1 1 1 1 1 1 1 1 1 1 1 1 1 1 1 1 1
 1 1 1 6 1 1 1 1 1 1 1 1 1 6 1 1 1
 1 1 1 1 1 6 1 1 6 1 1 6 1 1 1 1 1
 1 1 1 1 1 1 1 1 1 1 1 1 1 1 1 1 1
 1 1 1 1 1 1 1 1 1 1 1 1 1 1 1 1 1
!
 assembly 2  360  1
 2 2 2 2 2 2 2 2 2 2 2 2 2 2 2 2 2
 2 3 3 3 3 3 3 3 3 3 3 3 3 3 3 3 2
 2 3 3 3 3 6 3 3 6 3 3 6 3 3 3 3 2
 2 3 3 6 3 4 4 4 4 4 4 4 3 6 3 3 2
 2 3 3 3 4 4 4 4 4 4 4 4 4 3 3 3 2
 2 3 6 4 4 6 4 4 6 4 4 6 4 4 6 3 2
 2 3 3 4 4 4 4 4 4 4 4 4 4 4 3 3 2
 2 3 3 4 4 4 4 4 4 4 4 4 4 4 3 3 2
 2 3 6 4 4 6 4 4 5 4 4 6 4 4 6 3 2
 2 3 3 4 4 4 4 4 4 4 4 4 4 4 3 3 2
 2 3 3 4 4 4 4 4 4 4 4 4 4 4 3 3 2
 2 3 6 4 4 6 4 4 6 4 4 6 4 4 6 3 2
 2 3 3 3 4 4 4 4 4 4 4 4 4 3 3 3 2
```

```
2 3 3 6 3 4 4 4 4 4 4 4 3 6 3 3 2
2 3 3 3 3 6 3 3 6 3 3 6 3 3 3 3 2
2 3 3 3 3 3 3 3 3 3 3 3 3 3 3 3 2
2 2 2 2 2 2 2 2 2 2 2 2 2 2 2 2 2
```
!

assembly 3 360 1
```
7 7 7 7 7 7 7 7 7 7 7 7 7 7 7 7 7
7 7 7 7 7 7 7 7 7 7 7 7 7 7 7 7 7
7 7 7 7 7 7 7 7 7 7 7 7 7 7 7 7 7
7 7 7 7 7 7 7 7 7 7 7 7 7 7 7 7 7
7 7 7 7 7 7 7 7 7 7 7 7 7 7 7 7 7
7 7 7 7 7 7 7 7 7 7 7 7 7 7 7 7 7
7 7 7 7 7 7 7 7 7 7 7 7 7 7 7 7 7
7 7 7 7 7 7 7 7 7 7 7 7 7 7 7 7 7
7 7 7 7 7 7 7 7 7 7 7 7 7 7 7 7 7
7 7 7 7 7 7 7 7 7 7 7 7 7 7 7 7 7
7 7 7 7 7 7 7 7 7 7 7 7 7 7 7 7 7
7 7 7 7 7 7 7 7 7 7 7 7 7 7 7 7 7
7 7 7 7 7 7 7 7 7 7 7 7 7 7 7 7 7
7 7 7 7 7 7 7 7 7 7 7 7 7 7 7 7 7
7 7 7 7 7 7 7 7 7 7 7 7 7 7 7 7 7
7 7 7 7 7 7 7 7 7 7 7 7 7 7 7 7 7
7 7 7 7 7 7 7 7 7 7 7 7 7 7 7 7 7
```
!

assembly 4 360 1
```
1 1 1 1 1 1 1 1 1 1 1 1 1 1 1 1 1
1 1 1 1 1 1 1 1 1 1 1 1 1 1 1 1 1
1 1 1 1 1 8 1 1 8 1 1 8 1 1 1 1 1
1 1 1 8 1 1 1 1 1 1 1 1 1 8 1 1 1
1 1 1 1 1 1 1 1 1 1 1 1 1 1 1 1 1
1 1 8 1 1 8 1 1 8 1 1 8 1 1 8 1 1
1 1 1 1 1 1 1 1 1 1 1 1 1 1 1 1 1
1 1 1 1 1 1 1 1 1 1 1 1 1 1 1 1 1
1 1 8 1 1 8 1 1 5 1 1 8 1 1 8 1 1
1 1 1 1 1 1 1 1 1 1 1 1 1 1 1 1 1
1 1 1 1 1 1 1 1 1 1 1 1 1 1 1 1 1
1 1 8 1 1 8 1 1 8 1 1 8 1 1 8 1 1
1 1 1 1 1 1 1 1 1 1 1 1 1 1 1 1 1
1 1 1 8 1 1 1 1 1 1 1 1 1 8 1 1 1
1 1 1 1 1 8 1 1 8 1 1 8 1 1 1 1 1
1 1 1 1 1 1 1 1 1 1 1 1 1 1 1 1 1
1 1 1 1 1 1 1 1 1 1 1 1 1 1 1 1 1
```
!

assembly 5 360 1
```
1 1 1 1 1 1 1 1 1 1 1 1 1 1 1 1 1
1 1 1 1 1 1 1 1 1 1 1 1 1 1 1 1 1
1 1 1 1 1 9 1 1 9 1 1 9 1 1 1 1 1
1 1 1 9 1 1 1 1 1 1 1 1 1 9 1 1 1
1 1 1 1 1 1 1 1 1 1 1 1 1 1 1 1 1
1 1 9 1 1 9 1 1 9 1 1 9 1 1 9 1 1
1 1 1 1 1 1 1 1 1 1 1 1 1 1 1 1 1
1 1 1 1 1 1 1 1 1 1 1 1 1 1 1 1 1
1 1 9 1 1 9 1 1 5 1 1 9 1 1 9 1 1
1 1 1 1 1 1 1 1 1 1 1 1 1 1 1 1 1
1 1 1 1 1 1 1 1 1 1 1 1 1 1 1 1 1
1 1 9 1 1 9 1 1 9 1 1 9 1 1 9 1 1
1 1 1 1 1 1 1 1 1 1 1 1 1 1 1 1 1
1 1 1 9 1 1 1 1 1 1 1 1 1 9 1 1 1
1 1 1 1 1 9 1 1 9 1 1 9 1 1 1 1 1
1 1 1 1 1 1 1 1 1 1 1 1 1 1 1 1 1
1 1 1 1 1 1 1 1 1 1 1 1 1 1 1 1 1
```
!

assembly 6 360 1
```
2 2 2 2 2 2 2 2 2 2 2 2 2 2 2 2 2
2 3 3 3 3 3 3 3 3 3 3 3 3 3 3 3 2
2 3 3 3 3 8 3 3 8 3 3 8 3 3 3 3 2
2 3 3 8 3 4 4 4 4 4 4 4 3 8 3 3 2
2 3 3 3 4 4 4 4 4 4 4 4 4 3 3 3 2
2 3 8 4 4 8 4 4 8 4 4 8 4 4 8 3 2
2 3 3 4 4 4 4 4 4 4 4 4 4 4 3 3 2
```

```
  2 3 3 4 4 4 4 4 4 4 4 4 4 4 3 3 2
  2 3 8 4 4 8 4 4 5 4 4 8 4 4 8 3 2
  2 3 3 4 4 4 4 4 4 4 4 4 4 4 3 3 2
  2 3 3 4 4 4 4 4 4 4 4 4 4 4 3 3 2
  2 3 8 4 4 8 4 4 8 4 4 8 4 4 8 3 2
  2 3 3 3 4 4 4 4 4 4 4 4 4 3 3 3 2
  2 3 3 8 3 4 4 4 4 4 4 4 3 8 3 3 2
  2 3 3 3 3 8 3 3 8 3 3 8 3 3 3 3 2
  2 3 3 3 3 3 3 3 3 3 3 3 3 3 3 3 2
  2 2 2 2 2 2 2 2 2 2 2 2 2 2 2 2 2
!
 rad_conf 90 edge
  1 2 3
  2 1 3
  3 3 3
!
XSEC
  lib_type 1
  group_spec  7 4
  file ../../lib/c5g7.xsl
!
OPTION
  conv_crit 4*1e-5
  cmfd F F
  submesh 10
  pol_quad T
.
```

B.2. Rodded Case A DeCART Input

CASEID 3d_rA C5G7 BENCHMARK Problem

MATERIAL

```
GEOM
 ncells  17
 pitch 1.26
 ax_mesh  3*14.28 21.42
 albedo 0.5  0.0  0.5
!
! 1:UO2-3.3, 2:MOX4.3, 3:MOX7.0, 4:MOX8.7,  5:FissCham, 6:GT, 7:MOD
 pin 1 0.540 0.62 0.63 / 1 7 7 / 3 1 / 24 8 8
 pin 2 0.540 0.62 0.63 / 2 7 7 / 3 1 / 24 8 8
 pin 3 0.540 0.62 0.63 / 3 7 7 / 3 1 / 24 8 8
 pin 4 0.540 0.62 0.63 / 4 7 7 / 3 1 / 24 8 8
 pin 5 0.540 0.62 0.63 / 5 7 7 / 3 1 / 24 8 8
 pin 6 0.540 0.62 0.63 / 6 7 7 / 3 1 / 24 8 8
 pin 7 0.540 0.62 0.63 / 7 7 7 / 3 1 / 24 8 8
 pin 8 0.540 0.62 0.63 / 8 7 7 / 3 1 / 24 8 8
!
 cell 1 1 1
  1
 cell 2 1 1
  2
 cell 3 1 1
  3
 cell 4 1 1
  4
 cell 5 1 1
  5
 cell 6 1 1
  6
 cell 7 1 1
  7
 cell 8 1 1
  8
!
 stack 1  3*1  4*7
 stack 2  3*2  4*7
 stack 3  3*3  4*7
```

stack 4 3*4 4*7
stack 5 3*5 4*5
stack 6 3*6 4*8
stack 7 3*7 4*7
stack 8 2*6 1*8 4*8
stack 9 1*6 2*8 4*8
!
assembly 1 360 1
1 1 1 1 1 1 1 1 1 1 1 1 1 1 1 1 1
1 1 1 1 1 1 1 1 1 1 1 1 1 1 1 1 1
1 1 1 1 1 6 1 1 6 1 1 6 1 1 1 1 1
1 1 1 6 1 1 1 1 1 1 1 1 1 6 1 1 1
1 1 1 1 1 1 1 1 1 1 1 1 1 1 1 1 1
1 1 6 1 1 6 1 1 6 1 1 6 1 1 6 1 1
1 1 1 1 1 1 1 1 1 1 1 1 1 1 1 1 1
1 1 1 1 1 1 1 1 1 1 1 1 1 1 1 1 1
1 1 6 1 1 6 1 1 5 1 1 6 1 1 6 1 1
1 1 1 1 1 1 1 1 1 1 1 1 1 1 1 1 1
1 1 1 1 1 1 1 1 1 1 1 1 1 1 1 1 1
1 1 6 1 1 6 1 1 6 1 1 6 1 1 6 1 1
1 1 1 1 1 1 1 1 1 1 1 1 1 1 1 1 1
1 1 1 6 1 1 1 1 1 1 1 1 1 6 1 1 1
1 1 1 1 1 6 1 1 6 1 1 6 1 1 1 1 1
1 1 1 1 1 1 1 1 1 1 1 1 1 1 1 1 1
1 1 1 1 1 1 1 1 1 1 1 1 1 1 1 1 1
!
assembly 2 360 1
2 2 2 2 2 2 2 2 2 2 2 2 2 2 2 2 2
2 3 3 3 3 3 3 3 3 3 3 3 3 3 3 3 2
2 3 3 3 3 6 3 3 6 3 3 6 3 3 3 3 2
2 3 3 6 3 4 4 4 4 4 4 4 3 6 3 3 2
2 3 3 3 4 4 4 4 4 4 4 4 4 3 3 3 2
2 3 6 4 4 6 4 4 6 4 4 6 4 4 6 3 2
2 3 3 4 4 4 4 4 4 4 4 4 4 4 3 3 2
2 3 3 4 4 4 4 4 4 4 4 4 4 4 3 3 2
2 3 6 4 4 6 4 4 5 4 4 6 4 4 6 3 2
2 3 3 4 4 4 4 4 4 4 4 4 4 4 3 3 2
2 3 3 4 4 4 4 4 4 4 4 4 4 4 3 3 2
2 3 6 4 4 6 4 4 6 4 4 6 4 4 6 3 2
2 3 3 3 4 4 4 4 4 4 4 4 4 3 3 3 2
2 3 3 6 3 4 4 4 4 4 4 4 3 6 3 3 2
2 3 3 3 3 6 3 3 6 3 3 6 3 3 3 3 2
2 3 3 3 3 3 3 3 3 3 3 3 3 3 3 3 2
2 2 2 2 2 2 2 2 2 2 2 2 2 2 2 2 2
!
assembly 3 360 1
7 7 7 7 7 7 7 7 7 7 7 7 7 7 7 7 7
7 7 7 7 7 7 7 7 7 7 7 7 7 7 7 7 7
7 7 7 7 7 7 7 7 7 7 7 7 7 7 7 7 7
7 7 7 7 7 7 7 7 7 7 7 7 7 7 7 7 7
7 7 7 7 7 7 7 7 7 7 7 7 7 7 7 7 7
7 7 7 7 7 7 7 7 7 7 7 7 7 7 7 7 7
7 7 7 7 7 7 7 7 7 7 7 7 7 7 7 7 7
7 7 7 7 7 7 7 7 7 7 7 7 7 7 7 7 7
7 7 7 7 7 7 7 7 7 7 7 7 7 7 7 7 7
7 7 7 7 7 7 7 7 7 7 7 7 7 7 7 7 7
7 7 7 7 7 7 7 7 7 7 7 7 7 7 7 7 7
7 7 7 7 7 7 7 7 7 7 7 7 7 7 7 7 7
7 7 7 7 7 7 7 7 7 7 7 7 7 7 7 7 7
7 7 7 7 7 7 7 7 7 7 7 7 7 7 7 7 7
7 7 7 7 7 7 7 7 7 7 7 7 7 7 7 7 7
7 7 7 7 7 7 7 7 7 7 7 7 7 7 7 7 7
7 7 7 7 7 7 7 7 7 7 7 7 7 7 7 7 7
!
assembly 4 360 1
1 1 1 1 1 1 1 1 1 1 1 1 1 1 1 1 1
1 1 1 1 1 1 1 1 1 1 1 1 1 1 1 1 1
1 1 1 1 1 8 1 1 8 1 1 8 1 1 1 1 1
1 1 1 8 1 1 1 1 1 1 1 1 1 8 1 1 1
1 1 1 1 1 1 1 1 1 1 1 1 1 1 1 1 1

```
 1 1 8 1 1 8 1 1 8 1 1 8 1 1 8 1 1 8 1 1
 1 1 1 1 1 1 1 1 1 1 1 1 1 1 1 1 1 1 1 1
 1 1 1 1 1 1 1 1 1 1 1 1 1 1 1 1 1 1 1 1
 1 1 8 1 1 8 1 1 5 1 1 8 1 1 8 1 1 8 1 1
 1 1 1 1 1 1 1 1 1 1 1 1 1 1 1 1 1 1 1 1
 1 1 1 1 1 1 1 1 1 1 1 1 1 1 1 1 1 1 1 1
 1 1 8 1 1 8 1 1 8 1 1 8 1 1 8 1 1 8 1 1
 1 1 1 1 1 1 1 1 1 1 1 1 1 1 1 1 1 1 1 1
 1 1 1 8 1 1 1 1 1 1 1 1 1 1 8 1 1 1 1 1
 1 1 1 1 1 8 1 1 8 1 1 8 1 1 1 1 1 1 1 1
 1 1 1 1 1 1 1 1 1 1 1 1 1 1 1 1 1 1 1 1
 1 1 1 1 1 1 1 1 1 1 1 1 1 1 1 1 1 1 1 1
!
 assembly 5  360  1
 1 1 1 1 1 1 1 1 1 1 1 1 1 1 1 1 1 1 1 1
 1 1 1 1 1 1 1 1 1 1 1 1 1 1 1 1 1 1 1 1
 1 1 1 1 1 9 1 1 9 1 1 9 1 1 1 1 1 1 1 1
 1 1 1 9 1 1 1 1 1 1 1 1 1 9 1 1 1 1 1 1
 1 1 1 1 1 1 1 1 1 1 1 1 1 1 1 1 1 1 1 1
 1 1 9 1 1 9 1 1 9 1 1 9 1 1 9 1 1 9 1 1
 1 1 1 1 1 1 1 1 1 1 1 1 1 1 1 1 1 1 1 1
 1 1 1 1 1 1 1 1 1 1 1 1 1 1 1 1 1 1 1 1
 1 1 9 1 1 9 1 1 5 1 1 9 1 1 9 1 1 9 1 1
 1 1 1 1 1 1 1 1 1 1 1 1 1 1 1 1 1 1 1 1
 1 1 1 1 1 1 1 1 1 1 1 1 1 1 1 1 1 1 1 1
 1 1 9 1 1 9 1 1 9 1 1 9 1 1 9 1 1 9 1 1
 1 1 1 1 1 1 1 1 1 1 1 1 1 1 1 1 1 1 1 1
 1 1 1 9 1 1 1 1 1 1 1 1 1 9 1 1 1 1 1 1
 1 1 1 1 1 9 1 1 9 1 1 9 1 1 1 1 1 1 1 1
 1 1 1 1 1 1 1 1 1 1 1 1 1 1 1 1 1 1 1 1
 1 1 1 1 1 1 1 1 1 1 1 1 1 1 1 1 1 1 1 1
!
 assembly 6  360  1
 2 2 2 2 2 2 2 2 2 2 2 2 2 2 2 2 2 2 2 2
 2 3 3 3 3 3 3 3 3 3 3 3 3 3 3 3 3 3 3 2
 2 3 3 3 3 8 3 3 8 3 3 8 3 3 3 3 3 3 3 2
 2 3 3 8 3 4 4 4 4 4 4 4 3 8 3 3 3 2
 2 3 3 3 4 4 4 4 4 4 4 4 4 3 3 3 2
 2 3 8 4 4 8 4 4 8 4 4 8 4 4 8 3 2
 2 3 3 4 4 4 4 4 4 4 4 4 4 4 3 3 2
 2 3 3 4 4 4 4 4 4 4 4 4 4 4 3 3 2
 2 3 8 4 4 8 4 4 5 4 4 8 4 4 8 3 2
 2 3 3 4 4 4 4 4 4 4 4 4 4 4 3 3 2
 2 3 3 4 4 4 4 4 4 4 4 4 4 4 3 3 2
 2 3 8 4 4 8 4 4 8 4 4 8 4 4 8 3 2
 2 3 3 3 4 4 4 4 4 4 4 4 4 3 3 3 2
 2 3 3 8 3 4 4 4 4 4 4 4 3 8 3 3 3 2
 2 3 3 3 3 8 3 3 8 3 3 8 3 3 3 3 3 3 3 2
 2 3 3 3 3 3 3 3 3 3 3 3 3 3 3 3 3 3 3 2
 2 2 2 2 2 2 2 2 2 2 2 2 2 2 2 2 2 2 2 2
!
 rad_conf 90 edge
 4 2 3
 2 1 3
 3 3 3
!
XSEC
 lib_type 1
 group_spec  7 4
 file ../../lib/c5g7.xsl
!
OPTION
 conv_crit 4*1e-5
 cmfd F F
 submesh 10
 pol_quad T
.
```

B.3. Rodded Case B DeCART Input

CASEID 3d_rB C5G7 BENCHMARK Problem

MATERIAL

GEOM
ncells 17
pitch 1.26
*ax_mesh 3*14.28 21.42*
albedo 0.5 0.0 0.5
!
! 1:UO2-3.3, 2:MOX4.3, 3:MOX7.0, 4:MOX8.7, 5:FissCham, 6:GT, 7:MOD
pin 1 0.540 0.62 0.63 / 1 7 7 / 3 1 / 24 8 8
pin 2 0.540 0.62 0.63 / 2 7 7 / 3 1 / 24 8 8
pin 3 0.540 0.62 0.63 / 3 7 7 / 3 1 / 24 8 8
pin 4 0.540 0.62 0.63 / 4 7 7 / 3 1 / 24 8 8
pin 5 0.540 0.62 0.63 / 5 7 7 / 3 1 / 24 8 8
pin 6 0.540 0.62 0.63 / 6 7 7 / 3 1 / 24 8 8
pin 7 0.540 0.62 0.63 / 7 7 7 / 3 1 / 24 8 8
pin 8 0.540 0.62 0.63 / 8 7 7 / 3 1 / 24 8 8
!
cell 1 1 1
* 1*
cell 2 1 1
* 2*
cell 3 1 1
* 3*
cell 4 1 1
* 4*
cell 5 1 1
* 5*
cell 6 1 1
* 6*
cell 7 1 1
* 7*
cell 8 1 1
* 8*
!
*stack 1 3*1 4*7*
*stack 2 3*2 4*7*
*stack 3 3*3 4*7*
*stack 4 3*4 4*7*
*stack 5 3*5 4*5*
*stack 6 3*6 4*8*
*stack 7 3*7 4*7*
*stack 8 2*6 1*8 4*8*
*stack 9 1*6 2*8 4*8*
!
assembly 1 360 1
* 1 1 1 1 1 1 1 1 1 1 1 1 1 1 1 1 1*
* 1 1 1 1 1 1 1 1 1 1 1 1 1 1 1 1 1*
* 1 1 1 1 1 6 1 1 6 1 1 6 1 1 1 1 1*
* 1 1 1 6 1 1 1 1 1 1 1 1 1 6 1 1 1*
* 1 1 1 1 1 1 1 1 1 1 1 1 1 1 1 1 1*
* 1 1 6 1 1 6 1 1 6 1 1 6 1 1 6 1 1*
* 1 1 1 1 1 1 1 1 1 1 1 1 1 1 1 1 1*
* 1 1 1 1 1 1 1 1 1 1 1 1 1 1 1 1 1*
* 1 1 6 1 1 6 1 1 5 1 1 6 1 1 6 1 1*
* 1 1 1 1 1 1 1 1 1 1 1 1 1 1 1 1 1*
* 1 1 1 1 1 1 1 1 1 1 1 1 1 1 1 1 1*
* 1 1 6 1 1 6 1 1 6 1 1 6 1 1 6 1 1*
* 1 1 1 1 1 1 1 1 1 1 1 1 1 1 1 1 1*
* 1 1 1 6 1 1 1 1 1 1 1 1 1 6 1 1 1*
* 1 1 1 1 1 6 1 1 6 1 1 6 1 1 1 1 1*
* 1 1 1 1 1 1 1 1 1 1 1 1 1 1 1 1 1*
* 1 1 1 1 1 1 1 1 1 1 1 1 1 1 1 1 1*
!
assembly 2 360 1
* 2 2 2 2 2 2 2 2 2 2 2 2 2 2 2 2 2*

2 3 3 3 3 3 3 3 3 3 3 3 3 3 3 2
2 3 3 3 3 6 3 3 6 3 3 6 3 3 3 2
2 3 3 6 3 4 4 4 4 4 4 3 6 3 3 2
2 3 3 3 4 4 4 4 4 4 4 4 3 3 3 2
2 3 6 4 4 6 4 4 6 4 4 6 4 4 6 3 2
2 3 3 4 4 4 4 4 4 4 4 4 4 3 3 2
2 3 3 4 4 4 4 4 4 4 4 4 4 3 3 2
2 3 6 4 4 6 4 4 5 4 4 6 4 4 6 3 2
2 3 3 4 4 4 4 4 4 4 4 4 4 3 3 2
2 3 3 4 4 4 4 4 4 4 4 4 4 3 3 2
2 3 6 4 4 6 4 4 6 4 4 6 4 4 6 3 2
2 3 3 3 4 4 4 4 4 4 4 4 3 3 3 2
2 3 3 6 3 4 4 4 4 4 4 3 6 3 3 2
2 3 3 3 3 6 3 3 6 3 3 6 3 3 3 2
2 3 3 3 3 3 3 3 3 3 3 3 3 3 3 2
2 2 2 2 2 2 2 2 2 2 2 2 2 2 2 2
!
assembly 3   360   1
7 7 7 7 7 7 7 7 7 7 7 7 7 7 7 7
7 7 7 7 7 7 7 7 7 7 7 7 7 7 7 7
7 7 7 7 7 7 7 7 7 7 7 7 7 7 7 7
7 7 7 7 7 7 7 7 7 7 7 7 7 7 7 7
7 7 7 7 7 7 7 7 7 7 7 7 7 7 7 7
7 7 7 7 7 7 7 7 7 7 7 7 7 7 7 7
7 7 7 7 7 7 7 7 7 7 7 7 7 7 7 7
7 7 7 7 7 7 7 7 7 7 7 7 7 7 7 7
7 7 7 7 7 7 7 7 7 7 7 7 7 7 7 7
7 7 7 7 7 7 7 7 7 7 7 7 7 7 7 7
7 7 7 7 7 7 7 7 7 7 7 7 7 7 7 7
7 7 7 7 7 7 7 7 7 7 7 7 7 7 7 7
7 7 7 7 7 7 7 7 7 7 7 7 7 7 7 7
7 7 7 7 7 7 7 7 7 7 7 7 7 7 7 7
7 7 7 7 7 7 7 7 7 7 7 7 7 7 7 7
7 7 7 7 7 7 7 7 7 7 7 7 7 7 7 7
!
assembly 4   360   1
1 1 1 1 1 1 1 1 1 1 1 1 1 1 1 1
1 1 1 1 1 1 1 1 1 1 1 1 1 1 1 1
1 1 1 1 1 8 1 1 8 1 1 8 1 1 1 1
1 1 1 8 1 1 1 1 1 1 1 1 8 1 1 1
1 1 1 1 1 1 1 1 1 1 1 1 1 1 1 1
1 1 8 1 1 8 1 1 8 1 1 8 1 1 8 1 1
1 1 1 1 1 1 1 1 1 1 1 1 1 1 1 1
1 1 1 1 1 1 1 1 1 1 1 1 1 1 1 1
1 1 8 1 1 8 1 1 5 1 1 8 1 1 8 1 1
1 1 1 1 1 1 1 1 1 1 1 1 1 1 1 1
1 1 1 1 1 1 1 1 1 1 1 1 1 1 1 1
1 1 8 1 1 8 1 1 8 1 1 8 1 1 8 1 1
1 1 1 1 1 1 1 1 1 1 1 1 1 1 1 1
1 1 1 8 1 1 1 1 1 1 1 1 8 1 1 1
1 1 1 1 1 8 1 1 8 1 1 8 1 1 1 1
1 1 1 1 1 1 1 1 1 1 1 1 1 1 1 1
1 1 1 1 1 1 1 1 1 1 1 1 1 1 1 1
!
assembly 5   360   1
1 1 1 1 1 1 1 1 1 1 1 1 1 1 1 1
1 1 1 1 1 1 1 1 1 1 1 1 1 1 1 1
1 1 1 1 1 9 1 1 9 1 1 9 1 1 1 1
1 1 1 9 1 1 1 1 1 1 1 1 9 1 1 1
1 1 1 1 1 1 1 1 1 1 1 1 1 1 1 1
1 1 9 1 1 9 1 1 9 1 1 9 1 1 9 1 1
1 1 1 1 1 1 1 1 1 1 1 1 1 1 1 1
1 1 1 1 1 1 1 1 1 1 1 1 1 1 1 1
1 1 9 1 1 9 1 1 5 1 1 9 1 1 9 1 1
1 1 1 1 1 1 1 1 1 1 1 1 1 1 1 1
1 1 1 1 1 1 1 1 1 1 1 1 1 1 1 1
1 1 9 1 1 9 1 1 9 1 1 9 1 1 9 1 1
1 1 1 1 1 1 1 1 1 1 1 1 1 1 1 1
1 1 1 9 1 1 1 1 1 1 1 1 9 1 1 1

```
  1 1 1 1 1 9 1 1 9 1 1 9 1 1 9 1 1 1 1 1
  1 1 1 1 1 1 1 1 1 1 1 1 1 1 1 1 1 1 1 1
  1 1 1 1 1 1 1 1 1 1 1 1 1 1 1 1 1 1 1 1
!
 assembly 6  360  1
  2 2 2 2 2 2 2 2 2 2 2 2 2 2 2 2 2 2 2 2
  2 3 3 3 3 3 3 3 3 3 3 3 3 3 3 3 3 3 3 2
  2 3 3 3 3 8 3 3 8 3 3 8 3 3 3 3 2
  2 3 3 8 3 4 4 4 4 4 4 4 3 8 3 3 2
  2 3 3 3 4 4 4 4 4 4 4 4 3 3 3 2
  2 3 8 4 4 8 4 4 8 4 4 8 4 4 8 3 2
  2 3 3 4 4 4 4 4 4 4 4 4 4 3 3 2
  2 3 3 4 4 4 4 4 4 4 4 4 4 3 3 2
  2 3 8 4 4 8 4 4 5 4 4 8 4 4 8 3 2
  2 3 3 4 4 4 4 4 4 4 4 4 4 3 3 2
  2 3 3 4 4 4 4 4 4 4 4 4 4 3 3 2
  2 3 8 4 4 8 4 4 8 4 4 8 4 4 8 3 2
  2 3 3 3 4 4 4 4 4 4 4 4 3 3 3 2
  2 3 3 8 3 4 4 4 4 4 4 4 3 8 3 3 2
  2 3 3 3 3 8 3 3 8 3 3 8 3 3 3 3 2
  2 3 3 3 3 3 3 3 3 3 3 3 3 3 3 3 3 3 3 2
  2 2 2 2 2 2 2 2 2 2 2 2 2 2 2 2 2 2 2 2
!
 rad_conf 90 edge
  5 6 3
  6 1 3
  3 3 3
!
XSEC
  lib_type 1
  group_spec  7 4
  file ../../lib/c5g7.xsl
!
OPTION
  pol_quad T
  conv_crit 4*1e-5
  cmfd F F
  submesh 10
.
```

Appendix C Codes Input for Chapter 5

C.1. Additional Information

The number of density for each material is provided inTable C. 1. They correspond to the fresh material before exposure and are used as starting point for the core equilibrium calculation.

Table C. 1. Material Compositions

Material	Density [g/cm^3]	Enrichment	Isotope	Number of Density [#/b-cm]
UO$_2$ Fuel	10.412	4.0% U-235	U-235	9.41E-04
			U-238	2.23E-02
			O-16	4.65E-02
IFBA	1.690	---	B-10	3.59E-03
			B-11	1.45E-02
			Nat. Zr.	9.02E-03
Gap	0.001	---	O-16	3.76E-05
			N-14	2.15E-05
Clad/Guide Tube	6.504	---	Nat. Cr	4.28E-05
			Nat. Fe	5.13E-05
			Nat. Zr	4.20E-02
			Nat. Sn	6.42E-04
Core Baffle	7.820	---	Nat. Cr	1.63E-02
			Mn-55	1.71E-03
			Nat. Fe	5.99E-02
			Nat. Ni	7.22E-03

The loading pattern, which has not been optimized, is shown in Fig C. 1 for the PWR core model and is used to generate the equilibrium core composition. The number indicates the current cycle of residence for that assembly, (e.g. 1 is for the first cycle of residence and indicates a fresh assembly). The letter indicates the path along which the assembly is shuffled throughout its residency in the core. The shuffling path of the P1 assembly is less intuitive. Its location has eight symmetric positions elsewhere in the full core. It is then moved onto two locations on the quarter-symmetry boundary, which in the full core also accounts for eight assembly locations; therefore P$_a$2 and P$_b$2 will have the same composition at BOC which is equivalent to the P1 composition at EOC. Note that the axial reflectors consist only of water; the density of which is computed by the T/H module and contains soluble boron.

Q3 P$_a$2 B$_a$3 P$_b$2 P$_b$3 B$_a$1 P$_a$3 B1

A3 L2 D3 D2 F3 L1 J1

```
Q2    H2    H3    O2    O3    F1
      A2    F2    L3    H1    D1
            Q1    J2    O1
                  A1    P1
```

Fig C. 1. PWR Loading Pattern

The spatial discretization of the various pin cells is shown in Fig C. 2. The mesh in the axial reflectors is the same as the mesh in the regions below, so the part of the axial reflector above the fuel will have the fuel pin mesh, and similarly for the parts above the guide tubes and baffle and radial reflector. Axially, there are 22 planes, each of equal thickness (18.288 cm). The subgroup calculation is performed once at the beginning and then again at 10 GWd/t. The rays spacing is 0.05 cm with 4 azimuthal and 2 polar angles per 90° octant. The SANM solver is used for computing the partial currents in the axial direction. For the heat conduction calculation, one mesh region is used for the clad and six equidistance rings are used in the fuel pellet. The tolerance is 10_{-5} for the eigenvalue, fission source and CMFD balance residuals.

a) Fuel Pin Mesh	b) Guide Tube Mesh
c) Baffle and Radial Reflector Mesh	d) Axial Reflector Mesh
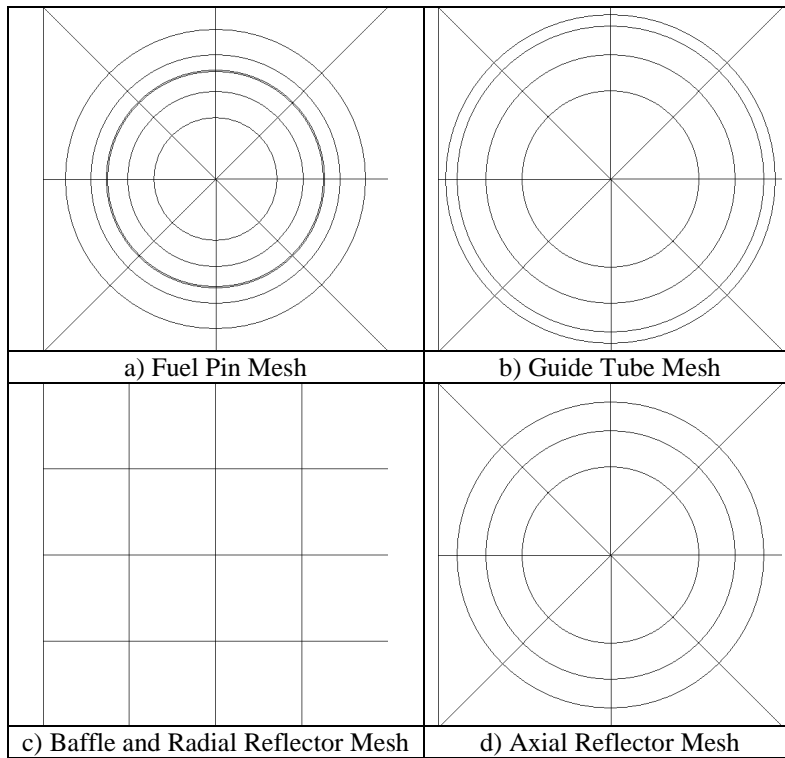
Fig C. 2. Pin cell mesh in PWR DeCART model

C.2. DeCART Input

C.2.1. *Lattice Calculations*

Below is the DeCART input used to generate cross sections for the PARCS run. The BRANCH cases are missing and are described in Chapter 5.

```
CASEID  batch1

STATE
!       power_fa (MW), t_in(C), p_exit(MPa), mdot_fa (kg/s)
  th_cond    18.4715   286.85      15.5    82.12102

MATERIAL
  file    ../../shared_input/mixtures.inp

GEOM
  ncells   17
  pitch    1.26
  ax_mesh  22*18.288
  albedo   0.0 0.0 0.0 0.0 0.5 0.5

  file    ../../shared_input/pins3D.inp
  file    ../../shared_input/assemblies.inp
!
! Assembly Types
! 1 - UO2 4.2%
! 2 - UO2 4.2% Control Assembly
! 3 - West Edge Baffle/Reflector
! 4 - NE Corner Baffle/Reflector
! 5 - NE Edge Baffle/Reflector
! 6 - North Edge Baffle/Reflector
!
    rad_conf 45
     1
!
XSEC
  lib_type  0 0
  file      ../../shared_input/hel047g_v19a_ascii.xsl
  depl_lib  ../../shared_input/DeCART_v2.dpl
TH
  pin_dim   0.3951 0.4583 0.0573  0.6032
  steam_tbl ../../shared_input/tpfh2o_ascii.txt
  matprop   F
!
OPTION
  feedback  T 0.5
  cmfd      T T
  reso_opt  4 F F
  nem       F
  ray       0.05 4 2
  boron     1000
  threads   1
!
SHUFFLE
!
  id_map
    BATCH0
!
  cfile_map
    0
!
  rot_map
    0
!
  id_wrt
    BATCH1
!
```

```
EDIT
  eqx  F
  rst  T
  isum F
  bin  T
/
DEPL
  bu_opt 2 1
  burnup 0.1 0.5
EDIT
  isum F
  rst  F
  eqx  F
/
DEPL
  bu_opt 2 2
  burnup 1.0 2.0 3.0 4.0 5.0
EDIT
  isum F
  rst  F
  eqx  F
/
DEPL
  bu_opt 2 5
  burnup 7.5 10.0 12.5 15.0
EDIT
  isum F
  rst  F
  eqx  F
.
```

C.2.2. Transient Calculations

Below is the input used to run the RIA scenario presented in Chapter 5 . The equilibrium core composition is recorded in the file PWR_UO2_octCore.core.

```
CASEID  PWR_UO2_octCore_octCore
  init PWR_UO2_octCore_000_00000.rst
STATE
!       power_fa (MW), t_in(C), p_exit(MPa), mdot_fa (kg/s)
  core_power  1e-6
  th_cond    18.4715   286.85      15.5    82.12102

MATERIAL
  file    ../shared_input/mixtures.inp

GEOM
  ncells   17
  pitch    1.26
  ax_mesh  22*18.288
  albedo   0.5 0.0 0.0 0.5 0.0 0.0

  file    ../shared_input/pins3Dtmp.inp
  file    ../shared_input/assemblies.inp
!
! Assembly Types
! 1 - UO2 4.2%
! 2 - UO2 4.2% Control Assembly
! 3 - West Edge Baffle/Reflector
! 4 - NE Corner Baffle/Reflector
! 5 - NE Edge Baffle/Reflector
! 6 - North Edge Baffle/Reflector
!

  rad_conf  45 CENT
   2  1  2  1  2  1  2  1  3
    1  1  1  1  2  1  1  3
```

```
           2  1  1  2  1  3
             1  1  2  1  1  3
               2  1  2  5  4
                 1  1  3
                   5  4

XSEC
  lib_type   0 0
  file        ../shared_input/hel047g_v19a_ascii.xsl
  depl_lib   ../shared_input/DeCART_v2.dpl
  chi_lib T
TH
  pin_dim    0.3951 0.4583 0.0573  0.6032
  steam_tbl  ../shared_input/tpfh2o_ascii.txt
  matprop    F
!
SHUFFLE
  cfile 1 PWR_UO2_octCore.core
  file       ../shared_input/eighth/lp_mh_n.inp
!
OPTION
  feedback   T 0.5
  cmfd       T T
  ray        0.05 4  2
  boron 1000.
  threads    1
EDIT
  rst  T
ROD
  rod_typ PWR 220
  rod_mat 9 9 9 9 9 9 9 9 9
  no_rod 11
! bank 1 CR-A see MOX benchmark
! bank 2 CR-B
! bank 3 CR-C
! bank 4 CR-D
! bank 5 CR-SA
! bank 6 CR-SB
! bank 7 CR-SC
! bank 8 CR-SD
! bank 9 Cr to eject
  bank 1 3
  bank 2 22
  bank 3 7 18
  bank 4 1
  bank 5 33
  bank 6 14
  bank 7 27
  bank 8 5
  bank 9 31
  bank_pos 1 220.0 2 220.0 3 220.0 4 220.0 5 0.0 6 0.0 7 0.0 8 0.0 9 220.0 ! RI
  move_bank 9 0.0005 220 0.0006 0
!
/
STATE
  tran  T
TRAN
  time_step  0.1 0.0001 0.001 10
  theta  1.0
  expo_opt  F
  cond_rt 1e-2 1e0 1e-2
OPTION
  feedback T
.
```

C.3. PARCS Input

Below is the PARCS input used to run the RIA scenario presented in Chapter 5. The 3-D exposure map is specified in the file EXPu.dep. The fuel, reflector and corner cross sections in UO2_900_inf.PMAX, refl_xu.PMAX and corner.PMAX respectively.

```
!*****************************************************************************
CASEID PWR_3D4_TR_uo2_900_inf Transient Validation
!*****************************************************************************
CNTL
    core_power 1e-6
!     bank   A    B    C    D   SA   SB   SC   SD  to eject step withdrawn
    bank_pos  0.0 0.0 0.0 0.0 22.0 22.0 22.0 22.0 0.0  ! RI MOX benchmark config
!     bank_pos  0.0 0.0 0.0 0.0 22.0 22.0 22.0 22.0  ! RO
    depletion T
    TREE_XS  T  2      T F F F F F T F F F T T T F
!                a,x,e,j,p,d,v,t,y,c,g,b,l,h
!     search ppm
    ppm 0.2
!     ppm 949.96
    transient  F
    th_fdbk   T
    pin_power  T
!----------------------------------------------------------------------------
!            input iteration   planar            adj
!            edit    table    power     pin      reac
    print_opt      T       F        T        T        T
!            fdbk     flux    planar
!            rho    precurs    flux    xe/sm     T/H
    print_opt      F       F        F        F        F
!            1d      pk    rad pwr   rad flux    assy
!            const    data    shape     shape    const
    print_opt      F       T        F        F        F
!*****************************************************************************
PARAM
!*****************************************************************************
GEOM
    geo_dim  17 17 22 1 1    !nasyx,nasyy,nz
    Rad_Conf
    0 0 0 0 1 1 1 1 1 1 1 1 0 0 0 0
    0 0 1 1 1 2 2 2 2 2 2 2 1 1 1 0 0
    0 1 1 2 2 2 2 2 2 2 2 2 2 1 1 0
    0 1 2 2 2 2 2 2 2 2 2 2 2 2 1 0
    1 1 2 2 2 2 2 2 2 2 2 2 2 2 1 1
    1 2 2 2 2 2 2 2 2 2 2 2 2 2 2 1
    1 2 2 2 2 2 2 2 2 2 2 2 2 2 2 1
    1 2 2 2 2 2 2 2 2 2 2 2 2 2 2 1
    1 2 2 2 2 2 2 2 2 2 2 2 2 2 2 1
    1 2 2 2 2 2 2 2 2 2 2 2 2 2 2 1
    1 2 2 2 2 2 2 2 2 2 2 2 2 2 2 1
    1 2 2 2 2 2 2 2 2 2 2 2 2 2 2 1
    1 1 2 2 2 2 2 2 2 2 2 2 2 2 1 1
    0 1 2 2 2 2 2 2 2 2 2 2 2 2 1 0
    0 1 1 2 2 2 2 2 2 2 2 2 2 1 1 0
    0 0 1 1 1 2 2 2 2 2 2 2 1 1 1 0 0
    0 0 0 0 1 1 1 1 1 1 1 1 0 0 0 0

    grid_x    17*21.42
    neutmesh_x 17*2
    grid_y    17*21.42
    neutmesh_y 17*2
    grid_z    22*18.288

    Boun_Cond  2 2  2  2  2  2 !ibcw,ibce,ibcn,ibcs,ibcb,ibct

    planar_reg 1
```

```
         2 2 2 2 2 2 2 2
       2 2 3 1 1 1 1 1 1 1 3 2 2
      2 3 1 1 1 1 1 1 1 1 1 1 3 2
      2 1 1 1 1 1 1 1 1 1 1 1 1 1 2
     2 3 1 1 1 1 1 1 1 1 1 1 1 1 3 2
     2 1 1 1 1 1 1 1 1 1 1 1 1 1 1 1 2
     2 1 1 1 1 1 1 1 1 1 1 1 1 1 1 1 2
     2 1 1 1 1 1 1 1 1 1 1 1 1 1 1 1 2
     2 1 1 1 1 1 1 1 1 1 1 1 1 1 1 1 2
     2 1 1 1 1 1 1 1 1 1 1 1 1 1 1 1 2
     2 1 1 1 1 1 1 1 1 1 1 1 1 1 1 1 2
     2 1 1 1 1 1 1 1 1 1 1 1 1 1 1 1 2
     2 3 1 1 1 1 1 1 1 1 1 1 1 1 3 2
      2 1 1 1 1 1 1 1 1 1 1 1 1 1 2
      2 3 1 1 1 1 1 1 1 1 1 1 3 2
       2 2 3 1 1 1 1 1 1 1 3 2 2
         2 2 2 2 2 2 2 2
```

planar_reg 2
```
         2 2 2 2 2 2 2 2
       2 2 2 2 2 2 2 2 2 2 2 2
      2 2 2 2 2 2 2 2 2 2 2 2 2 2
      2 2 2 2 2 2 2 2 2 2 2 2 2 2
     2 2 2 2 2 2 2 2 2 2 2 2 2 2 2 2
     2 2 2 2 2 2 2 2 2 2 2 2 2 2 2 2
     2 2 2 2 2 2 2 2 2 2 2 2 2 2 2 2
     2 2 2 2 2 2 2 2 2 2 2 2 2 2 2 2
     2 2 2 2 2 2 2 2 2 2 2 2 2 2 2 2
     2 2 2 2 2 2 2 2 2 2 2 2 2 2 2 2
     2 2 2 2 2 2 2 2 2 2 2 2 2 2 2 2
     2 2 2 2 2 2 2 2 2 2 2 2 2 2 2 2
     2 2 2 2 2 2 2 2 2 2 2 2 2 2 2 2
      2 2 2 2 2 2 2 2 2 2 2 2 2 2
      2 2 2 2 2 2 2 2 2 2 2 2 2 2
       2 2 2 2 2 2 2 2 2 2 2 2
         2 2 2 2 2 2 2 2
```
cr_axinfo 0.0 18.288   !fully inserted position and step size
bank_conf
```
         0 0 0 0 0 0 0 0
       0 0 0 0 0 0 0 0 0 0 0 0
      0 0 0 5 0 2 0 3 0 2 0 5 0 0 0
      0 0 0 0 7 0 6 0 6 0 7 0 0 0 0
     0 0 5 0 9 0 0 0 8 0 0 0 9 0 5 0 0
     0 0 0 7 0 0 0 0 0 0 0 0 0 7 0 0 0
     0 0 2 0 0 0 3 0 1 0 3 0 0 0 2 0 0
     0 0 0 6 0 0 0 0 0 0 0 0 0 6 0 0 0
     0 0 3 0 8 0 1 0 4 0 1 0 8 0 3 0 0
     0 0 0 6 0 0 0 0 0 0 0 0 0 6 0 0 0
     0 0 2 0 0 0 3 0 1 0 3 0 0 0 2 0 0
     0 0 0 7 0 0 0 0 0 0 0 0 0 7 0 0 0
     0 0 5 0 9 0 0 0 8 0 0 0 9 0 5 0 0
      0 0 0 0 7 0 6 0 6 0 7 0 0 0 0
      0 0 0 5 0 2 0 3 0 2 0 5 0 0 0
       0 0 0 0 0 0 0 0 0 0 0 0
         0 0 0 0 0 0 0 0
```

Pincal_loc
```
         0 0 0 0 0 0 0 0
       0 0 0 0 0 0 0 0 0 0 0 0
      0 0 0 0 0 0 0 0 0 0 0 0 0 0
      0 0 0 0 0 0 0 0 0 0 0 0 0 0
     0 0 0 0 0 0 0 0 0 0 0 0 0 0 0 0
     0 0 0 0 0 0 0 0 0 0 0 0 0 0 0 0
     0 0 0 0 0 0 0 0 0 0 0 0 0 0 0 0
     0 0 0 0 0 0 0 0 0 0 0 0 0 0 0 0
     0 0 0 0 0 0 0 0 1 1 1 1 1 1 1 0
     0 0 0 0 0 0 0 0 0 1 1 1 1 1 1 0
     0 0 0 0 0 0 0 0 0 0 1 1 1 1 1 0
     0 0 0 0 0 0 0 0 0 0 0 1 1 1 1 0
     0 0 0 0 0 0 0 0 0 0 0 0 1 1 0 0
```

```
        0 0 0 0 0 0 0 0 0 0 0 1 1 0
        0 0 0 0 0 0 0 0 0 0 0 0 0 0
         0 0 0 0 0 0 0 0 0 0 0 0 0
             0 0 0 0 0 0 0 0

    PR_Assign  1*2 20*1 1*2


!*******************************************************************************
TH
    unif_th      0.75238 286.85 286.85
    n_pingt      264 25              !npin,ngt
    fa_powpit    18.4715  21.42        !assembly power(Mw) and pitch(cm)
    pin_dim      3.951 4.583 0.573  6.032 !pin radii, rs,rw,tw, and rgt in mm
    flow_cond    286.85 82.12102           !tin,cmfrfa(Kg/sec)
    hgap         10000.                !hgap(w/M^2-C)
    n_ring       10                 !number of meshes in pellet
    thmesh_x     17*2                 !Number of T/H Nodes per FA in X-dir
    thmesh_y     17*2                 !Number of T/H Nodes per FA in y-dir
!*******************************************************************************
TRAN
    time_step    1.0 0.0001 0.001 10 !tend,delt0,tswitch,texpand
    move_bank    9  0.0 0.0 0.0005 0.0 0.0006 22.0
    conv_tr      0.001           !eps_r2
    expo_opt     F F
    pin_freq 10
!*******************************************************************************
DEPL
 INP_HST './xsec/EXPu.dep' 1 1
 PMAXS_F  1  './xsec/UO2_900_inf.PMAX'  1
 PMAXS_F  2  './xsec/refl_xu.PMAX'   2
 PMAXS_F  3  './xsec/corner.PMAX'   3
!*******************************************************************************
.
```

C.4. GenPMAXS Input

Below is the GenPMAXS input used to generate the PARCS cross sections. It uses the .xsec file generated by DeCART to produce a .pmax file.

```
%JOB_TIT
 ' UO2_900_inf.PMAX'  T   !TMI Assembly
%JOB_OPT
  T  F  F  F  F  F  F  F  F  F  F  F  F  1
 !ad,xe,de,j1,ch,Xd,iv,dt,yl,cd,gf,be,lb,dc,ups
%DAT_SRC
   4   1   1   1.0
%FIL_CNT
  1  'batch1.xsec' 1 1
%JOB_END
```